# Fast Monte Carlo Simulation of $^{90}Y$ Bremsstrahlung using a Kernel-based Photon Source

A thesis submitted in fulfilment

of the requirement for the degree of

**Doctor of Philosophy**

in

**Medical Physics**

at

**The University of Waikato**

by

**SUHAILI BINTI ZAKARIAH**

THE UNIVERSITY OF WAIKATO
Te Whare Wānanga o Waikato

**2011**

# ABSTRACT


In targeted radionuclide therapy using $^{90}Y$, bremsstrahlung photons can be used for imaging and subsequently for absorbed dose estimation. Monte Carlo simulation is a reliable method to study bremsstrahlung imaging but it takes a long computation time as not all $^{90}Y$ disintegrations result in emission of a bremsstrahlung photon. Furthermore the electron transport simulation is particularly time consuming. This research proposes that bremsstrahlung photons produced from the decay of a $^{90}Y$ point source are replaced with a kernel-based photon source for faster Monte Carlo simulation.

This study is divided into three main parts. First, a $^{90}Y$ point source in a spherical water phantom is fully simulated using Monte Carlo simulation. The characteristics of the bremsstrahlung photons produced from the $^{90}Y$ decay are investigated. The full Monte Carlo simulation of $^{90}Y$ point source provides the relationships between the emission position, energy and emission angle of the bremsstrahlung photon. These are recorded as probability distribution functions (PDFs).

Then, a kernel-based photon source which comprises of an array of photon-emitting concentric spherical shells is developed. The energy spectrum and angular distributions of the emitted photons are defined for each shell using the PDFs obtained previously from the full $^{90}Y$ Monte Carlo simulation. The kernel-based photon source shows a very close approximation to the distribution of bremsstrahlung photons generated by the full Monte Carlo simulation of $^{90}Y$ point source if the shells are sufficiently closely spaced.

Finally, the accuracy and speed of the kernel-based photon source are evaluated. A simplified gamma camera model, which consists of a collimator and NaI(Tl) detector is simulated to obtain the point spread function (PSF) of the point source 'image'. The PSF can be represented as a Gaussian function. Estimation of $\sigma$ of the Gaussian function and thus the full-width half-maximum (FWHM) is used to compare the different kernel-based photon source models to represent a 'real' source generated by a full Monte Carlo $^{90}Y$ simulation. The results show that the FWHMs of the photon source with kernels are comparable to full Monte Carlo simulation of $^{90}Y$ point source. The FWHM determined for a photon point source with the spectrum of $^{90}Y$ bremsstrahlung underestimates the full Monte Carlo simulation of the true $^{90}Y$ point source. This demonstrates that it is important to account for the photons being emitted at a distance away from the source and all of the photons cannot be assumed to come from a single point. It is more computationally efficient to use this source model than the kernel-based photon sources as it has the shortest computation time, however it is quite inaccurate. Simplifying the kernel-based source by assuming the photon emission as isotropic reduces the accuracy of the model slightly, though the reduction in simulation time is sufficiently small that the more accurate anisotropic kernel should be preferred.

The kernel-based photon source proposed in this study can be used to accurately represent the bremsstrahlung photons produced from the beta decay of a $^{90}Y$ point source. This approach greatly improves the simulation speed by almost 30 times.

# ACKNOWLEDGEMENTS

I sincerely thank my chief supervisor, Dr. Howell Round for his advice, support, input, guidance and encouragement throughout this research. In addition, I wish to thank my second supervisor, Dr. Michael Cree for sharing his thoughts and participation in my PhD research. I would also like to thank the members of the Geant4 forum for their assistance and support during the research.

I am thankful to my PhD colleagues at the room D.2.01 for their friendship over the course of my study, especially Chibueze Z. Uche. I appreciate all the help and discussion we have throughout the years. Not to forget, I would also like to thank the technical and administration staff of the Department of Engineering, University of Waikato, for all their assistance during the course of my study.

I also thank University of Technology Malaysia and Malaysian of Higher Education, for the financial support for my doctoral study.

My deepest gratitude goes to my mother, Mrs Mariam Jamaluddin, thank you for your love, support, encouragements and prayers. You are the diamond and the wind beneath my wings. My appreciation goes to my family, especially to my sister, Suhaila and family; as well as to my uncle, Dr. Jaafar Thani and family; for their understandings during my long absence. Many thanks also to all my friends either in Malaysia or Waikato, for their concern and prayers. In particular, I take this opportunity to thank my friend Siti Aisyah Abdul Rahman, who encouragement and care, kept me sane along the way. Through my ups and downs you were always there to encourage and support me. It is such a blessing to have a

friend like you and I am thankful for that. I would also like to thank Farhana Sidek for her friendship, emotional and instrumental support.

Finally, I offer my whole heart in gratitude to Allah for everything He has granted me throughout my life. I have been blessed and have been given opportunities that I know would not have come without His intervention.

# PUBLICATIONS ARISING FROM THIS THESIS

Round, W.H., Zakariah, S. and Cree, M. J. (2010). Kernel-based fast simulation of $^{90}$Y bremsstrahlung. Paper presented at the Engineering and Physical Sciences in Medicine & the Australian Biomedical Engineering Conference, Melbourne.

Round, W.H., Zakariah, S. and Cree, M. J. (2010). Fast simulation of $^{90}$Y bremsstrahlung using a kernel-based technique. Paper presented at the New Zealand Physics and Engineering in Medicine Conference, Dunedin.

Round, W.H., Zakariah, S. and Cree, M. J. (2009). Collimator characteristics for $^{90}$Y bremsstrahlung imaging. Paper presented at the RANZCR/AIR/FRO/ACPSEM Combined Scientific Meeting, Brisbane.

Zakariah, S., Round, W.H. and Cree, M. J. (2008). Photon source kernel for bremsstrahlung imaging. Poster presented at Engineering and Physical Sciences in Medicine & the Australian Biomedical Engineering Conference, Christchurch.

## TABLE OF CONTENTS

## LIST OF FIGURES

# LIST OF TABLES

# CHAPTER 1

# INTRODUCTION

## 1.1 Research background

Nuclear medicine is a branch of medicine and medical imaging that uses radiation for therapeutic and diagnostic purposes. Pure beta-emitting radionuclides such as $^{90}Y$ are increasingly used in radionuclide therapy to treat or provide pain relief for various types of malignancies. It is now commonly used in the treatment of cancers including non-Hodgkin's lymphoma (Friedberg, 2004; Wagner et al., 2002), neuroendocrine tumour (Druce et al., 2009; Lewington, 2003) and liver cancer (Gulec et al., 2009; King et al., 2008; Salem & Thurston, 2006). It is also used to treat arthritis and big joints such as the knee. The use of $^{90}Y$ is preferable because it has the benefit of delivering a high and localised radiation dose to the target area. Additionally, it also requires minimal radiation safety measures to be taken to protect the hospital staff and family members. Due to its low hazard, patients do not require hospital stay and can be released immediately after treatment (Manjunatha & Rudraswamy, 2010; Zanzonico et al., 1999).

Dosimetry is essential in radionuclide therapy to determine the radionuclide distribution (and thus absorbed dose) in the body to ensure the localisation of the radioisotope in the organ and to confirm treatment efficiency (DeNardo et al., 2001; Erdi et al., 1996). The required data needed for dosimetry in radionuclide therapy using a gamma-emitter can be obtained by directly imaging the uptake of the radionuclide in the body. However, $^{90}Y$ is a beta emitter and the beta particles have short range and are difficult to detect directly outside the body making imaging and dosimetry rather difficult. In the absence or lack of primary photons emission, $^{90}Y$ activity distribution can be imaged by acquiring events from bremsstrahlung photons created from near the decay site of $^{90}Y$ as a means of determining the beta emission distribution. Bremsstrahlung photons are secondary photons which are produced when beta particles interact with matter. Imaging of the $^{90}Y$ bremsstrahlung photons with a planar gamma camera and SPECT has been demonstrated by a number of researchers (Ito et al., 2009; Sebastian et al., 2008; Shen et al., 1994b). Studies also show that bremsstrahlung imaging can be employed to other pure beta-emitting radionuclides such as $^{32}P$ and $^{89}Sr$ (Cipriani et al., 1997; Clarke et al., 1992).

Gamma cameras are used to image radionuclides that emit photons with a distinct photopeak energy. The gamma energy determines the choice of collimator and the energy window is centred on the photopeak. Selection of collimator and energy windows is important to obtain optimal spatial resolution and sensitivity. However, there are several limitations associated with bremsstrahlung imaging which makes it difficult to apply the conventional gamma-ray imaging technique. In the case of $^{90}Y$ bremsstrahlung imaging, bremsstrahlung photons which are produced have a broad energy spectrum ranging from zero to the maximum beta energy. A distinct photopeak in energy spectrum does not exist making the choice of collimator and energy window complicated. Bremsstrahlung photon production is also low in body tissues thus reducing the sensitivity of the system. In order to increase the photon counts, a large energy window can be used but it will decrease the resolution as it is hard to distinguish primary photons and photons that have been scattered. Additionally, the photons are produced at varying distances from the source, thus the accuracy of original position determination is limited.

Monte Carlo simulation has become as an essential tool in medical physics, and now is widely used in many applications of nuclear medicine imaging. Several factors such as the physical properties of the camera, attenuation and scatter corrections as well as reconstruction algorithms can have an effect on the quality and accuracy of the image obtained from a nuclear medicine scan. Monte Carlo simulation attempts to create a model similar to a real physical system and generates the particle interactions within that system. By using a Monte Carlo simulation, it is possible to obtain results that cannot be measured experimentally. The use of Monte Carlo simulation enables the optimisation of the design of the imaging systems and thus improves the qualitative and quantitative accuracy of the reconstructed images (Andreo, 1991; Rogers, 2006; Zaidi, 1999).

## 1.2 Purpose of the research

As mentioned earlier, there are several problems associated with bremsstrahlung imaging. Most of the bremsstrahlung imaging studies reported that although bremsstrahlung photons can be imaged, the detected photon count is low and the resolution is poor (Mansberg et al., 2007; Shen, et al., 1994b). These problems should be studied further and Monte Carlo technique offers a reliable method to study bremsstrahlung imaging in order to obtain better images. However Monte Carlo simulation is always associated with long computing times. This is because Monte Carlo calculations require a large number of particle histories to be simulated in order to decrease the statistical uncertainty.

Monte Carlo simulation in bremsstrahlung imaging studies is particularly time consuming. There are two main factors that contribute to this problem, namely (i) electron transport simulation is mainly slow, and (ii) the production of bremsstrahlung photons is quite low. The simulation of electron transport is slow due to the frequent interactions of electrons. Unlike photons, an electron undergoes many interactions before it loses all its energy and it is unrealistic to track all interactions event by event. The condensed history algorithms are used in the Monte Carlo electron transport simulation in which the cumulative effects of many minor interactions are combined into a single step (Kawrakow & Bielajew, 1998; Ma et al., 2006). The condensed history technique is used in all general purpose Monte Carlo packages but the run times are still impractical. The bremsstrahlung photon yield depends on the electron energy and the atomic number of the absorber material. The average energy of $^{90}$Y beta particle is around 0.93 MeV, and the bremsstrahlung photon production is low in materials with low atomic number, such as water and tissue. This means that the bremsstrahlung production from $^{90}$Y decays inside a human body is especially low. Therefore it is necessary to run many electron histories to obtain good statistics and this implies a very long computation time. It is beneficial to find a way to achieve an acceptable computing time by reducing the time spent on tracking electrons. One way to achieve this is by increasing the cut-off energy of the electrons simulated. However, this would mean that the electron tracks are terminated sooner and might fail to properly simulate the bremsstrahlung contribution.

As another alternative solution to reduce the $^{90}$Y simulation time, this study proposes that bremsstrahlung photons produced from beta decays of a $^{90}$Y point source are replaced with a kernel-based photon source. The kernel-based photon source is an array of concentric spherical shells of photon sources that corresponds to bremsstrahlung photon emissions. This approach reduces the problem associated with simulation time in bremsstrahlung imaging studies. The use of photons as a substitute for the beta source in $^{90}Y$ bremsstrahlung imaging has been studied previously by Heard et al.(2004b) and recently by Rault et al.(2010). However, their work did not consider the emission angle of the bremsstrahlung photons and modelled the photon emission as isotropic. As will be presented in the thesis, we will see that the bremsstrahlung photon distribution is complex. It has a continuous energy spectrum, and the bremsstrahlung photons are produced at varying distances from the point where the electrons are emitted. Also, the emissions are anisotropic. As a result, the kernel-based photon source defined in this current work accounts for the position, energy and angular distribution of the bremsstrahlung photons for more accurate representation of the $^{90}Y$ bremsstrahlung photons. The kernel-based photon source is then used as a substitute for the $^{90}Y$ beta point source. Using the kernel-based photon source is expected to substantially reduce the time taken for $^{90}Y$ Monte Carlo simulations to be computed.

## 1.3 Aim and objectives of the research

The main aim of this research is to improve the Monte Carlo simulation time for $^{90}Y$ bremsstrahlung imaging studies. The objectives of this study are:

i) To investigate the characteristics, namely the energy spectrum, spatial and angular distributions of the bremsstrahlung photons produced from $^{90}Y$ decay in water.

ii) To develop a method to reduce the $^{90}Y$ bremsstrahlung simulation time by substituting the $^{90}Y$ beta point source with a kernel-based photon source.

iii) To develop a method in order to estimate the full-width half-maximum (FWHM) of a point source using a gamma camera simulation.

iv) To evaluate the accuracy and speed of the kernel-based photon source.

## 1.4 Contribution of the research

This research proposes a method where bremsstrahlung photons produced from beta decays of a $^{90}Y$ point source are replaced with a kernel-based photon source. This will greatly reduce the simulation time spent in tracking the electrons. As a consequence, Monte Carlo studies carried out to optimise bremsstrahlung imaging technology and techniques can be done more rapidly and this area of research can then be progressed faster.

Previous studies conducted to increase the $^{90}Y$ bremsstrahlung simulation speed only accounted for isotropic bremsstrahlung photon emission (Heard et al.,2004b; Rault et al., 2010). This research demonstrates the importance of modelling the bremsstrahlung as an anisotropic source as well as taking into account its emission position. This leads to a better representation of bremsstrahlung emission of $^{90}Y$.

Bremsstrahlung imaging studies is a relatively new area in nuclear medicine. Although Monte Carlo techniques have become popular in nuclear medicine, to our knowledge there is little research so far carried out in context of Monte Carlo simulation for bremsstrahlung imaging. Hence, this research will hopefully expand the knowledge and widen the literature on this aspect. This research will assist in the future research involving bremsstrahlung imaging using Monte Carlo method.

## 1.5 Structure of the thesis

This thesis is organised into seven chapters. Chapter 1 presents the background, purpose, objectives and contributions of the research. The literature review is presented in Chapter 2. It provides a brief description on the basic of nuclear and radiation physics, as well as the background on nuclear medicine. It also reviews the previous and current research in the areas relevant to the thesis topic. Chapter 3 provides a description of the Geant4 Monte Carlo simulation toolkit which is utilised in this study. Chapter 4 describes the simulations of some beta-emitting radionuclides decay to investigate the characteristics of the generated bremsstrahlung photons. It then focuses on the simulation of $^{90}$Y decay in water. The probability distributions of the bremsstrahlung photons as a function of interaction position, energy and emission angle are obtained. Chapter 5 describes the development of a kernel-based photon source that can be used to accurately model the bremsstrahlung production from the full Monte Carlo simulation of $^{90}$Y point source. The resulting distributions of the kernel-based photon source simulation are also compared to that obtained from the full Monte Carlo simulation of $^{90}$Y point source. Chapter 6 describes the validation study of the simulation method. It also describes a study on the kernel-based photon source to evaluate its speed and accuracy. Finally, Chapter 7 presents the conclusions and the recommendations.

# CHAPTER 2

# LITERATURE REVIEWS

## 2.1 Basic nuclear and radiation physics

An atomic nucleus is comprised of protons and neutrons and collectively these particles are known as nucleons. The atomic number, $Z$, and the neutron number, $N$, of an atom are determined by the number of its protons and neutrons respectively. The mass number, $A$ of a nucleus is the number of nucleons ($A + Z$). The stability of an atomic nucleus is determined by the $N/Z$ ratio of the nucleus. Unstable nuclides decay and lose energy by emitting ionising radiation in the form of alpha particles, beta particles or/and gamma rays to achieve a stable configuration of neutrons and protons in the nucleus.

In alpha decay, the nucleus ejects an alpha particle that consists of two neutrons and two protons, which is essentially a helium nucleus. Alpha particle decay is common among very heavy elements. Beta decay is a type of radioactive decay in which a beta particle (an electron or positron) is emitted. In $\beta^+$ decay, a proton is converted into a neutron and a positively charged electron is emitted along with neutrino, $\nu$. This positively charged electron is also known as positron ($\beta^+$). A neutrino is a particle with negligible mass, has no charge and is able to pass through matter almost undisturbed. In the case of $\beta^-$ decay, a neutron is converted into a proton while emitting a $\beta^-$ particle and an antineutrino, $\bar{\nu}$. A $\beta^-$ particle is actually a negatively charged electron and an antineutrino is the antiparticle of neutrino. After alpha and beta decay, the daughter nucleus may be in an excited or metastable state. The excited or metastable daughter nucleus must decay to ground or to another less energetic state by emitting gamma radiation. A gamma radiation is a high energy photon, and has no mass or electrical charge.

The energy difference between the parent and daughter nuclide is called transition or decay energy. An alpha particle has transition energy between 3–9 MeV, whereas a $\beta^-$ particle has continuous energy ranging from zero to the ‘end-point’ maximum energy value denoted by $E_{max}$. This is because, in $\beta^-$ decay, the transition energy is shared between a $\beta^-$ particle and an antineutrino. This energy sharing is random from one decay to the next. The $\beta^-$ particle energy spectrum resulting from the $\beta^-$ decay is shown in Figure 2.1. It shows that $\beta^-$ particle usually has energy less than $E_{max}$ and the remaining energy is carried by the antineutrino. Only in rare occasion does the $\beta^-$ particle carry all the energy. The average energy of the $\beta^-$ is denoted by $E_{ave}$ and usually has the value of $E_{ave} \approx ⅓\ E_{max}$. For $\beta^+$ decay to occur, a minimum transition energy of 1.022 MeV is required. The positron from $\beta^+$ decay cannot exist for a long time in matter. After ejection from nucleus, it soon combines with an atomic electron and annihilates producing two 511 keV gamma rays (also known as annihilation photons) which are emitted in opposite directions. The excess transition energy above 1.022 MeV is shared between the positron and the neutrino. The positron energy spectrum is similar to that observed for $\beta^-$ particle (Figure 2.1). The average energy for positron is $E_{ave} \approx ⅓\ E_{max}$, where $E_{max}$ is transition energy minus 1.022 MeV.

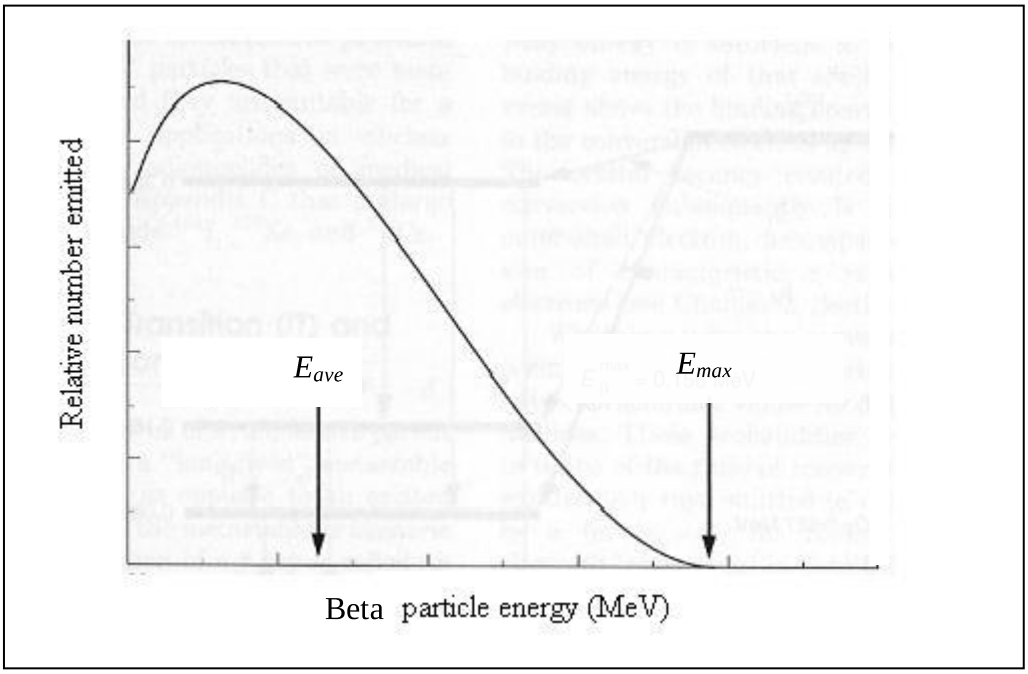


**Figure 2.1: Energy spectrum of beta particle.**

When charged particles like alpha and beta particles penetrate matter, they interact with matter through Coulomb interactions with atomic orbital electrons and atomic nuclei. Through these interactions the electrons may lose their kinetic energy (collision and radiative losses) or change their direction of travel (scattering). The collisions between the incident electron and an orbital electron or nucleus of an atom may be elastic or inelastic. In an elastic collision the electron is deflected from its original path but no energy loss occurs. In an inelastic collision the electron is deflected from its original path and loss some of its energy to an orbital electron or emitted in the form of bremsstrahlung. In collisional process, energy loss is caused by ionisation and excitation events. Ionisation and excitation is a caused by the interaction between electronic field of the charged particles and the orbital electron of a medium. In ionisation, the energy transfer is sufficient to overcome the binding energy of an orbital electron thus the electron is ejected from the atom. Excitation interactions generally result in smaller energy losses. In this process, the incident charged particle transfers all or part of its energy to the orbital electron, raising it to higher energy shells. The energy transferred in an excitation process is dissipated in molecular vibrations or atomic emission of infrared, visible or ultraviolet radiation. Collisional process decreases with the kinetic energy of the incident electron. The process of ionisation and excitation will continue until the incident particle comes to rest. The ionisation effect is very important because it is the basis for radiation detection and is responsible for radiobiological effects in tissues. The second interaction process, radiative loss, occurs when the charged particle comes close to the nucleus and is deflected by the nucleus. The particle is rapidly decelerated and losses energy by emitting continuous electromagnetic energy called bremsstrahlung.

The inelastic energy losses (collisional or radiative) by a charged particle are described by stopping power. Linear stopping power, $S$ is the rate of energy loss per unit path length by a charged particle in an absorber ($dE/dx$) and is typically given in unit MeV.cm$^2$/g. The mass stopping power refers to the linear stopping power divided by the density of the absorbing medium, $S/\rho = (1/\rho)(dE/dx)$. The total stopping power $S_{tot}$, for a charged particle with energy $E$ is the sum of collisional and radiative stopping power, $S_{tot} = S_{col} + S_{rad}$. The rate of bremsstrahlung production by light charged particles (electrons and positrons) travelling through a medium can be calculated using the Bethe-Heitler equation and is given by:

$$S_{rad} = \alpha r_e^2 Z^2 \frac{N_A}{A} B_{rad} E_i \tag{2.1}$$

where the value of $B_{rad}$ depends on the atomic number $Z$ and the initial total energy of the light charged particle $E_i$. For light charged particles, the parameter

$B_{rad}$ has the value of 16/3 in the non-relativistic energy range ($E_k << m_e c^2$), about 6 at $E_k$ = 1 MeV, 12 at $E_k$ = 10 MeV and 15 at $E_k$ = 100 MeV.

Collisional and radiative energy loss rates for electrons in the energy range of 0.01–10 MeV in different materials (that is lead and water) is shown in Figure 2.2. It clearly shows that bremsstrahlung production increases with the kinetic energy of the electron and in the atomic number of the material. In contrast, the collisional stopping power decreases with increasing electron energy and $Z$ of the medium. For electrons energies of interest in this thesis ($^{90}$Y beta particles and secondary electrons), the energies are less then few MeV. Therefore the radiative energy loss is always a small fraction. The ratio of collisional to radiative stopping power ($S_{col}/S_{rad}$) at a given electron kinetic energy is given approximately by

$$\frac{S_{col}}{S_{rad}} = \frac{\left(\frac{dE}{dx}\right)_{col}}{\left(\frac{dE}{dx}\right)_{rad}} \approx \frac{800}{Z\,E_k} \qquad (2.2)$$

and $E$ is in unit of MeV.

The interaction of alpha particles and electrons (or positrons) with matter is quite similar, but because of the large difference between their masses, they behave differently. Bremsstrahlung is substantial for light charged particles like electrons but insignificant for heavy particles like alpha particles and protons because the probability of penetrating close to the nuclei is very low due to their mass.

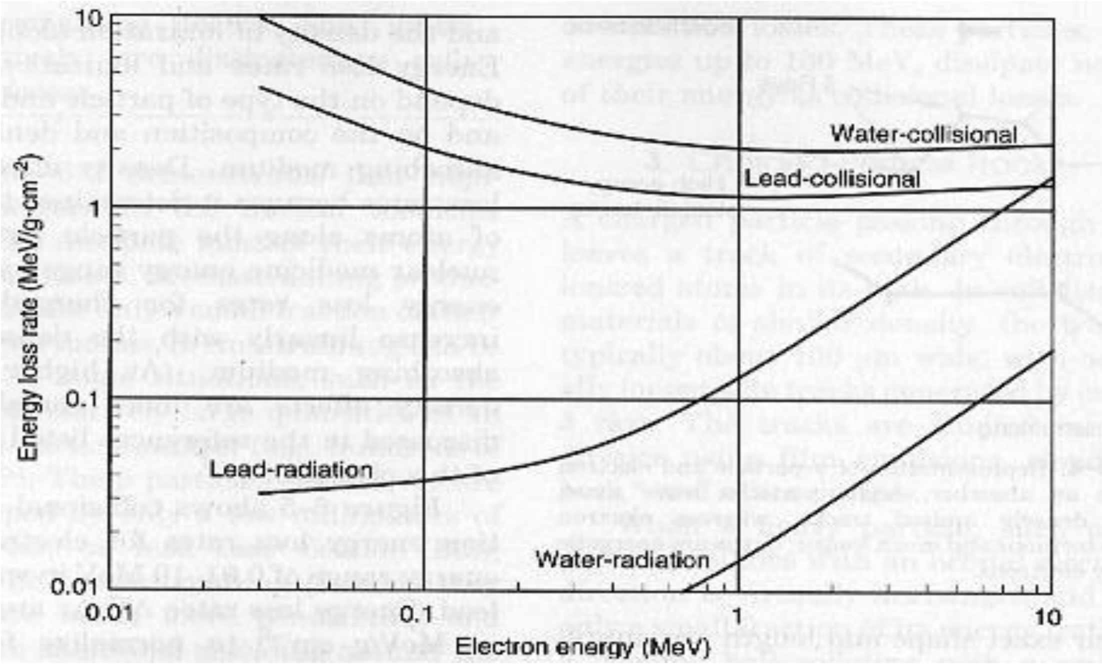


**Figure 2.2: Collisional and radiative energy loss at different electron energies for lead and water. Adapted from Cherry et al. (2003).**

The distance in a material to the point where a particle has lost all its energy is called its range. The range depends on the mass, charge and kinetic energy of the particle as well as the density of the material. An alpha particle has large mass, therefore it loses only a small fraction of its energy when colliding with an orbital electron. Its direction is almost unchanged and results in a straight path track. On the other hand, an incident electron has the same mass as an orbital electron; therefore it can lose a large fraction of its energy in a single collision and can scatter in any direction. This results in a track that is very tortuous. An electron also imparts weaker electrical forces on an orbital electron compared to an alpha particle. This means that an electron interacts less frequently, loses its energy more slowly and travels farther than an alpha particle before it is stopped.

High energy photons (gamma radiation, x-ray, annihilation radiation and bremsstrahlung) behave differently from charged particles. Unlike beta particles, the emitted gamma radiations have discrete energy values and are unique to the radionuclides. Since photons have no electrical charge, they interact infrequently with matter as they pass through making them highly penetrating. Photons interact with matter via four main mechanisms, namely the photoelectric effect, Compton scattering, pair production and Rayleigh scattering. These interactions do not cause ionisation directly, but result in the ejection of the orbital electrons or in the creation of positive-negative electron pairs which then cause ionisation.

The photoelectric effect is an atomic absorption process in which an atom absorbs all the energy of the incident photon. If sufficient energy is absorbed, an electron (known as photoelectron) is ejected from an electron shell. This will create a vacancy in the orbital electron shell and leads to the emission of characteristic x-rays or Auger electrons.

In Compton scattering, a photon collides with a loosely bound outer shell orbital electron. In this interaction, the photon transfers part of its energy to the recoil electron and is scattered at an angle determined from the amount of energy transferred in the collision.

Pair production occurs when a photon interacts with the electric field of a charged particle. In this process, the photon energy is converted into an electron-positron pair. A minimum photon energy of 1.022 MeV is required for pair production to occur. The electron pair lose their energies mostly by ionisation and excitation. The positron from the $e^+e^-$ pair will eventually interact with electron and produce a pair of 511 keV annihilation photons.

Rayleigh (or coherent) scattering occurs between a photon and an atom as a whole. Very little recoil energy is absorbed by the atom due to its large mass.

Therefore the photon is deflected with essentially no loss of energy. Rayleigh scattering is only important at energies below 50 keV.

The probability of each photon interaction to occur depends on the incident photon energy and the atomic number of the material it traverses as illustrated in the Figure 2.3 below. Photoelectric effect occurs mainly at low photon energies and its attenuation coefficient, $\tau/\rho$, is strongly dependent on the atomic number of the absorber material ($\propto Z^3$). Compton scattering predominates at intermediate energies and is the main interaction in body tissue ($Z \leq 20$). Pair production is the dominant interaction at high photon energies in materials of high atomic number.

The products of each photon interaction are secondary photons and electrons. Electrons are responsible for the deposition of energy in matter. Secondary photons and electrons can still undergo further interactions if they are energetically possible.

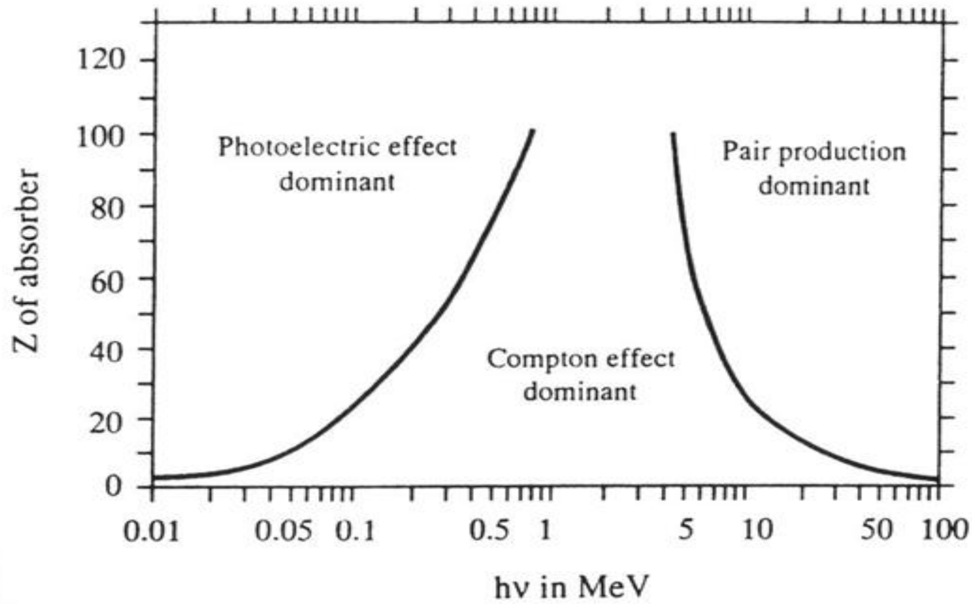


**Figure 2.3: Relative importance of the three major types of photon interaction as a function of atomic number and photon energy. Adapted from Evans (1955).**

## 2.2 Nuclear medicine

Nuclear medicine is a branch of medicine and medical imaging that involves the use of radionuclides for therapeutic and diagnostic purposes. In nuclear medicine procedure, radionuclides are labelled with a chemical compound or a pharmaceutical to form a radiopharmaceutical. The radiopharmaceutical is administered into patients by injection, ingestion or inhalation and concentrates in the organs of interest. The choice of radiopharmaceutical is based on the type of study and the target organ. This is because a particular organ only absorbs certain types of chemicals, therefore the pharmaceutical used for different organs could be different but it may be labelled with the same radionuclide. Different types of radiation may be emitted from the radiopharmaceutical depending on the radionuclide. Table 2.1 shows some of the common radionuclides used in nuclear medicine.

**Table 2.1:Basic properties of some radionuclides used in nuclear medicine**

| Radionuclide | Half-life | Photon energy (keV) | Beta particle $E_{max}$ (keV) |
|---|---|---|---|
| $^{99m}Tc$ | 6.01 hours | 140 | - |
| $^{111}In$ | 2.8 days | 171, 245 | - |
| $^{201}Tl$ | 3.04 days | 135, 167 | - |
| $^{18}F$ | 110 min | 511 (annihilation) | 634 (positron) |
| $^{131}I$ | 8.02 days | 364 | 807 |
| $^{90}Y$ | 2.67 days | - | 2280 |
| $^{32}P$ | 14.3 days | - | 1710 |
| $^{89}Sr$ | 50.5 days | - | 1463 |

Radionuclides can exist naturally but the radionuclides used in nuclear medicine are derived from fission or fusion processes where a stable atom is bombarded with sub-nuclear particles (neutrons, protons, etc.). This will cause nuclear reaction to occur and the stable nucleus becomes unstable. Radionuclides can be produced in a nuclear reactor to produce longer half-life radionuclides, or in cyclotron to produce shorter half-life radionuclides. A dedicated generator is used to take advantage of the natural decay process like $^{99}Mo/^{99m}Tc$ or $^{82}Sr/^{82}Rb$ (Saha, 1993; Volkert et al., 1991).

### 2.2.1 Radionuclide imaging

The radiopharmaceuticals are used as tracers in radionuclide imaging. The administered radiopharmaceutical accumulates inside the patient and emits radiation. The purpose of radionuclide imaging is to visualise the distribution of the radiopharmaceutical inside the body and to obtain quantitative measurement of the radiopharmaceutical taken up by the organ. Radionuclide imaging utilises the way that the organs handle chemical substance differently in the presence of disease. A tracer is distributed and processed differently when there is disease and results in the appearance of 'hot-spot' or 'cold-spot' areas. The main difference and advantage of radionuclide imaging compared to other imaging modalities is that it demonstrates the physiological process of the body or an organ rather than its anatomical structure.

An ideal radionuclide used for imaging must emit gamma radiation of sufficient energy to escape the body and can be detected by an external nuclear imaging device. The gamma radiations emitted from the radionuclides are captured and images are formed by the external detectors. The energy range of 80–500 keV (or 511 keV annihilation photons) is preferred in nuclear imaging because the gamma radiation are sufficiently penetrating to be detected from deep lying organs but still can be shielded adequately. Modern nuclear imaging primarily includes planar scintigraphy, single photon emission computed tomography (SPECT) and positron emission tomography (PET) (Hendee & Ritenour, 2002). Both planar scintigraphy and SPECT are used to detect radionuclides that emit gamma radiation like $^{99m}Tc$, $^{201}Tl$ and $^{131}I$. They are only different in a way that planar scintigraphy depicts a single two-dimensional projection view whereas SPECT represents projection of many angles obtained by rotating the gamma camera head around the patient to obtain a three-dimensional image. PET imaging also provides three-dimensional images by acquiring projection from different angles but it uses short-lived positron-emitting radionuclide such as $^{18}F$, $^{11}C$, $^{15}O$ or $^{13}N$. The positron promptly combines with nearby electron and produces a pair of 511 keV annihilation photon pairs which are detected by PET. PET design is originally based on the gamma camera but its detector is designed as opposing planes or a ring and operates by registering coincidence annihilation events on the opposite sides simultaneously which indicate its origin. Apart from oncology, PET is also commonly used for cardiac and brain imaging.

The first gamma camera was developed in 1958 by Hal O. Anger (Anger, 1958) and has become the instrumental basis for all nuclear imaging studies. Figure 2.4 illustrates the basic components of a gamma camera. Fundamentally, a gamma camera head consists of several important components: a collimator, a detector which is usually made from a NaI(Tl) scintillation crystal, an array of photomultiplier tubes (PMTs) and associated electronics. Basically each gamma radiation emerging from the body is detected by a the NaI(Tl) detector after it passes through a collimator. The gamma radiation, which are not visible to the eye, are converted into flashes of light by NaI(Tl) scintillation crystal. This light is in turn transformed into electrical signal by the photomultiplier tubes (PMTs). The electrical signal is then translated into an image.

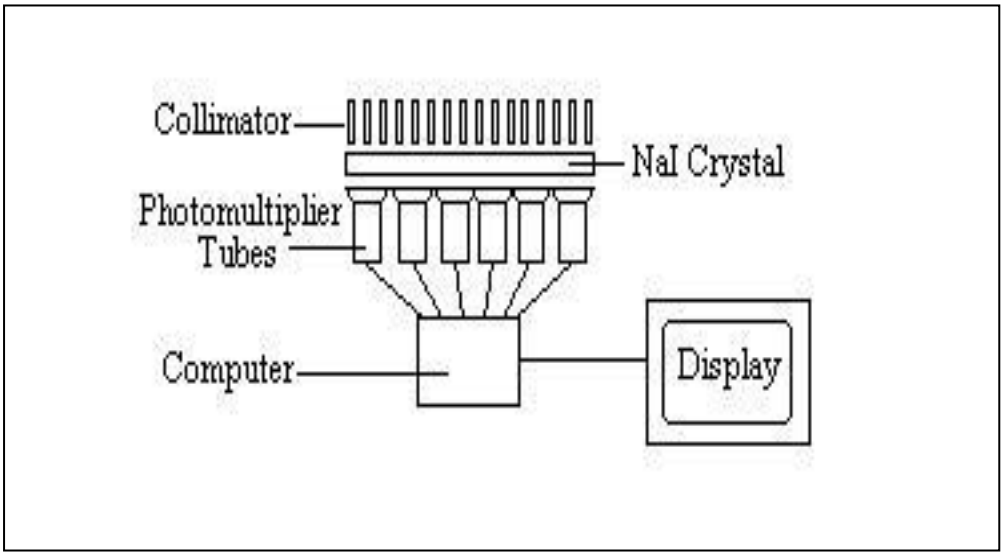


**Figure 2.4: Basic components of gamma camera.**

Gamma radiations are emitted in all directions; therefore a collimator is required to restrict the direction of the photons so that ideally each point in the image corresponds to a unique point in the source. A collimator is made of an absorbing high atomic number material, such as lead, tungsten or platinum. Lead is a popular choice for a collimator because it is the most economic. A parallel-hole collimator consists of thousand of holes that are parallel with each other and perpendicular to the detector face. The number of collimator holes depends on the diameter of the hole and the size of the septa. The collimator is attached to the face of the detector and ideally allows only gamma radiation that travel parallel to the axis of each hole to reach the detector and form an image. Gamma radiations emitted from other directions or with low energy are absorbed by the septa between the holes. Different types of collimator are used to channel gamma radiation emitted from different radionuclides. The features of the collimator are determined by the hole length, the diameter of the holes (hole size) and the thickness of the septum separating the holes (septa size). There are three types of collimator categorised according to different energies: low-energy (<140 keV), medium-energy (150–300 keV) and high-energy (300–400 keV) (Perkins, 1999). For example, low-energy collimator is designed for $^{99m}$Tc (140 keV); medium-energy collimator is for $^{123}$I (159 keV) and high-energy collimator is optimised for $^{131}$I (364 keV).

The function of the detector in a gamma camera is twofold. First it converts gamma radiation into visible light flashes by a scintillation crystal, and secondly these visible flashes are turned into electrical signal by PMTs. The scintillation crystal used in a gamma camera is typically made of sodium iodide with a trace of thallium, NaI(Tl). The choice of NaI crystal as detector is primarily due to the high density (3.67 g cm$^{-3}$) of the crystal and the high atomic number of iodine ($Z$=53) that correspond to high probability of photoelectric absorption for the energy range involved in nuclear imaging. Sodium iodide is doped with a trace amount (0.1% - 0.4%) of thallium as an activator, hence NaI(Tl) becomes more efficient at producing light photons after photons interact with it. Gamma radiation emerging from the body interacts with the crystal and produce visible lights. The scintillation detector has a unique property of creating scintillations or flashes of light after absorbing gamma radiation. As explained earlier, the gamma radiation interact via photoelectric, Compton and/or pair production mechanism, whereby NaI molecules are raised to higher energy states through ionisation or excitation. The excited states return to ground states by emitting light photons. Approximately 20–30 light photons are produced per 1 keV of energy. Light emission by the scintillator is proportional to the energy deposited in the material. Hence, it is possible not only to detect photons, but also to determine the energy of the photons detected.

The visible light is guided towards the photocathode on the photomultiplier tube (PMT). Then they are converted to electrons, multiplied and finally converted into an electrical pulse (or electrical signal) at the anode of each PMT. The PMTs outputs are subsequently processed and converted into three signals, two of which (*X* and *Y* signals) provide the spatial position of the scintillation and the third signal (*Z*-signal) gives the total energy deposited in the crystal by the gamma radiation. Pulse height analyser (PHA) is applied to *Z*-signal to retain events where the energy is within pre-set energy window. This is to reduce the number of photons that have undergone Compton scattering before interacting with the scintillation crystal. The position and the energy of the impinging photons which fall within a predetermined energy window are registered as counts and are used to produce projection of image and to quantify the activity distribution in the patient.

High spatial resolution and high sensitivity are two vital aim of radionuclide imaging but they always exist as trade-off between each other. Collimator choice and thickness of the crystal influence these two parameters. Better spatial resolution can be obtained by using a high-resolution collimator that has a smaller hole size, broad septa and a longer collimator length. However these will greatly reduce the sensitivity as majority of the gamma radiation is absorbed by the collimator septa. High-sensitivity collimator has bigger hole size and smaller septa, but will reduce the spatial resolution. Thickness of crystal may vary from 0.25 inch to 1 inch, with the usual crystal thickness in a gamma camera is ⅜ inch (0.95 mm). The sensitivity of the gamma camera versus gamma radiation energy for a range of NaI(Tl) crystal thickness is illustrate in Figure 2.5. It shows that for energies below 150 keV, the sensitivity of the gamma camera is nearly

100% for all crystal thicknesses. The sensitivity then decreases with increasing energy, depending on the crystal thickness. The sensitivity can be increased with a thicker crystal, but it will also increase multiple scattering within the crystal thus reduce the spatial resolution. Some gamma cameras, especially the ones that equipped with high-energy collimator are fitted with thicker crystal for better sensitivity, but this comes at the expense of some loss of spatial resolution.

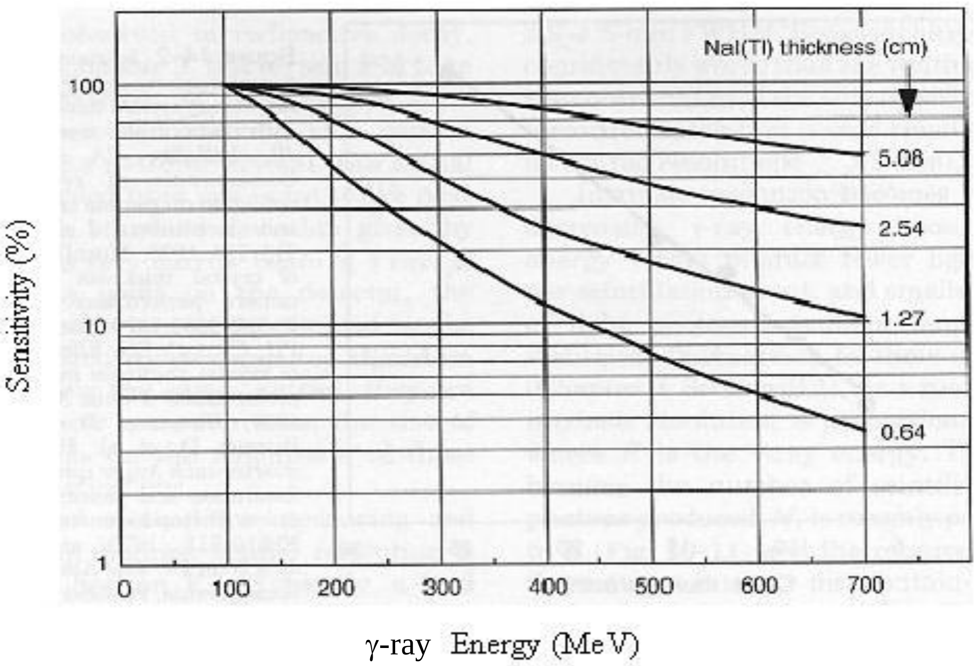


**Figure 2.5: Sensitivity of a gamma camera for different thicknesses of the NaI(Tl) crystal detector. Adapted from Cherry et al. (2003).**

Apart from the parallel-hole collimator, other designs of collimator have been developed to be used in specific imaging studies. The pinhole collimator, the converging collimator and the diverging collimator are design with different shapes and contain one or many holes to view a region of interest that is smaller or larger than the dimension of the crystal (Kimiaei et al., 1996; Moore et al., 1992; Peremans et al., 2005). Diverging, converging and pinhole collimators may be useful to change the field of view but the image distortion caused by the magnification with depth may be a problem. The different designs of these collimators are shown in Figure 2.6.

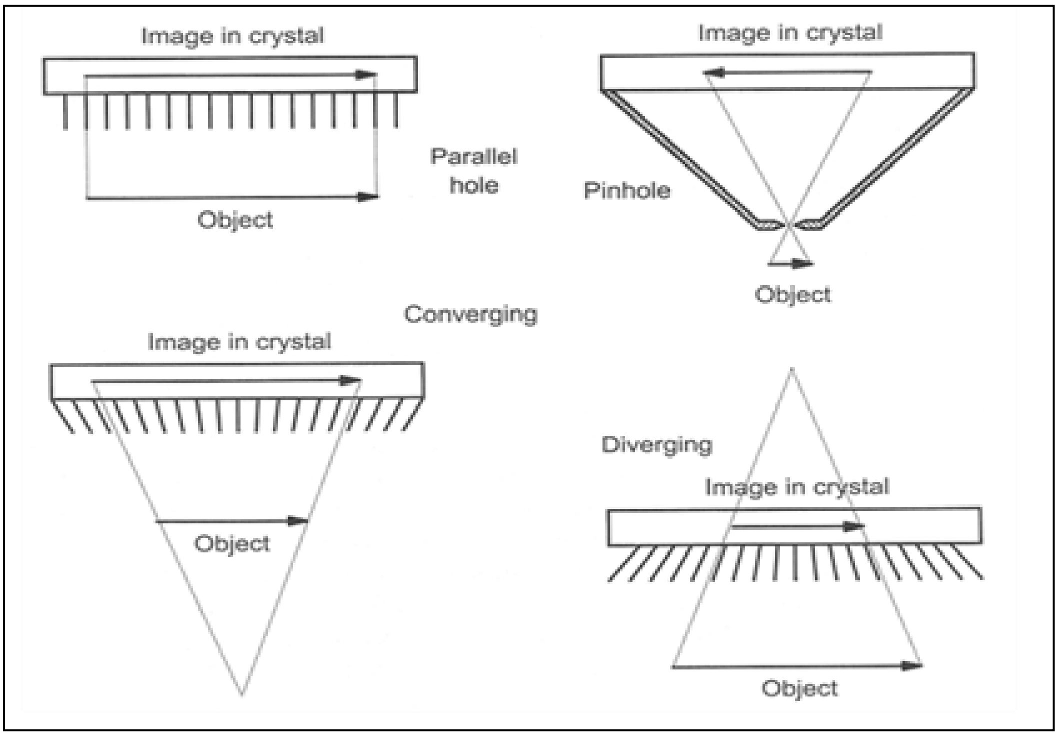


**Figure 2.6: Parallel, pinhole, converging and diverging collimator.**

### 2.2.2 Radionuclide therapy

The absorption of ionising radiation by cells always has the potential of harmful effects. The radiation may directly damage the cells or generate chemical changes that alter the biological properties of the cells which eventually lead to their destruction. Radiation can damage both cancerous and normal cells but most normal cells are able to repair themselves. However, cancerous cells that are rapidly dividing are particularly sensitive to radiation. For this reason, ionising radiation is used to control the growth of malignant cells by damaging and killing these cells. Therefore, the aim of radiation therapy is to deliver sufficient radiation dose to target tissues while minimising radiation dose to healthy tissues.

Radionuclide therapy (or radioimmunotherapy or ‘targeted’, or ‘molecular’ radiotherapy) is increasingly used to treat primary and metastatic cancer, as well as to reduce symptom by providing palliative pain relief (Perkins, 2008).

Radionuclide therapy is based on the use of radionuclides which are bound to antibodies or incorporated into conjugates (Hamoudeh et al., 2008; Sharkey & Goldenberg, 2006; Weiner & Thakur, 2005). The underlying principle of radionuclide therapy is based on the selective absorption of the agent in the lesion to be treated, and the radionuclides releasing radiation that will kill a tumour with minimal uptake by normal tissue (Perkins, 2008). In contrast to external beam therapy, radionuclide therapy is given internally and allows the radiation dose to be delivered locally. It is carried out by administering a radiation source into the target area to treat the disease or eradicate tumour cells. Some cancerous cells can spread to other parts of the body and form new tumours, known as metastases. For example, prostate and breast cancers may lead to multiple bone metastases. A single site may be treated with external beam therapy, but multiple sites of bone metastases will benefit more from radionuclide therapy because the radiopharmaceutical distributes as a tracer and concentrates in the target organ (Lewington, 1993; Pandit-Taskar et al., 2004). Furthermore in external beam therapy, only a limited area of the body is irradiated and high energies of gamma radiation are needed simply to penetrate tissue and reach tumour. This will cause damage to the healthy cells along the radiation path.

Several radionuclides are currently used in the radionuclide therapy. In nuclear imaging, radionuclides that emit gamma radiation are preferable because they can be detected externally. On the contrary, radionuclides that emit beta particles like $^{90}Y$, $^{32}P$, $^{89}Sr$, $^{153}Sm$, $^{186}Ho$ and $^{186}Re$ (Hamoudeh, et al., 2008; Kassis & Adelstein, 2005) are most widely used and have demonstrated to be valuable in radionuclide therapy. This is because a beta particle has a suitable path length in tissue and it minimises unwanted damage and side effects to non-target organs. The path length of emitted radiation from a beta-emitter is sufficient to enable radiation to target malignant cells via the crossfire effect (Enger et al., 2008). The crossfire effect can increase tumour killing better than non-radiolabelled antibodies. It irradiates tumour cells and its surrounding tumour cells that are not bound to the antibody. This effect is particularly beneficial in bulky tumours or tumours that are poorly vascularised (Kassis & Adelstein, 2005; Wagner, et al., 2002). Beta-emitting radionuclides are also preferable in radionuclide therapy because they have short ranges and therefore pose little hazard to medical staffs and family members of the patients.

### 2.2.3 Roles of radionuclide imaging in radionuclide therapy

Radionuclide therapy requires accurate administration of radionuclide activity. The knowledge of the radiation absorbed dose is important in order to ensure optimal and effective treatment. Radiation dosimetry plays an important role in treatment planning and is needed to detect and clarify the radionuclide distribution in the body. This is to predict the toxicity and efficacy of the radionuclide treatment by making sure that lethal radiation is delivered to target organs, and that damage to neighbouring non-target organs is minimised. The required data needed to determine the activity and absorbed dose in radionuclide therapy can be obtained by radionuclide imaging (DeNardo, et al., 2001). Imaging can also yield more accurate patient-specific dosimetry because the biokinetics in tumour and normal tissue depends on the patient. Patient-specific dosimetry allows every patient to receive a customised therapy plan involving the specific amount of activity (Brans et al., 2007; Flux et al., 2006).

Radionuclide imaging is conducted at various times before, during and after radionuclide administration (DeNardo, et al., 2001; Erdi, et al., 1996). Prior to the therapy, a low activity dose of the therapeutic radionuclide is administered into the body and its distribution is imaged to check the localisation of the radiopharmaceutical and whether the therapeutic dose to be injected will be effectively distributed (Bardiès et al., 2006). If the assessment shows that the patients are unlikely to benefit from the therapy, consequently the therapy will not be proceed to avoid unnecessary risk. If the pre-therapy imaging shows a positive outcome, radiation dosimetry calculations are employed to determine maximum and minimum activity to be administered. Imaging and dosimetry are also applied after treatment to confirm the therapeutic plan and to obtain information related to dose deposition and treatment efficacy.

Planar, SPECT and PET images can be used to estimate the radionuclide uptake. However some radionuclides are not suitable for imaging. Almost all radionuclides used for therapeutic purposes emit beta particles, although some of the radionuclides like $^{131}I$, $^{166}Ho$ and $^{188}Re$ are not pure beta-emitters. They also emit gamma radiation that can be used in imaging. Nevertheless sometimes the gamma energies are not optimal for imaging. It could be too high for effective detection or undergoes septal penetration that reduces the resolution (Bayouth & Macey, 1994). On the other hand, pure beta emitters like $^{90}Y$, $^{32}P$ and $^{89}Sr$ do not have primary gamma radiation that can be detected. In cases where the radionuclide is not suitable for imaging, a surrogate radiopharmaceutical which has the same chemical properties is used (Breitz et al., 1993; Clarke et al., 1999). Additionally, studies have shown that secondary photons called bremsstrahlung can be imaged for pure beta-emitting ($^{90}Y$, $^{32}P$ and $^{89}Sr$) radionuclides (Cipriani, et al., 1997; Clarke, et al., 1992; Shen, et al., 1994b). Planar scintigraphy and SPECT are both possible for bremsstrahlung imaging.

Recent studies also include the combined imaging modality of SPECT/PET with x-ray computed tomography (CT) which can provide both anatomical and functional data (Bardiès, et al., 2006; Chowdhury & Scarsbrook, 2008). Radionuclide imaging inherently has poor photon statistics because of the low activity administration and has modest spatial resolution. The image quality can also be degraded by physical factors such as photon attenuation and scatter radiation. In contrast, CT imaging is not suitable for functional imaging but can produce images with better spatial resolution. Moreover, CT data can generate a patient-specific map of attenuation coefficients and other anatomical data that can be used to correct data for error due to photon attenuation, scatter radiation and other physical effects. This shows that the combination of SPECT/PET with CT scans can provide rapid and accurate image correction for photon attenuation and scatter radiation thus improving both image quality and qualitative accuracy of the radionuclide imaging data (Buck et al., 2008; Sureshbabu & Mawlawi, 2005).

## 2.3 $^{90}$Y

$^{90}$Y is one of the radionuclides used in radionuclide therapy. $^{90}$Y is a neutron-rich radionuclide which is produced by neutron bombardment of $^{89}$Y in a reactor (Murthy et al., 2006). $^{90}$Y is considered as pure beta-emitter because it mainly decays to the daughter nuclide $^{90}$Zr by emitting a beta ($\beta^-$) particle. The decay process of $^{90}$Y is shown in Figure 2.7 below.

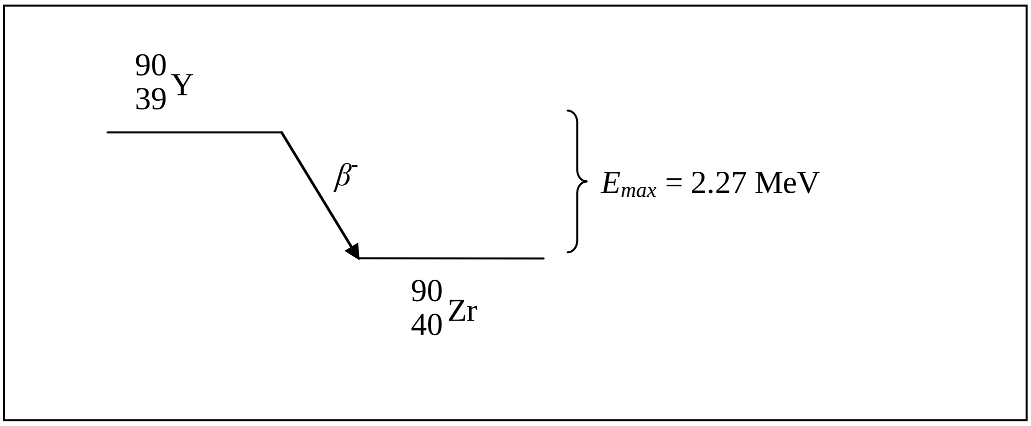


**Figure 2.7: $^{90}$Y decay scheme.**

$^{90}$Y is suitable for radionuclide therapy as it emits high-energy beta particles ($E_{max}$ = 2 .27MeV) which have a short range in tissue (~12 mm). This means that it delivers a high and localised radiation dose. 90% of the $^{90}$Y energy is absorbed within 5.2 mm in tissue (Berger, 1971), which is about the diameter of 100–200 cells. This path length gives $^{90}$Y a broad crossfire effect when bound to antibodies and conjugates (Wagner, et al., 2002). $^{90}$Y therapeutic administration is also of minimal radiation safety concern to hospital staff and family members (Hendrix, 2004). Due to its low hazard, patients do not require hospital stay and can be released immediately after treatment (Hendrix, 2004; Manjunatha & Rudraswamy, 2010; Zanzonico, et al., 1999). It has physical half-life of 64.2

hours which allows adequate time for radionuclide localisation and effective irradiation of the targeted area.

$^{90}Y$ is increasingly used in targeted radiotherapy to treat or provide palliative pain relief for various types of tumour and haematological malignancies. $^{90}Y$ is bound to antibodies, conjugates or encapsulated into tiny microspheres and administered internally into the body. $^{90}Y$ is bound to monoclonal antibody and is used in different types of cancer treatment especially non-Hodgkin's lymphoma (Friedberg, 2004; Wagner, et al., 2002) and neuroendocrine tumour (Druce, et al., 2009; Lewington, 2003). Selective Internal Radiation Therapy (SIRT) with $^{90}Y$ microsphere encapsulation is an effective treatment for primary and metastatic liver cancer (Gulec, et al., 2009; King, et al., 2008; Salem & Thurston, 2006). SIRT is a palliative treatment in which it slows down the tumour growth and alleviates symptoms. The treatment is performed by blocking off the blood supply that feeds the cancerous cells using tiny resin or glass beads called microspheres. The microspheres are embedded with $^{90}Y$ and are lodged at the tumour site to deliver high radiation dose (Hamami et al., 2009; Murthy et al., 2005).

$^{90}Y$ is also used for the treatment of arthritis and big joints such as the knee and is commonly used in radionuclide synovectomy (Kyle et al., 1983; Perkins, 2008; Taylor et al., 1997). $^{90}Y$ has a huge potential in radionuclide therapy and currently many other $^{90}Y$-labelled antibodies are being developed to be used in treatment of other type of cancers and diseases. Studies showed that $^{90}Y$-labelled antibodies also have prospects for ovarian (Alvarez et al., 2002), breast (DeNardo et al., 1997; Johnson et al., 2002), colon (Leichner et al., 1997) and liver (Yu et al., 2003) cancer treatment.

### 2.3.1 Imaging of $^{90}$Y distribution in radionuclide therapy

As discussed earlier, we can see that $^{90}$Y is optimal for therapeutic use. It is therefore important to determine the activity and dosimetry in the planning and assessment of the treatment procedure. This relies heavily on radionuclide imaging, but $^{90}$Y imaging is particularly challenging because of its short range. Different approaches are used to imitate the biodistribution of $^{90}$Y and to predict its dosimetry.

The lack of primary gamma radiation for direct imaging has led to the use of another radionuclide that emits gamma radiation and has chemical properties similar to the pure beta-emitter which will be eventually used in radionuclide therapy procedures (Clarke, et al., 1999). As in case of $^{90}$Y radioimmunotherapy, $^{111}$In is used as substitute tracer for imaging because it has chemical properties comparable to $^{90}$Y (Onthank et al., 2004). $^{111}$In emits two photons in cascade of energies 171 and 245 keV that are suitable for imaging. $^{111}$In imaging is performed to verify tumour targeting and to estimate potential radiation dose to tumour and normal organs (Clarke, et al., 1999; DeNardo, et al., 1997; Linden et al., 2005). However $^{111}$In activity distribution does not predict $^{90}$Y distribution completely (Carrasquillo et al., 1999; Jonsson et al., 1992).

Treatment evaluation of SIRT procedure is performed to assess $^{90}$Y biodistribution and to detect possible complications of shunting to the lung and deposition in the gastrointestinal tract (Hamami, et al., 2009; Murthy, et al., 2006). The pre-treatment imaging and the calculation of radiation absorbed doses to tumours and normal tissues are calculated based on the $^{99m}$Tc-labelled macro aggregated albumin ($^{99m}$Tc-MAA) study and computed tomography (CT) scans. It is assumed that $^{90}$Y follows MAA distribution and can be used as surrogate for imaging (Hamami, et al., 2009; Knešaurek et al., 2010; Sarfaraz et al., 2003; Sarfaraz et al., 2004). However due to the physical differences between $^{90}$Y and $^{99m}$Tc-MAA, the distributions of $^{90}$Y and $^{99m}$Tc-MAA *in vivo* may differ, and affect the dosimetry calculation and treatment planning overall (Knešaurek, et al., 2010).

A study on the $^{90}$Y has been performed previously and shows that the decay of $^{90}$Y has a minor (0.01%) branch to the 0+ excited state of $^{90}$Zr at 1.76 MeV (Ford, 1955; Johnson et al., 1955). This is followed by an internal conversion, internal $e^{+}e^{-}$ pair creation or two photon de-excitation (Ryde et al., 1961). Consequently, $^{90}$Y PET imaging was suggested to assess the biodistribution of $^{90}$Y-labelled therapeutic agents (Lhommel et al., 2010; Nickles et al., 2004). Nonetheless, $^{90}$Y has very low positron production, where $e^{+}e^{-}$ pair only occurs in 34 out of a million decays (Selwyn et al., 2007). PET-based dosimetry of $^{90}$Y also requires major financial investment and it is more challenging to obtain multiple images in PET (Hendee & Ritenour, 2002; Nickles, et al., 2004). PET quantification for $^{90}$Y therapy was also proposed by using surrogate isotopes like $^{86}$Y and $^{89}$Zr (Avila-Rodriguez et al., 2007; Barone et al., 2005; Helisch et al., 2004). However it requires extensive correction due to its complex decay process (Flux, et al., 2006). The surrogate isotopes have such short half-lives and must be produced in centres that are near, or have access to a cyclotron for the radionuclide's production. The time-activity curve of the surrogate radionuclides also does not reflect the complete biodistribution of $^{90}Y$ (Flux, et al., 2006).

It is known that electron interactions with matter produce secondary photon emission called bremsstrahlung. Since $^{90}Y$ does not produce gamma rays, its distribution can be imaged using planar gamma camera or SPECT by acquiring events of the bremsstrahlung production created from near the decay site of $^{90}Y$ (Mansberg, et al., 2007; Sebastian, et al., 2008; Shen, et al., 1994b). The advantages of bremsstrahlung imaging are that it represents the correct distribution of $^{90}Y$ compared to surrogate radiopharmaceuticals and it is more straightforward than PET imaging.

## 2.4 Bremsstrahlung Imaging

Bremsstrahlung imaging is an imaging technique using planar gamma camera or SPECT, where bremsstrahlung photons are acquired for the purpose of dosimetry in radionuclide therapy. So far, bremsstrahlung imaging is unique for radionuclides that primarily emit beta particles because they do not have or lack of primary gamma radiation which are required for imaging (Cipriani, et al., 1997; Clarke, et al., 1992; Shen, et al., 1994b).

As explained earlier, the physical components of the gamma camera have a huge influence on the quantitative and qualitative accuracy of the acquired image. Most gamma cameras are optimised for $^{99m}Tc$ because it is the most common radionuclide used in nuclear imaging. $^{99m}Tc$ emits photons with a distinct photopeak energy of 140 keV. Collimators are also designed for higher or lower radioisotope energies, and can be optimised for higher resolution or higher sensitivity. Energy window selection is also critical because a small energy window reduces sensitivity but a large energy window will include low-energy scattered photons and reduces resolution. The selection of collimator and energy windows represents a practical compromise between spatial resolution and sensitivity, thus it is important to choose the right collimator and energy window to obtain optimal imaging condition.

Bremsstrahlung imaging has been employed in the planning and assessment of the radionuclide therapy. However, bremsstrahlung imaging is rather complex because conventional gamma radiation imaging methods cannot be easily applied to bremsstrahlung imaging. Bremsstrahlung photons have a broad energy spectrum ranging from zero to the maximum beta energy and the distinct photopeak in energy spectrum does not exist, making the choice of collimator and energy window difficult. As discussed earlier, bremsstrahlung photons production depends on the incident electron energy and the atomic number, $Z$, of the material where it traverses. This means that bremsstrahlung events are few in a medium like tissue. This significantly reduces the sensitivity of the system. In order to increase photon counts, a large energy window can be applied but this decreases the resolution as it is hard to distinguish primary and scattered photons. The scattered photons produced from high-energy photons interactions can also be accepted in the energy window. Additionally, the bremsstrahlung photons are produced at varying distances from the decay site, limiting the accuracy of the original position determination.

Bremsstrahlung imaging has been performed in numerous studies of radionuclide therapy using suitable selection of collimator and energy window (Ito, et al., 2009; Mansberg, et al., 2007; Murthy, et al., 2005; Sebastian, et al., 2008) but the combination of collimator type and energy window varied for different research groups. The studies are mainly focus on finding the optimal selection of collimator and energy window (Heard, et al., 2004b; Rault et al., 2007; Shen, et al., 1994b). Other studies of bremsstrahlung imaging include the correction methods to improve the quality of the images (Minarik et al., 2009; Shen et al., 1994a; Siegel & Khan, 1996) to improve the quality of image.

It has previously been shown that in bremsstrahlung imaging, low-energy collimators surpass medium- and high-energy collimators in term of sensitivity. However imaging using the low-energy collimator produced images with poorer spatial resolution (Shen, et al., 1994b). Medium-energy general-purpose (MEGP) collimator and a very broad energy window (55–285 keV) were suggested for optimal imaging. However characteristic x-rays photons produced from lead collimator were also included in an energy window with a lower limit below 80 keV (Cipriani, et al., 1997; Clarke, et al., 1992; Shen, et al., 1994b). The best contrast was obtained when using smaller energy windows (100–150 keV) where the full-width at half-maximum (FWHM) at 2.5 cm was 8 mm (Heard, et al., 2004b). Currently, some researchers and treatment centres use a MEGP collimator with energy window ranging between 70–120 keV (Mansberg, et al., 2007; Sebastian, et al., 2008). MEGP collimators suffer more contamination but offer a better resolution and contrast recovery than the high-energy collimators for a fixed energy window (Rault, et al., 2007). Minarik et al. (2008) chose to use a HEGP collimator with an energy window ranging from 105–195 keV because the energy window setting showed a good compromise between the low count rate generally obtained in bremsstrahlung imaging, and the increased probability of septal penetration by higher energy photons.

The quality of the images obtained from bremsstrahlung imaging is affected by a number of factors, namely high noise due to low sensitivity, scatter of photons inside patient and collimator, photon penetration through collimator septa and backscatter from camera housing to the crystal. The correction methods for bremsstrahlung imaging are also under on-going research (Minarik, et al., 2009; Shen, et al., 1994a; Siegel & Khan, 1994) so they can be employed effectively to obtain better and acceptable images.

## 2.5 Monte Carlo simulation in nuclear medicine

Monte Carlo methods are numerical calculation methods used to solve mathematical or statistical problems using a random variable sampling to determine the properties of some phenomenon. Monte Carlo technique can be used to solve radiation transport using the existing knowledge of radiation interaction processes. Nowadays, Monte Carlo simulations are widely used in nuclear medicine imaging. The method has been applied in a wide range of problems that could not be easily addressed using experimental or analytical approaches. It is an essential tool to assist in, among others, the design of new medical imaging devices, improvement of image reconstruction method, compensation of attenuation and scatter as well as evaluation of imaging techniques (Zaidi, 1999, 2006). The use of Monte Carlo techniques is rising because of the availability of powerful codes and the increase in computing power.

In order to do Monte Carlo calculations, information about the occurring physics processes in the simulations is needed. This information is expressed in the form of probability distribution functions. When simulating particle interactions, a cross-section data which represent such information is used to calculate the path length and the type of interactions. These probability distribution functions are sampled by predefined sampling rules using randomly generated numbers. The energy of such a particle can be dissipated along its path or the particle can penetrate the media to reach the detector where a new probability distribution function sampling decides whether it should be accounted for in the scoring region, or whether it should be discarded.

The radiation transport is ideal to be simulated using Monte Carlo methods since the interaction processes for particles are well known and the precise cross section data are available. In a Monte Carlo simulation, a particle is tracked from creation until termination, with all decisions (starting energy, location of interaction, scatter angle, etc.) are based on the interaction physics, extensive cross section table and pseudo-random numbers. A particle is created by sampling a source's energy together with starting location and its initial direction. In the transport phase, for each interaction type and location are sampled, together with the remaining energy and new direction. This process is repeated until the source particle and all its secondary particles have deposited all their energies or escape the simulation geometrical boundary. The process is repeated for a predefined number of creations.

Major limitation of Monte Carlo methods is linked to the statistics required to accurately simulate a given experimental setting. The required quantities of interest can be calculated by obtaining the distribution of the number of simulated particle which is called history. The statistical uncertainty of the calculation depends on the number of particle histories simulated, $N$ and decreases by $\sqrt{N}$. This means that $N$ has to be very high and therefore implies heavy computing power and simulation time. In gamma camera, only 1 out of 10 000 emitted gamma radiations will actually pass the collimator and be detected. This illustrates how inefficient this process in term of statistics perspective. In the Monte Carlo simulation, the uncertainty, $\sigma_x$ of the quantity $x$ can be estimated using

$$\sigma_x = \sqrt{\frac{\sum_{i=1}^{N}(X_i - \bar{X})^2}{N(N-1)}} \tag{2.3}$$

where $\bar{\boldsymbol{X}}$ is the sample mean and $\boldsymbol{X_i}$ is the value of the score associated with the i-th history.

Monte Carlo simulation of photon histories is performed by using a detailed scheme, in which all interactions undergone by the transported photons are simulated in chronological sequence. This strategy is also applicable to other kind of radiation that has small or moderate number of interactions. A photon history terminates after a single photoelectric or pair production interaction, or after a few Compton interactions. This means that a photon undergoes a small number of interactions, and detailed simulation of photon transport is a simple task and employs short simulation time. However, simulation of an electron (and positron) is much more difficult than a photon. The main reason is that the average energy loss of an electron in single interaction is very small, and therefore electrons, especially those with high-energy suffer large number of collisions before being slowed down. The simulation of electron transport is a time consuming process due to the frequent interactions of electrons. Unlike photons, an electron undergoes many interactions before it loses all its energy. For example, for 1.5 MeV electrons over a thousand steps are needed before all energy is deposited. Therefore, it is unrealistic to track all electron interactions event by event. To overcome this difficulty, the condensed history method is used in Monte Carlo radiation transport simulation where the path of the electron is divided into series of step. This technique is possible because in most cases, the single collision of electron only causes small changes in the electron's energy and/or direction. The combined effects of many small individual interactions during one step are grouped into a single, large-effect condensed history step (Chetty et al., 2007). A multiple scattering theory is used to account for the elastic and inelastic scattering during this step (Kawrakow & Bielajew, 1998; Vilches et al., 2007). The condensed history transport for electron and positron is used in all general purpose Monte Carlo packages; however the simulation time is still rather long.

There are several Monte Carlo codes used in the area of medical physics and they can be divided into two categories: general purpose and user specific. Examples for general purpose codes are Geant4, EGS and MCNP. Alternatively, specific codes are developed for specific situation, such as SIMIND, SimSET and GATE which are developed specifically for Monte Carlo simulations in emission tomography.

There are several advantages of the general purpose codes. They are widely used, well documented, extensively tested and validated for many purposes and energy ranges. These codes are well maintained and supported, continuously evolving and updated with the current software and hardware capabilities. Its implementation effort is also shared by a large community to ensure long term support and maintenance.

## 2.6 Summary

From the reviews, it is quite clear that therapy using $^{90}$Y has a lot of benefits and thus bremsstrahlung imaging is an emerging field in nuclear medicine. Monte Carlo simulation is a reliable method and beneficial to study bremsstrahlung imaging because it is able to simulate a model similar to a real physical system. However, it is known that large number of particle histories must be simulated to decrease statistical uncertainty in the Monte Carlo calculations. The Monte Carlo simulation of $^{90}$Y bremsstrahlung imaging is especially time consuming. This is because the production of bremsstrahlung photons is low in body tissues and Monte Carlo simulation of electron transport is also notably slow. It is therefore useful to find a way to achieve an acceptable computing time for simulation of bremsstrahlung imaging. Because of these aspects associated with Monte Carlo simulation of $^{90}$Y bremsstrahlung, it is useful to find a way to speed up the simulation time.

# CHAPTER 3

# GEANT4 TOOLKIT

## 3.1 Introduction

This chapter gives an overview of the Geant4 Monte Carlo toolkit which is used in this research.

## 3.2 Geant4

Geant4 (Agostinelli et al., 2003) is a general purpose Monte Carlo code and its applications are widespread. It is most commonly used to investigate particle and nuclear physics, accelerator design, medical physics and space science. Geant stands for 'Geometry and Tracking' and it is a platform for the simulation of particle passage and interactions through matter. The Geant4 toolkit is an open source collection of C++ classes. It is based on object-oriented C++ programming. Object-oriented software design has high modularity and re-usability. The Geant4 toolkit can be publicly downloaded from the Geant4 website (http://geant4.web.cern.ch/geant4/), which includes all the C++ source code. The web also provides an extensive documentation and tutorial examples which shows the complete applications of Geant4. The toolkit can be installed in several supported platforms (Linux, SUN and Windows). Moreover, it can be interfaced with several visualisation tools like VRML, OpenGL and DAWN.

Geant4 was developed by a collaboration of about 100 scientists in Europe, Japan, United States, Canada and Russia.

Geant4 was used in this research because it has been extensively tested, well documented, well maintained and provides reliable results. Geant4 is also flexible and allows modification to meet different application needs. Geant4 is capable of simulating the transportation of most particles through any material. It provides for various types of particle (for example, electrons, photons, protons, quarks, ions and others). The Geant4 toolkit includes all aspects of the simulation process, such as geometry and materials involved, particle of interest, the generation of primary events, particles tracking through materials and electromagnetic fields, the physics process governing particle interactions, the response of sensitive detector components, the generation of event data and the visualisation of the detector and particle trajectories. Geant4 uses standard high-energy physics and to extend its application in medical physics, very low energy processes down to tens of eV are included in Geant4. It allows generation and tracking of optical photons from scintillation inside detection crystals. However, Geant4 is rather complex and very difficult to learn, the installation process could be tiresome and lead to serious errors that can only be understood by experts. Luckily Geant4 provides an online forum site for user to discuss and enquire about problems that arise. Efforts to improve the code in term of its accuracy and usability are continuously being made by the developers.

## 3.3 Geant4 features

Geant4 requires the user to write his/her own C++ programming using classes which inherit behaviour from Geant4 classes. The user must define three mandatory classes which are derived from the base classes provided by Geant4. These base classes are the G4VUserDetectorConstruction, G4VUserPhysicsList and G4VUserPrimaryGeneratorAction classes.

### 3.3.1 G4VUserDetectorConstruction

The G4VUserDetectorConstruction class controls the definition of the geometric and material setup. In Geant4, the geometry is made of a number of volumes. The largest volume is called 'World' and contains all other volumes in the detector geometry. Geant4 has a set of pre-programmed shapes present in its source code that can be assembled in a hierarchy of volume. The volume hierarchy is used as a way of placing volumes inside previous volumes (known as daughter and mother volumes, respectively, in Geant4). Each volume is created by describing its shape, physical characteristics and its placement in World. The materials used in the simulations are defined by their densities, isotope or element compositions. The element composition can be specified by the number or atoms in a molecule, the mass per molecule or the fractional mass of each component. Several other properties like detector sensitivities and visualisation attributes are also defined in this class. A volume is marked as 'sensitive' for scoring so that a certain user-defined code is activated as soon as a particular set of particles passes through it. A 'hit' is a snapshot of the physical interaction of a track in sensitive region of the detector. For each hit, a variety of information from the track can be stored, such as the kinetic energy of the particle or the geometrical information of the hit. Geant4 provides a large set of solids of different complexity and allows an efficient repetitive structure representation. Geant4 capability to build repetitive structure is especially useful in this research to define the arrays of collimator holes.

### 3.3.2 G4VUserPhysicsList

The G4VUserPhysicsList class describes the type of particles, physics processes, models and the particle range cuts which are customized to its specific type of applications. Within this class, all particles and physics processes to be used in the simulation must be defined. A complete physics setup that contains all this information is termed a 'physics list' in Geant4. All the particles which are used in the simulation including secondary particles must be defined by the user to ensure that these particles are created or generated by the physics that is used.

Physics processes describe how particles interact with materials. Geant4 provides seven major categories of process: electromagnetic, hadronic, transportation, decay, optical, photolepton hadron and parametrisation. The electromagnetic physics packages manage the electrons, positrons, photons, optical photons, muons, hadrons and ions. For electromagnetic physics, two models are available, namely standard and low-energy.

The range cut-off parameter is also defined in this class. Usually most Monte Carlo codes impose an energy cut-off, where particle is stopped when the energy is reached. Any remaining energy of the particle is dumped at that point. Therefore, the use of cut-off energy may cause imprecise stopping location and energy deposition as the range of particle depends on the particle type and the material it traverse. In Geant4, a production threshold is imposed. The production threshold is defined as the distance (or range cut-off) which is internally converted to energy for each material and particle type so that the particle with threshold energy stops (or is absorbed) after travelling the range cut-off distance. A range cut-off is basically a low-energy limit on a particle production. Below the threshold no secondary particles will be generated. Production threshold for photon, electron and positron is set as 1 mm by default but it should be defined based on the application by the user. Table 3.1 demonstrated the different range cuts and the converted production energy thresholds in different materials used in this study. In our simulation, the range cut parameter was set to 1 $\mu$m, and this range was converted to a production energy threshold. Only one value of production threshold distance is used for all materials because it corresponds to different energies depending on the material. The gamma production threshold for a given material is used to separate the continuous and discrete parts of the process. Below the threshold the emission of soft photons is treated as a continuous energy loss. For bremsstrahlung above a given threshold energy, the energy loss is simulated by the explicit production of photons.

**Table 3.1: Energy cuts in Geant4 corresponding to the difference range cuts and materials used in this work**

| Range cut ($\mu$m) | Material | Energy cut for electrons (keV) | Energy cut for gammas (keV) |
|---|---|---|---|
| 1.0 | Water | 1 | 1 |
| 1.0 | Adipose tissue | 1 | 1 |
| 1.0 | Bones | 1 | 1 |
| 1.0 | Lead | 6.75 | 1 |
| 1.0 | NaI(Tl) | 1.40 | 1 |
| 100.0 | Water | 85 | 1 |
| 100.0 | Adipose tissue | 82 | 1 |
| 100.0 | Bones | 111 | 1.85 |
| 100.0 | Lead | 241.52 | 29.48 |
| 100.0 | NaI(Tl) | 132.80 | 7.33 |

Geant4 has different packages for electromagnetic physics which are specialised for different particle types, energy range or approach in the physics modelling. In the Geant4 updated version of 9.3, the electromagnetic physics are divided to two main configurations, the *standard* and *low-energy* electromagnetic physics. (In the earlier versions, the electromagnetic physics are divided into three: standard, low-energy and Penelope). Penelope (PENetration and ENErgy Loss of Positrons and Electrons) is a FORTRAN77 Monte Carlo code for the simulation of electromagnetic showers which can handle electrons, gamma-rays and positrons. In the new version, Penelope physics is included in the low-energy electromagnetic package. The migration to the new versions improves the computing performance without significant changes on the physics outcome. All the physics processes are well founded both theoretically and experimentally.

The standard electromagnetic physics package describes the interaction of the particles in the energy range of 1 keV−100 TeV. All main photon and electron interactions are included, except Rayleigh scattering and atomic relaxation. The low-energy physics category provides alternative electromagnetic physics model. In this package, the treatment of photons and electrons covers the energy range from 100 GeV and is extended and verified down to 250 eV. It models all interactions as well as Rayleigh scattering and atomic relaxation. All physical models present in Geant4 are continuously being tested and updated.

The low-energy processes are based on the publicly distributed Livermore evaluated data libraries database: EPDL (Evaluated Photons Data Library), EEDL (Evaluated Electrons Data Library) and EADL (Evaluated Atomic Data Library) to provide data for the determination of cross sections and the sampling of the final state. The physics used in Geant4 is explained in detail in the Physics Reference Manual which also can be downloaded from the website.

The Monte Carlo simulations in this study are carried out using the low-energy electromagnetic physics model and account for beta decays, electrons and photon interactions. Although the low-energy electromagnetic model takes more computer time than the standard electromagnetic model, this low-energy model was considered more appropriate in this research since it was specifically designed for better performance at the appropriate energy region and is recommend for use in medical physics. An overview of the physics processes and models employed for different particles in this research is shown in

Table 3.2. According to Geant4 terminology, the particle type ‘generic ion’ represents all nuclei except $^{1}H$, $^{2}H$, $^{3}H$, $^{3}He$ and $^{4}He$.

**Table 3.2: Geant4 processes and models for different particles used in this simulation work**

| Particle type | Physics process | Model |
|---|---|---|
| Gamma | Rayleigh scattering | G4LivermoreRayleighModel |
| | Compton scattering | G4LivermoreComptonModel |
| | Gamma conversion | G4LivermoreGammaConversionModel |
| | Photoelectric effect | G4LivermorePhotoElectricModel |
| Electron | Ionisation | G4LivermoreIonisationModel |
| | Bremsstrahlung | G4LivermoreBremsstrahlungModel |
| | Multiple scattering | G4eMultipleScattering |
| | Annihilation | G4eplusAnnihilation |
| Generic ion | Radioactive decay | G4RadioactiveDecay |
| | | G4ionIonisation |

### 3.3.3 G4VUserPrimaryGeneratorAction

The third mandatory class, G4VUserPrimaryGeneratorAction class controls the generation of the primary particles of the simulation. This class is used to define the primary particle, its energy, initial position and emission direction. Geant4 provides three G4VPrimaryGenerator concrete classes: G4ParticleGun, G4GeneralParticleSource and G4HEPEvtInterface. For many applications G4ParticleGun is sufficient. It has several virtual classes whose methods are overridden to specify how the primary event should be generated. However, G4GeneralParticleSource (GPS) is a simpler way to specify the more sophisticated source particles. GPS offers many options to generate the primary particles. The emission position distribution can be defined using several basic shapes that contain the starting point of source particles. It can be described as point, planar, surface or volume source. The angular distribution can be set to specific angle to control the directions in which the photons are emitted. Generally there are three main choices of angular distribution: isotropic, cosine-law or user-defined histogram. The energy distribution defines the energies of the photons. The input energy can be set using several built-in functions or by a user-defined histogram. Detailed explanation of GPS can be obtained from http://reat.space.qinetiq.com/gps/.

### 3.3.4 User classes

Apart from the mandatory classes, Geant4 also provides five other user classes namely G4UserRunAction, G4UserEventAction, G4UserStackingAction, G4UserTrackingAction and G4UserSteppingAction. In each of these classes there are several virtual methods which can be overridden by the user to gain control of the simulation at various stages of the simulation. The functions for each class in Geant4 are summarised in Table 3.3. Further information on the Geant4 toolkit can be obtained from their website that contains extensive documentation.

**Table 3.3: Functions of the mandatory and optional classes in Geant4**

| Class | Function |
|---|---|
| *Mandatory* | |
| G4VUserDetectorConstruction | Define geometrical and material setup, as well as sensitive detector for scoring and visualisation |
| G4VUserPhysicsList | Define particle types, physics processes and range cuts |
| G4VUserPrimaryGeneratorAction | Define the primary particle, its energy, position and emission direction |
| *Optional* | |
| G4UserRunAction | Define and store histogram |
| G4UserEventAction | Analyse simulation data |
| G4UserStackingAction | Customise priority of tracks |
| G4UserTrackingAction | Create trajectories |
| G4UserSteppingAction | Kill/ suspend a track |

# CHAPTER 4

# CHARACTERISTICS OF BREMSSTRAHLUNG PHOTONS FROM BETA DECAY

## 4.1 Introduction

This chapter describes the characteristics of the bremsstrahlung photons produced from beta decay. The emission processes of three beta-emitting radionuclides that are commonly used in nuclear medicine, namely $^{90}$Y, $^{32}$P and $^{89}$Sr were simulated in different materials. By understanding the characteristics of bremsstrahlung photons produced from beta decays, a kernel-based photon source can be developed. The results obtained can also be used to predict the sensitivity and the spatial resolution of a collimator.

## 4.2 Method

In order to investigate the characteristics of the bremsstrahlung photons produced from beta decay, the radionuclides that emit beta particles, $^{90}$Y, $^{32}$P and $^{89}$Sr point sources were simulated. The basic physical properties of these radionuclides are shown in Table 2.1. The point source was simulated as being placed at the centre of a 3 cm radius spherical volume of an absorbing material. The radius was chosen to ensure that the emitted electrons would release all their kinetic energy within the sphere. The beta particles were emitted isotropically, that is uniformly in all directions, and interacted with the material. Geant4 code was used to simulate $1\times10^9$ beta particle decays from the point source and to track their subsequent interactions in the absorber. The accuracy of the bremsstrahlung photon as simulated by the Geant4 Monte Carlo was validated by comparing the measured and simulated bremsstrahlung photon energy PDF (Figure 4.1). The measured data was obtained from the work published by Rault et al.(2010). The graph shows that simulated spectrum overestimated the contribution of the low-energy bremsstrahlung photons and underestimated the high-energy bremsstrahlung photons.

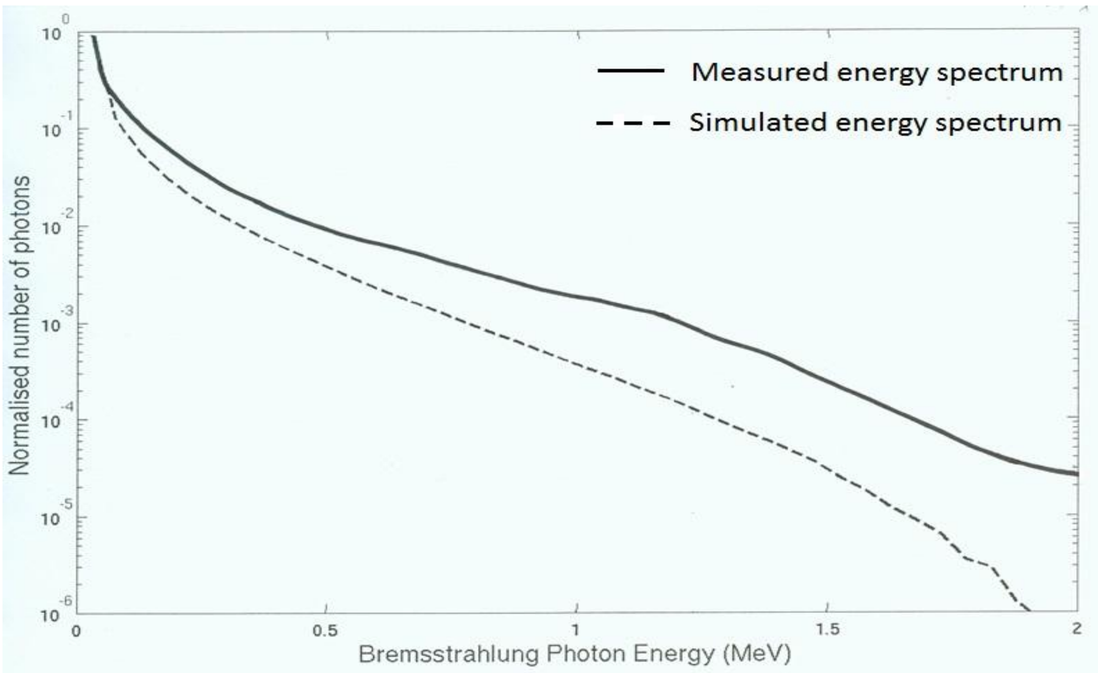


**Figure 4.1: Comparison of measured and simulated bremsstrahlung photon energy PDF.**

The distribution of the bremsstrahlung photons used in this study was obtained by recording the occurrence of bremsstrahlung emission as randomly simulated by Geant4. The energy cut-off was set to 1 keV. The production threshold was set low in order to simulate all physics as well as possible. For every first bremsstrahlung event generated by a beta particle, the energy, interaction position and emission angle of the photon were recorded. The emission angle was defined as the angle between the direction of a line from the point source to the bremsstrahlung emission point and the direction in which the bremsstrahlung is emitted. This angle can only be in the range of 0 degrees (i.e. bremsstrahlung travelling directly away from the point source) up to 180 degrees (i.e. bremsstrahlung travelling directly towards the point source).

Only the first event of bremsstrahlung produced by the beta particles was considered. This is because the total number of bremsstrahlung photons produced from the secondary electrons is relatively few and is not much difference from those produced from the primary electrons. This is demonstrated from initial $^{90}Y$ simulation and the comparison is illustrated in Figure 4.2 below. We can see from the graph that the energy spectra of bremsstrahlung photons produced from primary and secondary electrons are similar and do not really affect the outcome of the simulation. Further observation shows that bremsstrahlung photon produced from secondary electron were mostly in the low energy range. In the energy range of interest in this study (that is above 50 keV), bremsstrahlung events from both primary and secondary electron are only 0.02% more than those produced from primary electrons only. In fact, at higher energies, the primary bremsstrahlung dominates.

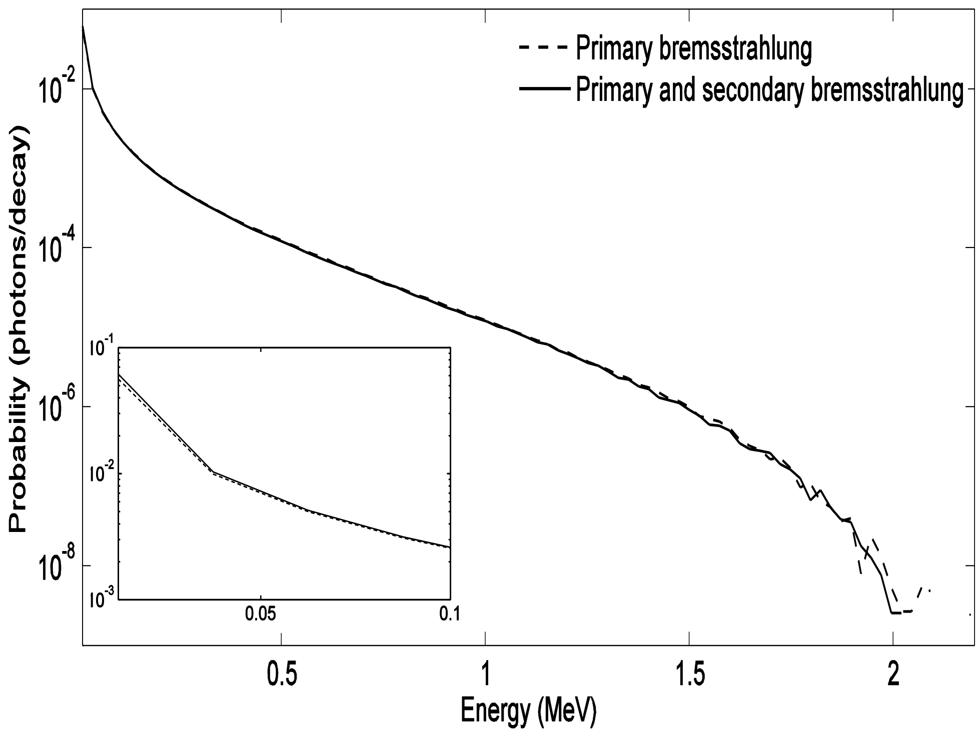


**Figure 4.2: Energy spectra for primary and secondary bremsstrahlung generated from a $^{90}Y$ point source in water. The smaller diagram shows an enlarged section at lower energy range for better comparison.**

The generation of the bremsstrahlung photons by different radionuclides was simulated in different absorber materials, namely water, adipose tissue and bone. The elemental compositions of the materials used in this simulation are listed in Table 4.1. The physical properties of these materials are shown in Table 4.2. The energy spectrum, spatial and angular distributions of the generated bremsstrahlung photons were then aggregated and normalised to obtain the probability distribution functions.

**Table 4.1: Composition of the different phantom material used in the Monte Carlo simulation performed in this work. The tabulated values correspond to the fractional mass of its component in each material, given in percentage**

| Fractional mass (%) | Water | Adipose tissue | Cortical bone | Air |
|---|---|---|---|---|
| Hydrogen | 11.2 | 11.2 | 3.0 | - |
| Carbon | - | 59.8 | 15.5 | 0.01 |
| Nitrogen | - | 0.9 | 4.2 | 75.53 |
| Oxygen | 88.8 | 27.8 | 43.5 | 23.18 |
| Calcium | - | - | 22.5 | - |
| Phosphorus | - | - | 10.7 | - |
| Sodium | - | 0.1 | 0.1 | - |
| Magnesium | - | - | 0.2 | - |
| Sulphur | - | 0.1 | 0.3 | - |
| Chlorine | - | 0.1 | - | - |
| Argon | - | - | - | 1.28 |

**Table 4.2: Properties of absorber material used in this simulation work (Hendee & Ritenour, 2002).**

| Material | Water | Adipose tissue | Bone |
|---|---|---|---|
| Effective atomic number $Z_{eff}$ | 7.4 | 5.9–6.3 | 11.6–13.8 |
| Density (kg/m$^3$) | 1.00 | 0.91 | 1.85 |

## 4.3 Results

The beta energy spectra for $^{90}Y$, $^{32}P$ and $^{89}Sr$ as simulated by Geant4 are shown in Figure 4.3. The beta particle energy spectra have continuous energies ranging from zero to the end-point of maximum energy value. $^{90}Y$ emits electrons with the highest energy, with a maximum energy of 2.27 MeV, followed by $^{32}P$ and $^{89}Sr$ which have maximum energies of 1.70 MeV and 1.47 MeV respectively.

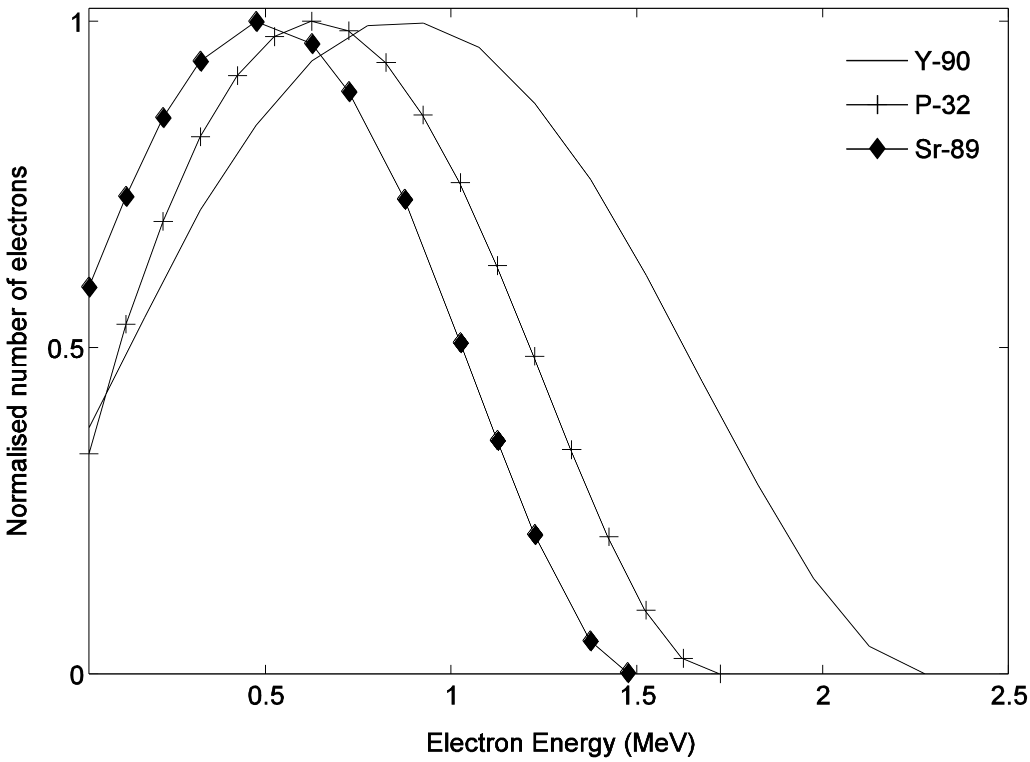


**Figure 4.3: Beta energy spectra for $^{90}Y$, $^{32}P$ and $^{89}Sr$ .**

The production probability, energy spectra, radial and angular distributions of the bremsstrahlung photons generated by the beta emissions in all of the materials were determined. $1\times10^9$ of beta particle emissions were simulated for each radioisotope, and the simulation time was $8\times10^3$ minutes on an Intel Xeon CPU running at 2.66 GHz with 8 GB RAM.

The bremsstrahlung yield generated in different materials from different radionuclides is presented in Table 4.3. For the purpose of comparison, the bremsstrahlung yield was calculated relative to the value obtained from $^{90}Y$ simulation in water and this is indicated between brackets. It can be seen that the bremsstrahlung yield was influenced by the incident electron energy and the effective atomic number, $Z_{eff,}$ of the medium. For $^{90}Y$ decays which have average electron energy of 0.94 MeV, only 8.6% of the decay produced bremsstrahlung photons in water. For $^{32}P$ and $^{89}Sr$ which have lower average energies than $^{90}Y$, the bremsstrahlung production in water was 6.0% and 4.7% correspondingly.

As shown in Table 4.1, bone has the highest effective atomic number and adipose tissue has the lowest effective atomic number. The effective atomic number of bone is about twice the effective atomic number of adipose tissue. The atomic number of absorbing medium influences the bremsstrahlung output. For each radionuclide simulation, the bremsstrahlung photon yield was highest in bone and least in adipose tissue; and their difference was approximately a factor of 2. The bremsstrahlung yield was least efficient for $^{89}Sr$ source in adipose tissue. Figure 4.4 shows the comparison of bremsstrahlung yield probability from $^{90}Y$ point source decay for water, bone and adipose tissue. The relative shape of the bremsstrahlung spectrum is independent of the atomic number of the absorber and is the same for all materials. However, the probability of bremsstrahlung emission in adipose tissue was similar to that of water, whereas the probability of bremsstrahlung emission in bone was almost doubled, due to its higher effective atomic number.

**Table 4.3: Bremsstrahlung yield obtained from the simulation of beta point source emissions. The bremsstrahlung yield relative to the value obtained from $^{90}$Y simulation in water is indicated between brackets**

| Radionuclide | Bremsstrahlung yield (%) | | |
|---|---|---|---|
| | Water | Adipose tissue | Bone |
| $^{90}$Y | 8.6 (1.00) | 7.4 (0.86) | 14.2 (1.65) |
| $^{32}$P | 6.0 (0.70) | 5.0 (0.58) | 9.6 (1.12) |
| $^{89}$Sr | 4.7 (0.55) | 3.9 (0.46) | 7.6 (0.88) |

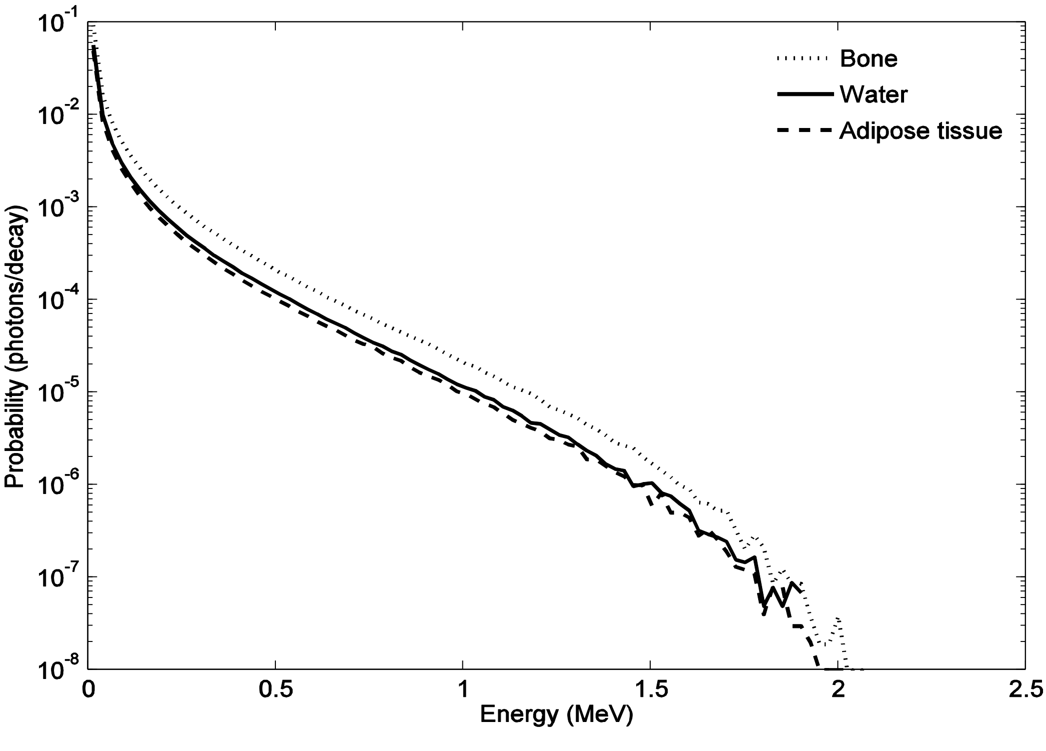


**Figure 4.4: Comparison of bremsstrahlung photons energy spectra generated from a $^{90}$Y point source in water, bone and tissue.**

Bremsstrahlung photon energy spectra, angular and radial distance distributions around the beta sources were obtained by aggregating all bremsstrahlung events from the initial beta simulations. The bremsstrahlung photon energy spectra are broad and continuous, although the figure shows the spectrum as being ‘binned’ in increments of 50 keV (Figure 4.5). When a radionuclide undergoes beta decay, the electron carries off a portion of the energy given up by the nucleus. The bremsstrahlung photons can have energies that range from 0 to the maximum kinetic energy, $E_{max}$, of the incident electrons, which is demonstrated by each of the radioisotope. However, the probability that an electron generates a photon with energy equal to its kinetic energy is very low. Most of the bremsstrahlung photons have energies below 50 keV. For $^{90}$Y decay in water, only 1.9% of the beta decays produced photons with energies above 50 keV. The fraction of high-energy bremsstrahlung photons was much lower for $^{32}$P and $^{89}$Sr. Only 1.2% and 0.8% of the bremsstrahlung photons were produced with energies above 50 keV for $^{32}$P and $^{89}$Sr emissions correspondingly.

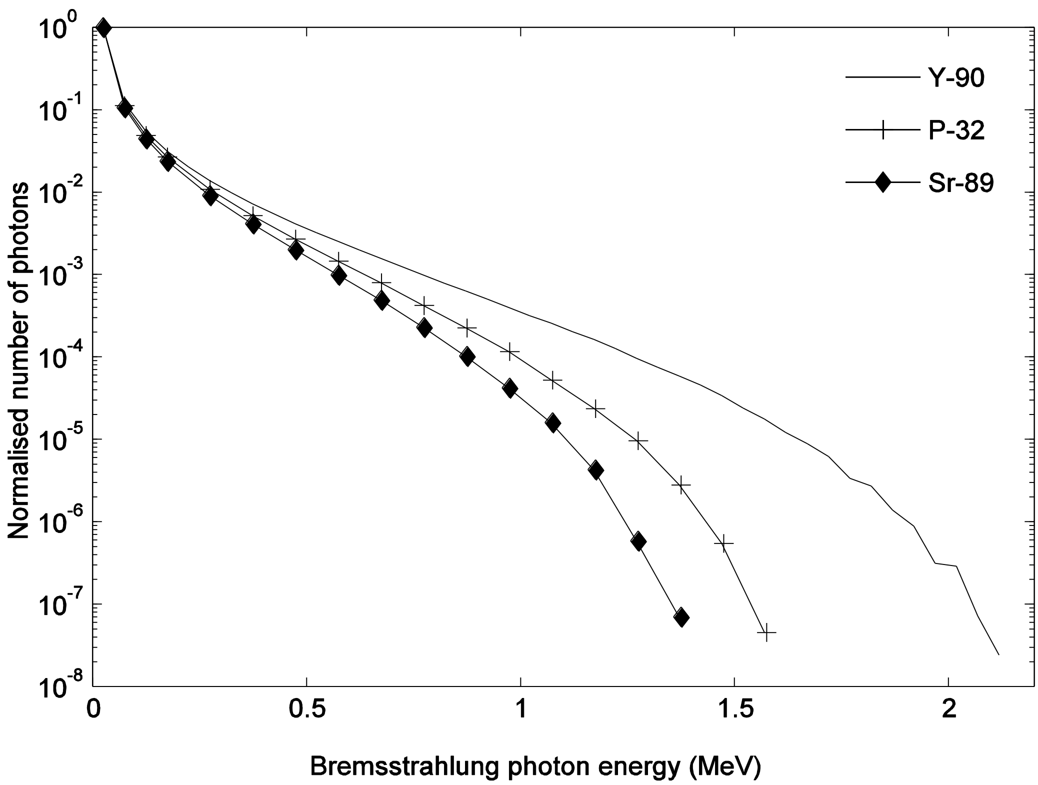


**Figure 4.5: Bremsstrahlung photons energy spectra for $^{90}$Y, $^{32}$P and $^{89}$Sr point sources in water.**

Beta particles have a characteristic range in matter that is dependent upon their initial kinetic energies and the media they traverse. Bremsstrahlung photons can be emitted anywhere along the path of electron, thus the distance between the point of decay and point of bremsstrahlung emission varies. Figure 4.6 and 4.7 show that the bremsstrahlung photons were produced at varying distances along the electron track from the point of beta decay but the probability of photon generation decreased with radial distance. The radial distance to the bremsstrahlung emission depends on the kinetic energy of the incident electrons (Figure 4.6) and the density of the absorbing material (Figure 4.7). Bremsstrahlung photons were emitted as far as 11 mm from the $^{90}Y$ source in water, and 90% of the bremsstrahlung photons were emitted within 5 mm of the source. The maximum photon emission distance for $^{32}P$ and $^{89}Sr$ in water was approximately 8 mm and 7 mm respectively. Figure 4.7 shows that there is an inverse relationship between the radial distance of the $^{90}Y$ bremsstrahlung emission and the density of the absorber material.

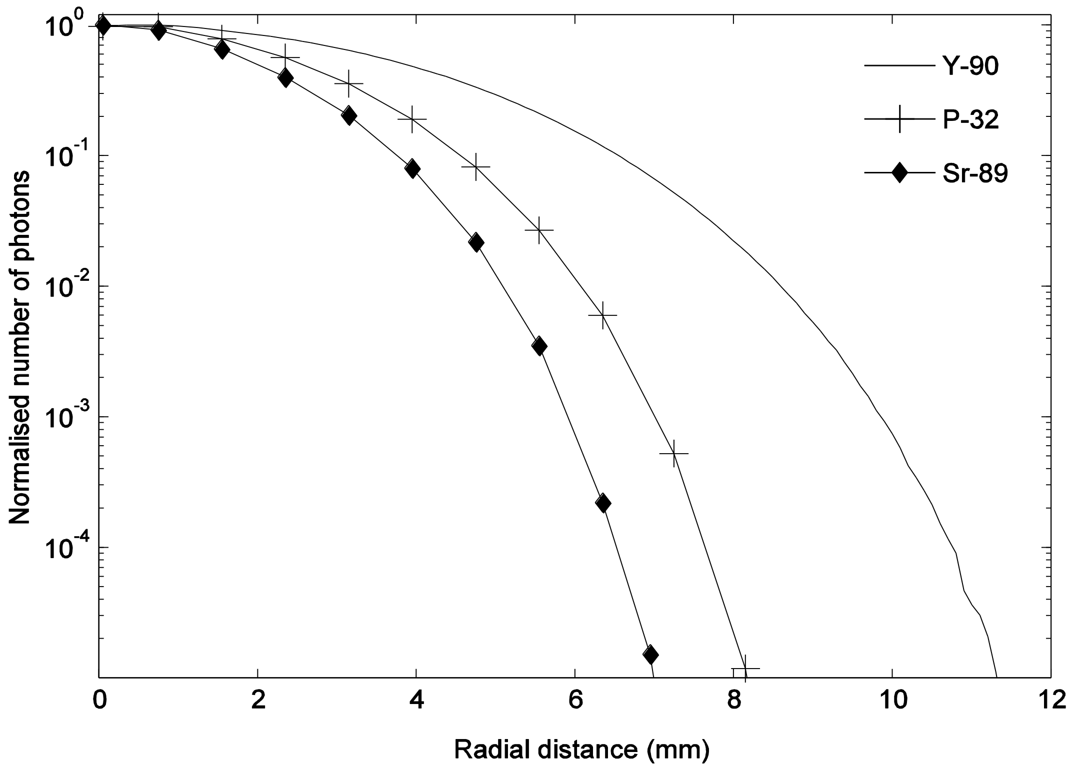


**Figure 4.6: Radial distance distribution of bremsstrahlung photon emission from $^{90}Y$, $^{32}P$ and $^{89}Sr$ point sources in water.**

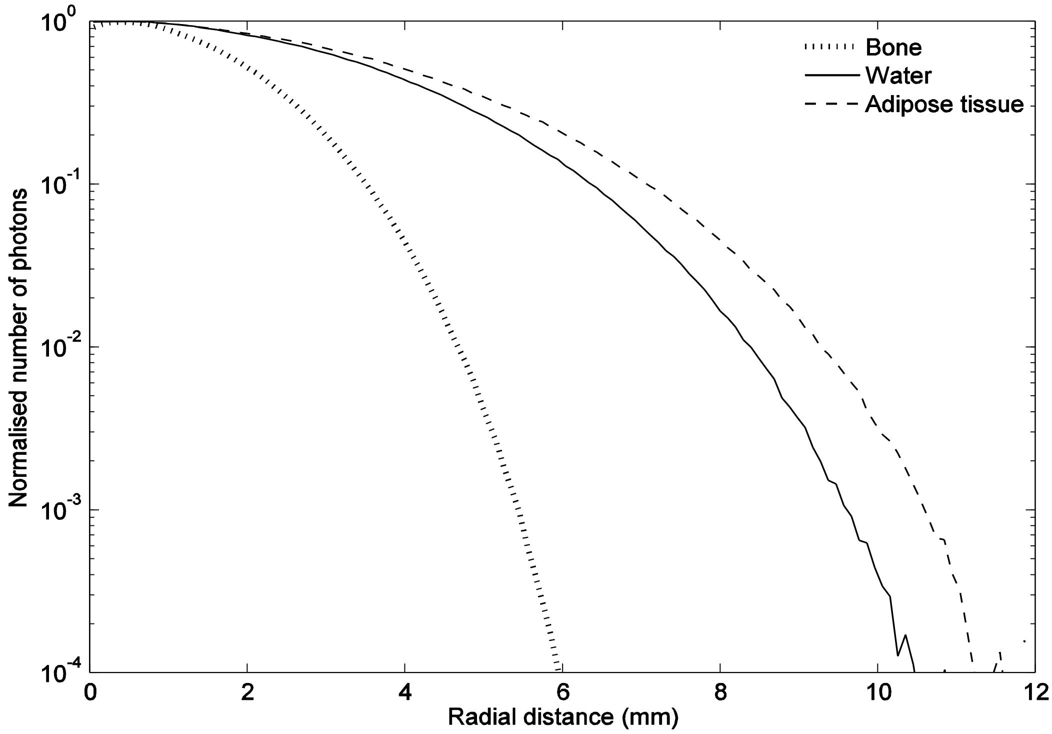


**Figure 4.7: Radial distance distribution of bremsstrahlung photon emissions from a $^{90}Y$ point source in water, bone and tissue.**

Furthermore, the proportion of photons that were emitted at same distance varies with photon energy. This is demonstrated from the $^{90}Y$ simulation in water (Figure 4.8). We can see that photons of the same energy were created at all radial distances out to a maximum with the rate at which they were produced dropping off with distance. The rate of drop off of the higher energy bremsstrahlung was faster for the lower energy photons.

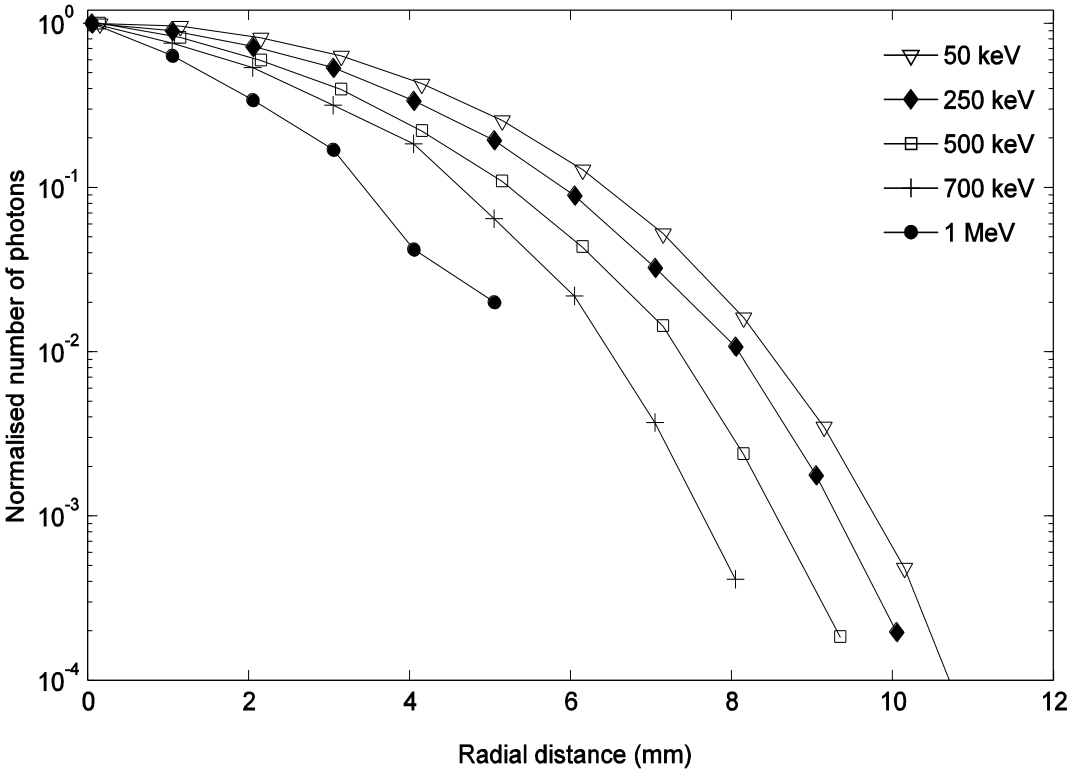


**Figure 4.8: Radial distribution of bremsstrahlung photon emissions from a $^{90}Y$ point source in water at selected photon energies.**

Even though the bremsstrahlung photons generated can be emitted in any direction, the angular distribution of the bremsstrahlung photons depends on their radial distances, energies of the incident electron as well as the absorbing material as shown in Figures 4.9–4.12. Figure 4.9 shows the angular distribution of bremsstrahlung emissions of $^{90}Y$ at different radial distances. It indicates that most bremsstrahlung photons were emitted at smaller emission angles when they were generated closer to the source. The angular distribution becomes broader at larger distances from the source.

Figure 4.10 shows the comparison of angular distributions between different radioisotopes in water. The bremsstrahlung photons were emitted at smaller emission angle in $^{90}Y$ which has higher energy compared to $^{32}P$ and $^{89}Sr$. The angular distribution became wider for radionuclides with lower energies. A closer look on the influence of energies on the angular distribution of the bremsstrahlung photons is illustrated in Figure 4.11. This figure shows the angular distribution of $^{90}Y$ bremsstrahlung photons in the 0 to 300 keV energy range with 50 keV intervals. It indicates that higher energy photons were emitted at smaller emission angles. These figures show that photons emitted closer to the source and with higher energy are more likely to be forwardly directed. The angular distribution of the photons was also dependant on the material. Low effective atomic number material produced distribution with smaller angle width (Figure 4.12).

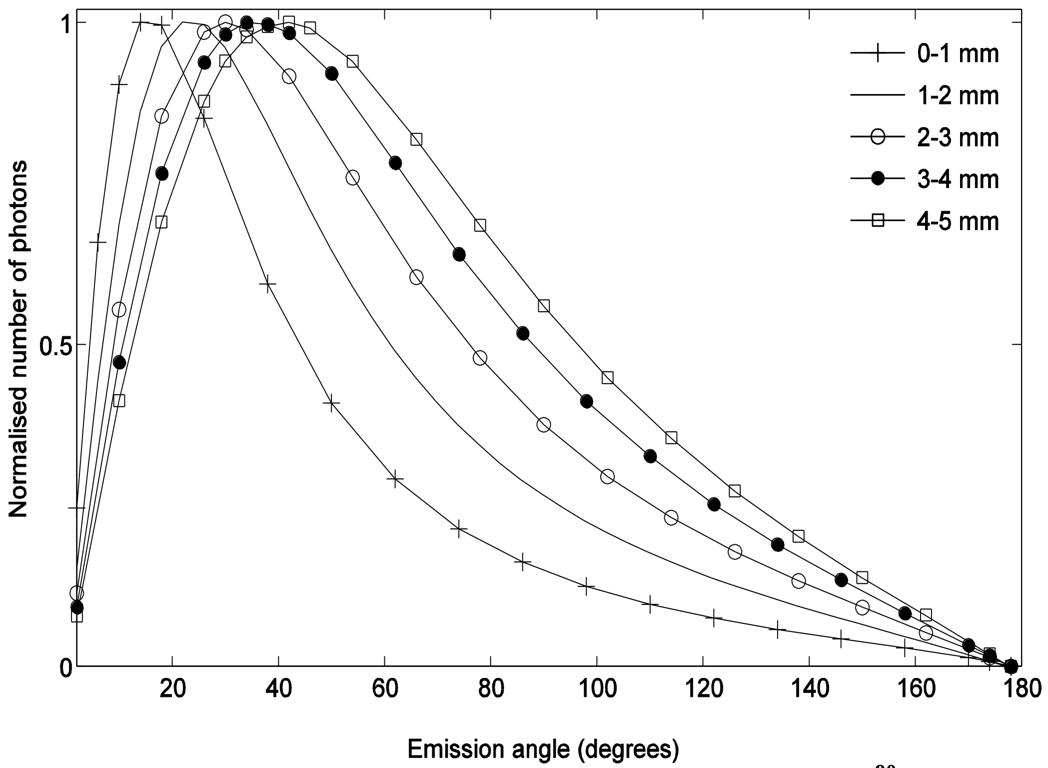


**Figure 4.9: Angular distribution of bremsstrahlung photons from $^{90}$Y decay in water at different emission distances from the source.**

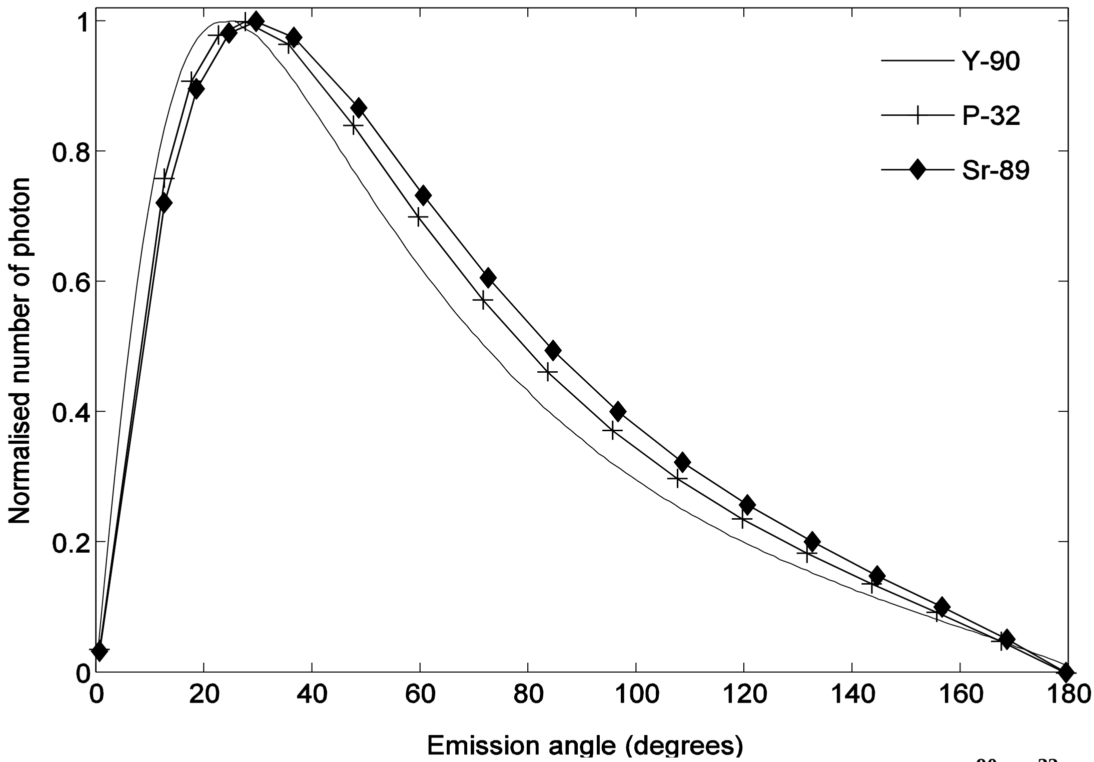


**Figure 4.10: Emission angle distribution of bremsstrahlung photons for $^{90}$Y, $^{32}$P and $^{89}$Sr point sources in water.**

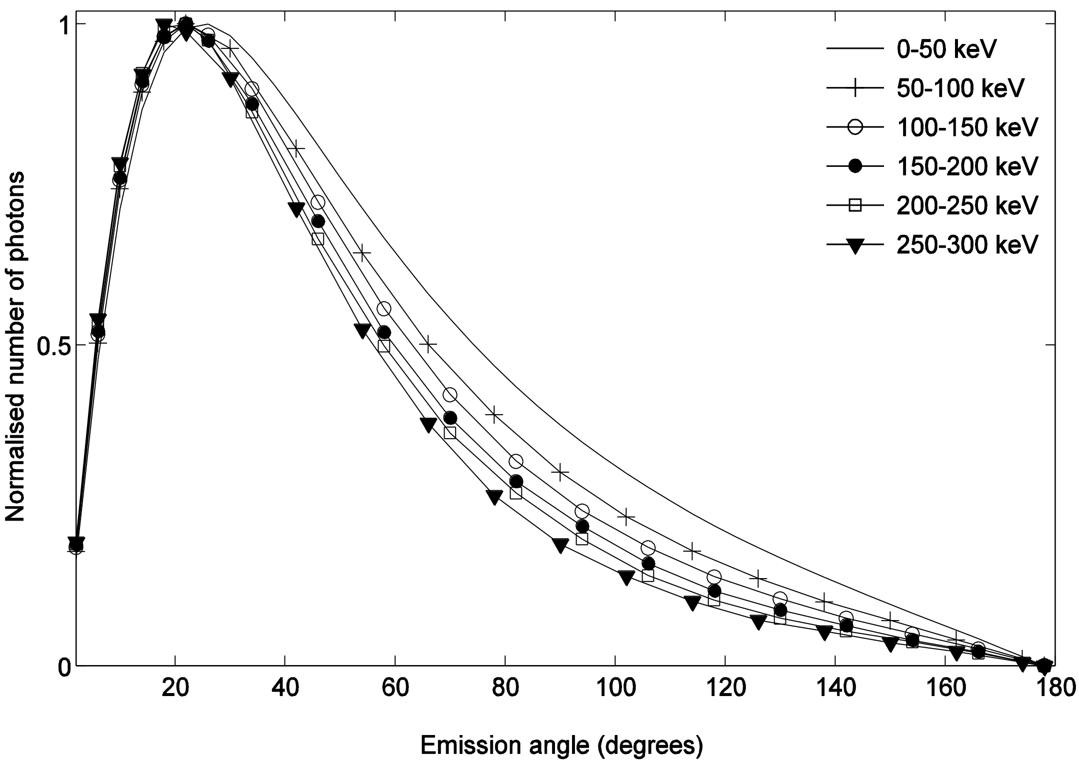


**Figure 4.11: Angular distribution of bremsstrahlung photons from $^{90}Y$ decay in water for selected energies.**

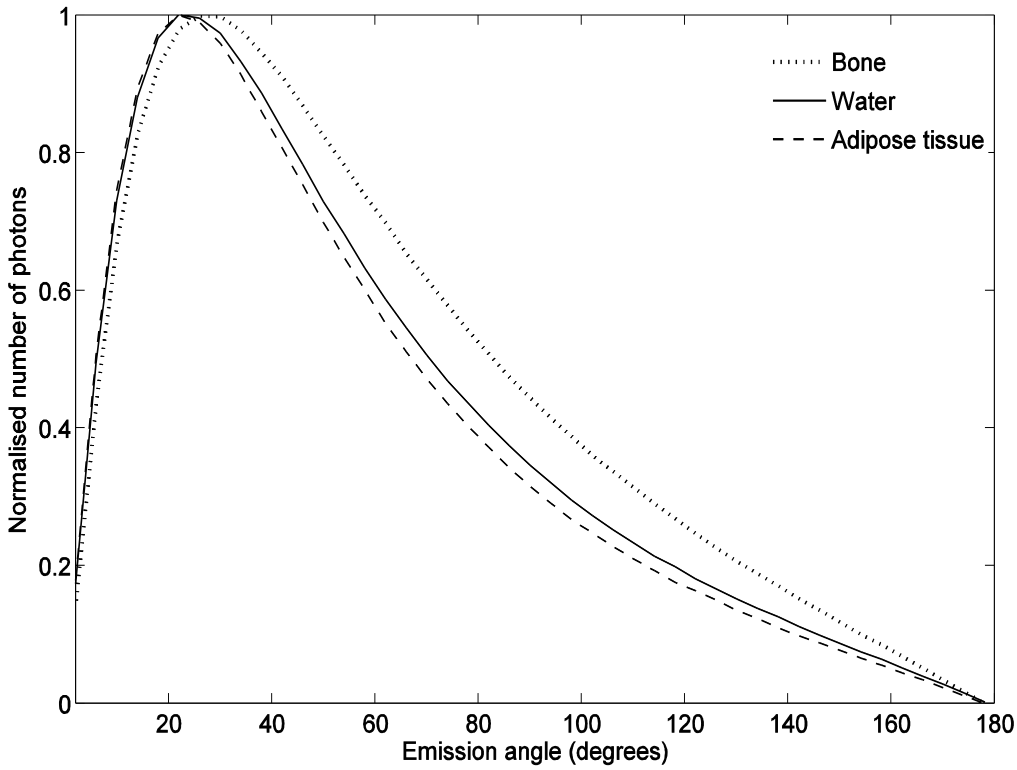


**Figure 4.12: Bremsstrahlung photons emission angles generated in water, bone and tissue for a $^{90}Y$ source.**

## 4.4 Discussion

In order to develop the kernel-based photon source, it is important to obtain the distribution of bremsstrahlung photons produced from beta decay. The energy spectra, radial and angular distribution were simulated for different beta-emitting radionuclide in different materials. Then the energy spectrum and distribution were investigated more closely for $^{90}$Y decay in water.

Beta particles lose energy through ionisation and radiative collisions in which bremsstrahlung are generated. Most electron interactions are via collisional loss thus very few bremsstrahlung photons are produced in this simulation. An electron undergoes many interactions before it loses all its energy thus explains the long simulation time spent for tracking the electron histories. From the results, we can also understand that the sensitivity for bremsstrahlung imaging will be low especially when the source is projected to a collimator.

Radiative loss increases with the energy of the incident electron and the atomic number of the absorber material (Evans, 1955). Results show that bremsstrahlung output was higher for $^{90}$Y decay in bone and least for $^{89}$Sr decay in adipose tissue. As expected, the bremsstrahlung production in materials with low effective atomic number was found to be a low-probability event. For $^{90}$Y decay in water, only 8.6% of the decay generates bremsstrahlung photons. The bremsstrahlung yield of $^{90}$Y in water was comparable to the study of Heard et al. (2004a) where 8% bremsstrahlung photons were produced in their simulation.

Bremsstrahlung photons have a continuous energy spectrum and are produced at varying distances from the point where the electron is emitted. The majority of the bremsstrahlung photons produced has low energy and only 1.9% of the bremsstrahlung photons from $^{90}Y$ decay in water have energies above 50 keV. This compared well with the percentage obtained by Heard et al.(2004a) which is1.85%, but was slightly lower than the percentage attained by Minarik et al. (2008) which is 2.2%. The lower energy photons have little importance in bremsstrahlung imaging as they are absorbed by the patient and the collimator, and are not detected by the gamma camera. Similar to the results presented by Simpkin et al.(1992), our finding shows that the bremsstrahlung photon's energy depends on the radial distance from where it is emitted from the beta point source. The electrons lose energy through minor interactions as they penetrate deeper, so the energy of the bremsstrahlung photons decreases with depth. Low energy photons are produced along the electron's track but high energy photons are produced at radial distances closer to the emission point. Moreover, the probability of photon production decreases with radial distance. This is to be expected as the betas that produce the higher energy bremsstrahlung must produce the photons before their energy drops too low from lower energy interactions along its path. The result also shows that the radial distance of the bremsstrahlung emission was influenced by the absorber material.

An electron may interact and lose its energy anywhere along its track in a medium. This means that bremsstrahlung may also be generated at any position along the track. The energy and the direction of the bremsstrahlung photon which is produced depend on the incident electron's energy and the material it traverses. Since the energy of an electron varies along the track, the energy and the emission angle of the bremsstrahlung photon also vary. Our results show that the width of angular distribution of bremsstrahlung photons is inversely related to radial distances and photon energy. At radial distances closer to the beta emission point, the photons are emitted more towards the forward direction, whereas the angular distribution becomes broader with increased radial distance. This is because at larger radial distances, electrons have undergone more interactions, lost more of their energy and multiple scattering through large angles becomes more important. This directs the electrons further away from the central path before emitting bremsstrahlung photons and contributes to wider angular distribution. The initial momentum of an incident electron is shared between the residual electron, the atomic nucleus and the emitted photon in a radiative collision. This means that the emitted photon only carries a small portion of the momentum and can be emitted in any direction, with higher energy photons tending to be more forward directed (Shivaramu, 1986).

This also explained the angular distribution of the bremsstrahlung photons for different materials. The emission angle of the photons is greatly dependant on the absorbing material. Low effective atomic number material gives distribution with smaller width of angular distribution. Multiple scattering of the electrons in the material makes a large contribution to the angular distribution. In high density materials, an electron undergoes more collisions and loses more energy thus produces a wider emission angle (Nordell & Brahme, 1984). This is shown from $^{90}$Y simulation in bone, where it generates wider angular distribution.

The effect of emission angle could be used to predict the performance of the collimator of the gamma camera. Since high energy photons have smaller emission angles, we expected that they could escape the phantom and be detected by the gamma camera. Low energy photons have wider emission angles, thus might be absorbed by collimator septa and not be detected. We also expected that photon kernels with the correct angular distribution would generate narrower point spread function (PSF) than assuming an isotropic emission.

The validation of bremsstrahlung photon energy spectra with experimental data are mostly done for energy above 2 MeV and in targets used in radiotherapy. It was recognized in these validation studies that the spectra generated by Monte Carlo codes generally overestimated the low-energy fluence of bremsstrahlung photons as demonstrated by Faddegon et al. (2008). This was also shown in our comparison of the measured and simulated bremsstrahlung spectra. This present study used the Geant4 low-energy physics package where the range of validity for electrons and photons extends down to 250 eV, which is relevant for the use in medical physics. Their compatibility with reference data from National Institute of Standards and Technology (NIST) has been well established (Amako et al., 2005). However, this study did not intend to compare the results with experimental measurements. The primary intention was to investigate the characteristics of the bremsstrahlung photons as simulated by Geant4 and used them to develop kernel-based photon source. The overestimation of the simulated low-energy bremsstrahlung photons would be consistent throughout the study.

## 4.5 Summary

Bremsstrahlung photons production from beta decay is investigated. The distributions of the bremsstrahlung photons are aggregated and normalised to obtain the probability distribution functions. It is found that bremsstrahlung production in human tissues is a low-probability event. In order to obtain good statistics, large number of electron histories need to be simulated and this takes a long computation time. The distributions show the relationship between the radial distance, energy and emission angle. At radial distances closer to the beta source emission point, high-energy photons are produced, and the photons are emitted more towards the forward direction. On the contrary, when the radial distance increases, the energy of the photons decreases and angular distribution becomes broader. The bremsstrahlung distributions obtained from this study are used later to define a kernel-based photon source.

# CHAPTER 5

# THE KERNEL-BASED PHOTON SOURCE

## 5.1 Introduction

We established in the previous chapter that the production of bremsstrahlung photons in materials with low atomic number is very low, therefore it is necessary to run many electron histories to obtain good statistics. This implies a very long computation time as the Monte Carlo simulation of electron transport is slow due to the their frequent interactions. It is therefore beneficial to find a way to achieve an acceptable computing time by reducing the time spent on tracking the electrons.

Compared to electron transport, tracking of photons is relatively a fast process. Therefore this study proposes that a bremsstrahlung-producing $^{90}Y$ beta-emitting point source is replaced by a kernel-based photon source. The kernel-based photon source was defined as an array of concentric spherical photon-emitting shells sources that corresponds to the emitters. This chapter describes the development of a kernel-based photon source based on the probability distribution functions of the bremsstrahlung photons production obtained in the previous chapter.

## 5.2 Method

This study focuses on the development of a kernel-based photon source for $^{90}Y$ bremsstrahlung produced in water. This is because all soft tissues have physical characteristics similar to water. The probability distribution functions that were used in this simulation were obtained from the full Monte Carlo simulation of $^{90}Y$ point source in water phantom which provided the information on the bremsstrahlung yield, energy spectra, radial and angular distributions of the bremsstrahlung photons in water.

The kernel-based photon source was defined as an array of concentric spherical shells of photon sources. A point source which was modelled as a kernel-based photon source was placed at the centre of a 3 cm radius spherical volume of water (Figure 5.1). Each spherical shell corresponds to a spherical region of finite thickness from which some of the initial bremsstrahlung photons were produced around an isotropic $^{90}Y$ point source. The positions on the shells from which the photons were simulated to be emitted were randomly but uniformly spread over the spherical surface. The bremsstrahlung yield was very low in water and for $^{90}Y$ decays, only 8.6% of the decay produced in bremsstrahlung events. Thus *n* beta decays of $^{90}Y$ may be simulated by $n \times 0.086$ photon histories in the kernel-based photon source simulation.

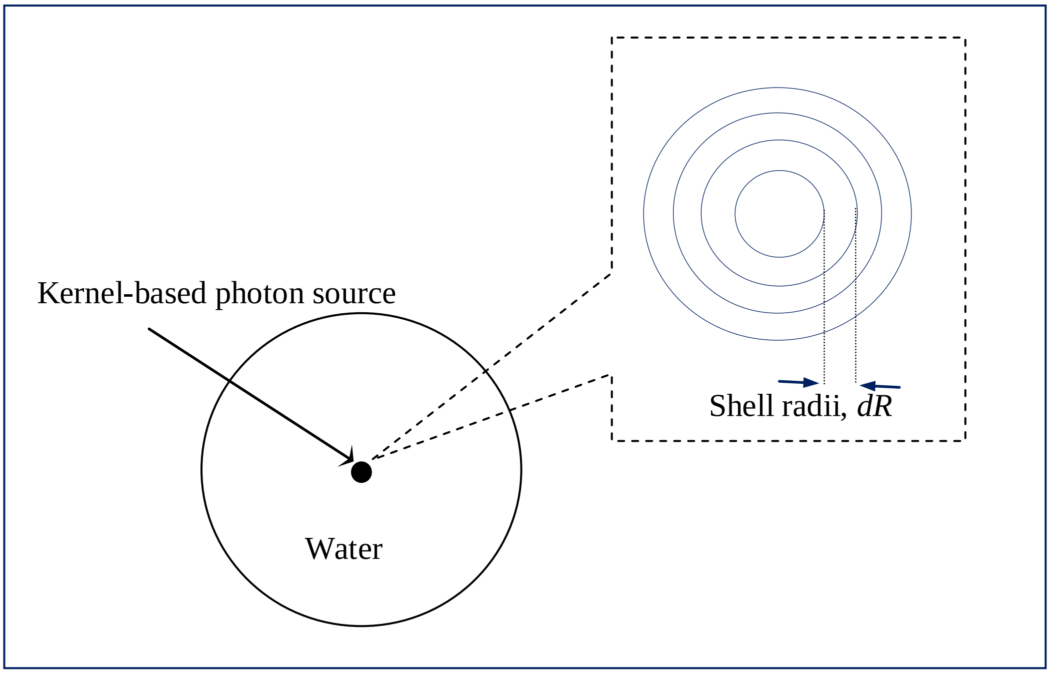


**Figure 5.1: An array of spherical shells defines kernel-based photon source. Each shell corresponds to the spherical region of finite thickness from which some of the bremsstrahlung photons are emitted. Photons were uniformly distributed over the shell. The energy and emission angle of these photons are defined for each spherical shell. Different shell radii, *dR* are used to define the kernel-based photon source.**

The photons emitted by the kernel-based photon source were generated using G4GeneralParticleSource (GPS). GPS provides options to specify the emission position, energy and the angular distributions of the source photons. GPS offers many options to generate the photons. The emission position distribution can be defined using several basic shapes that contain the starting point of source particles. It can be described as point, planar, surface or volume source. The angular distribution defines the directions in which the photons are emitted and the energy distribution defines the energies of the photons. Generally there are three main choices of angular distribution: isotropic, cosine-law or user-defined histogram. The input energy can be set either using built-in functions (e.g. monoenergetic, linear, exponential) or by being defined as a histogram.

Since the kernel-based photon source was defined as an array of concentric spherical shells of photon sources in this work, the position distribution of the photon was defined as a spherical surface. The positions on the shells from which the photons were simulated to be emitted were randomly but uniformly spread over the spherical surface. The energy spectra and angular distributions of the emitted photons were defined for each spherical shell surface. The distributions are defined as histograms. These histograms were based on the calculation of the probability distribution function obtained from the earlier simulation of the beta decay and its subsequent bremsstrahlung emission. The kernel-based photon source can be considered as the sum of the contributions from the series of spherical shell photon sources that account for the radial position, energy and emission angle distribution.

The bremsstrahlung photons distributions generated from the kernels with different shell radii increments, namely 0.1 mm, 0.5 mm and 1.0 mm, were investigated and compared with those from the full Monte Carlo simulation of $^{90}Y$ point source.

## 5.3 Results

The kernel-based photon source was constructed as a series of infinitely thin concentric spherical shells. The photons were emitted from the surface with angle and energy distributions equal to photon distributions at a distance equal to the radius of the shell provided from the simulation of a point $^{90}Y$ source.

It is valuable to know how many shells the kernel should have to reasonably simulate the photon emissions from a point source before the shell approximation starts to become inappropriate. Kernels were constructed with different shell radii increments, namely 0.1 mm, 0.5 mm and 1.0 mm. The overall spectra and angular distributions obtained from the kernel simulations were compared with those from the full beta simulation (labelled as ‘bremsstrahlung photon PDF’).

The angular distribution of bremsstrahlung photons produced from the beta simulation and kernel-based photon source simulations for different shell radii are illustrated in Figure 5.2. It can be seen that the shell thickness used to construct the kernel-based photon source model had a pronounced effect on the photon kernel’s ability to accurately model the bremsstrahlung distribution. The photon kernels with small incremental shell radii (0.1 mm) simulated the bremsstrahlung photon produced from $^{90}Y$ decay almost exactly whereas at larger shell thickness increments (0.5 mm and 1.0 mm) the simulation was rather less accurate.

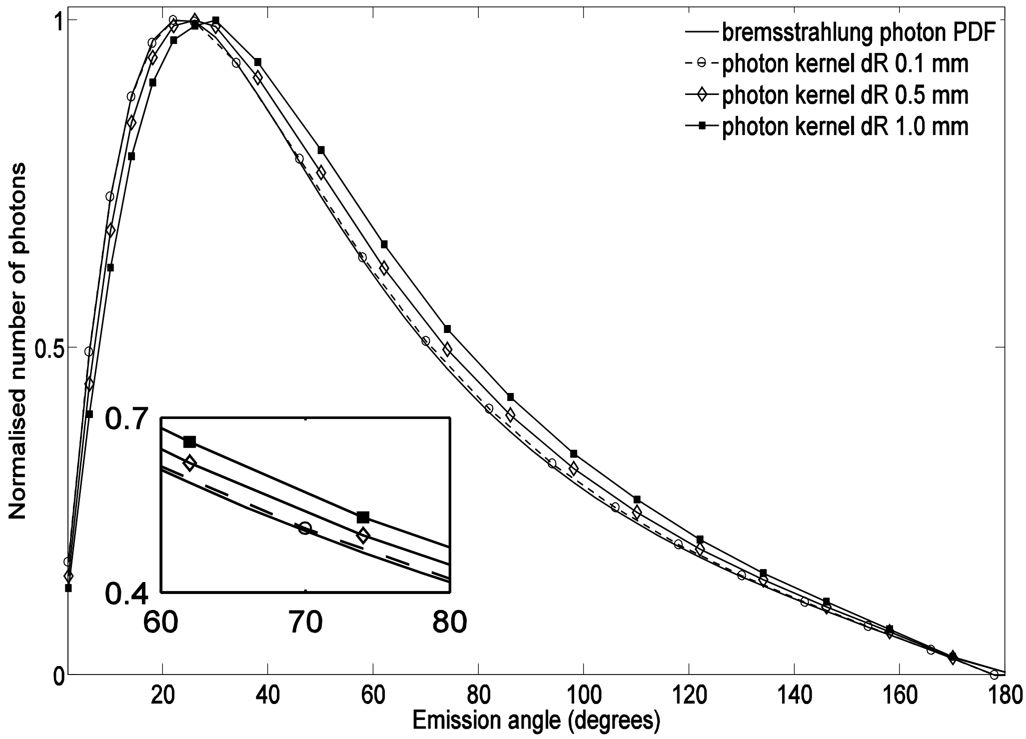


**Figure 5.2: Comparison of angular distribution of bremsstrahlung photons from full $^{90}$Y simulation and kernel-based photon source with various shell thickness. The smaller diagram shows an enlarged section for better comparison.**

As reported in the previous chapter, the energy and the number of photons emitted decrease with the radial distance of emission from the source. Therefore, it may not be necessary to have such small radius differences between the outer shells. This was tested by considering the photon emissions from fewer radii. Figure 5.3(a) shows the combined angular distributions for shells in the range of 0–1 mm for different incremental radii as well as the equivalent distribution from the original beta simulation. Again it is seen that the kernel is very accurate for small incremental radii. Figure 5.3(b) shows the equivalent situation for the

3–4 mm range. There is reasonable agreement now even for an increment of 0.5 mm.

Figure 5.4 shows the comparison between energy spectra from the original beta simulation and photon kernel for shells with different incremental radii in the range of 0–1 mm and 3–4 mm range for bremsstrahlung energies up to 500 keV which is the maximum energy in gamma camera imaging. It also shows a reasonable agreement for radii increment of 0.5 mm.

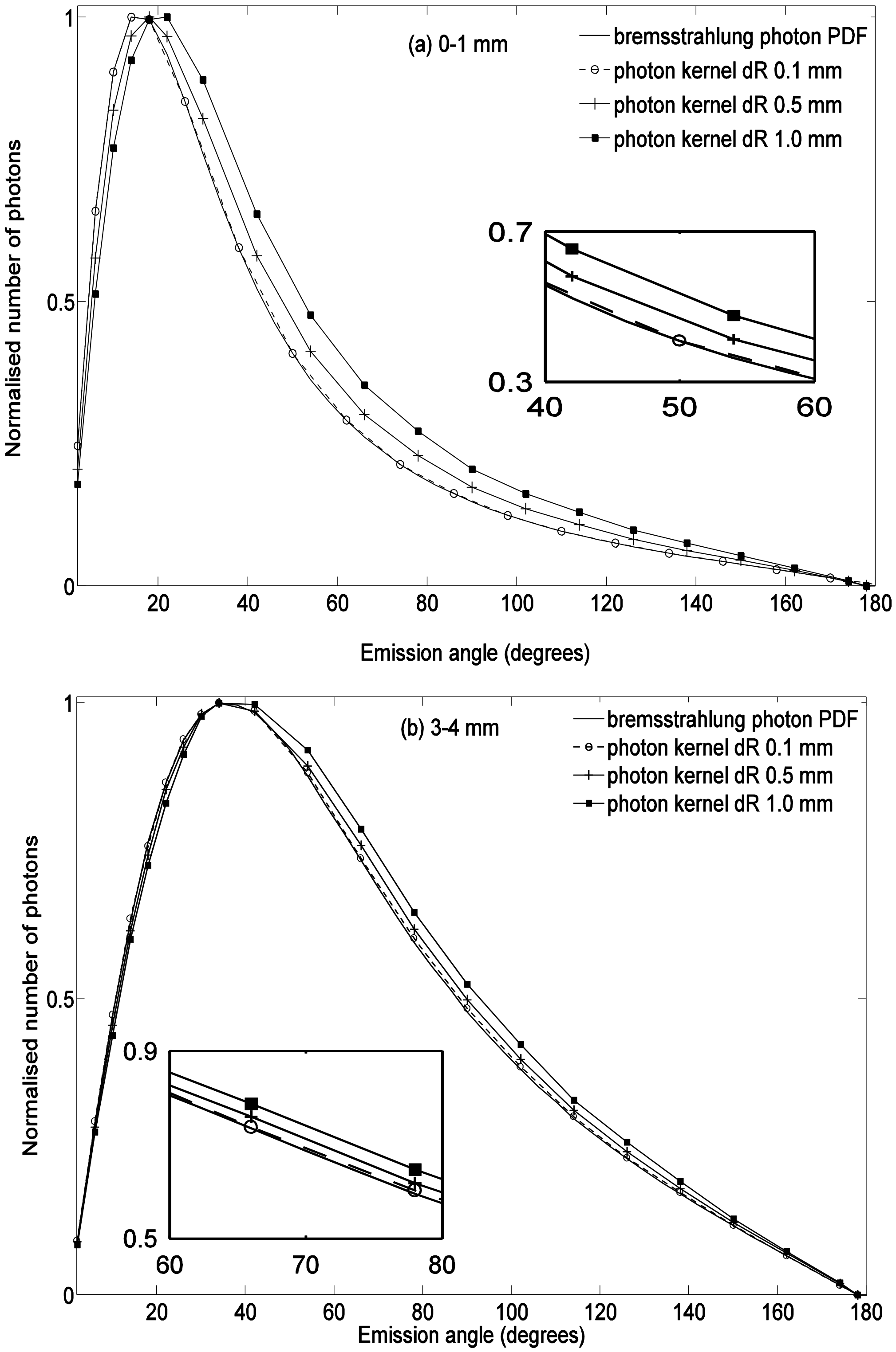


**Figure 5.3: Comparison of angular distribution with different shell thicknesses of photon kernel at different radial distances: (a) Thick shell thickness did not fit the bremsstrahlung PDF at small radii (0−1mm), but (b) matched the data adequately for larger radii (3–4mm). The smaller diagrams show an enlarged section for better comparison.**

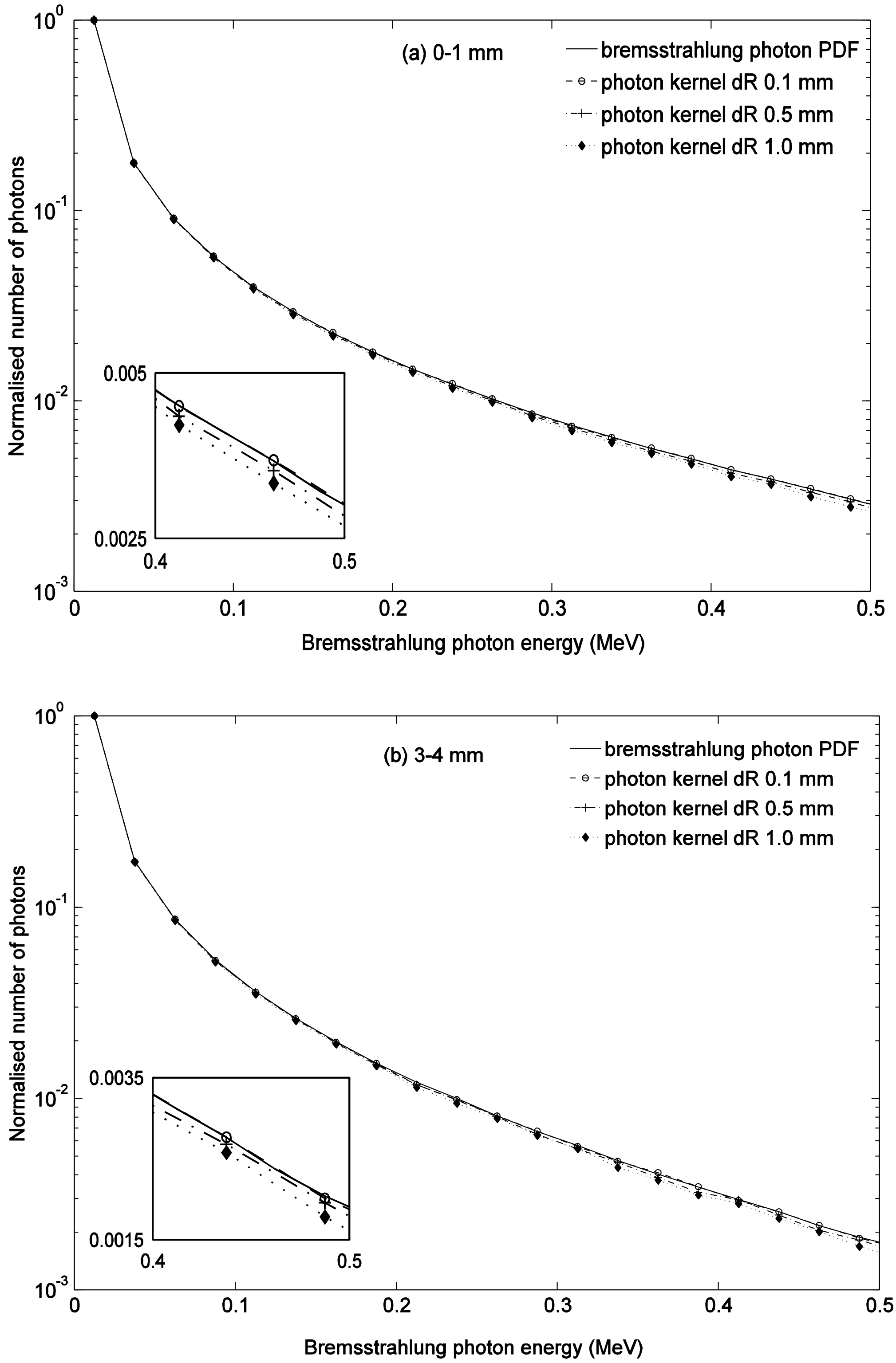


**Figure 5.4: Comparison of energy spectra at different radial distances obtained from photon kernel with different shell thicknesses: (a) 0–1 mm and (b) 3–4 mm. The smaller diagrams show an enlarged section for better comparison.**

Clearly, the kernel-based photon source can be modelled with different radius increments. The use of smaller increments is necessary for the region closer to the beta source, and larger increments are sufficient for regions further from the source. Accordingly, the final kernel-based photon source was modelled such that for radii between 0 mm to 5 mm, increments of 0.1 mm were used, increasing to 0.5 mm for radii of 5 mm to 7 mm and to 1 mm beyond that. Figures 5.5(a) and (b) show the comparison of energy spectra and angular distributions between bremsstrahlung photons produced from the full Monte Carlo beta simulation and from the kernel-based photon source simulation. They are very similar.

The results demonstrate that the bremsstrahlung photon distribution obtained from a kernel-based photon source was a very close approximation to the distribution obtained from $^{90}Y$ beta decay and therefore can be used to replace the $^{90}Y$ beta point source. The simulation time for the kernel-based photon source was 300 minutes, thus the simulation time has improved 27 times from full Monte Carlo simulation of $^{90}Y$ point source for the same number of bremsstrahlung produced from $^{90}Y$ beta decay.

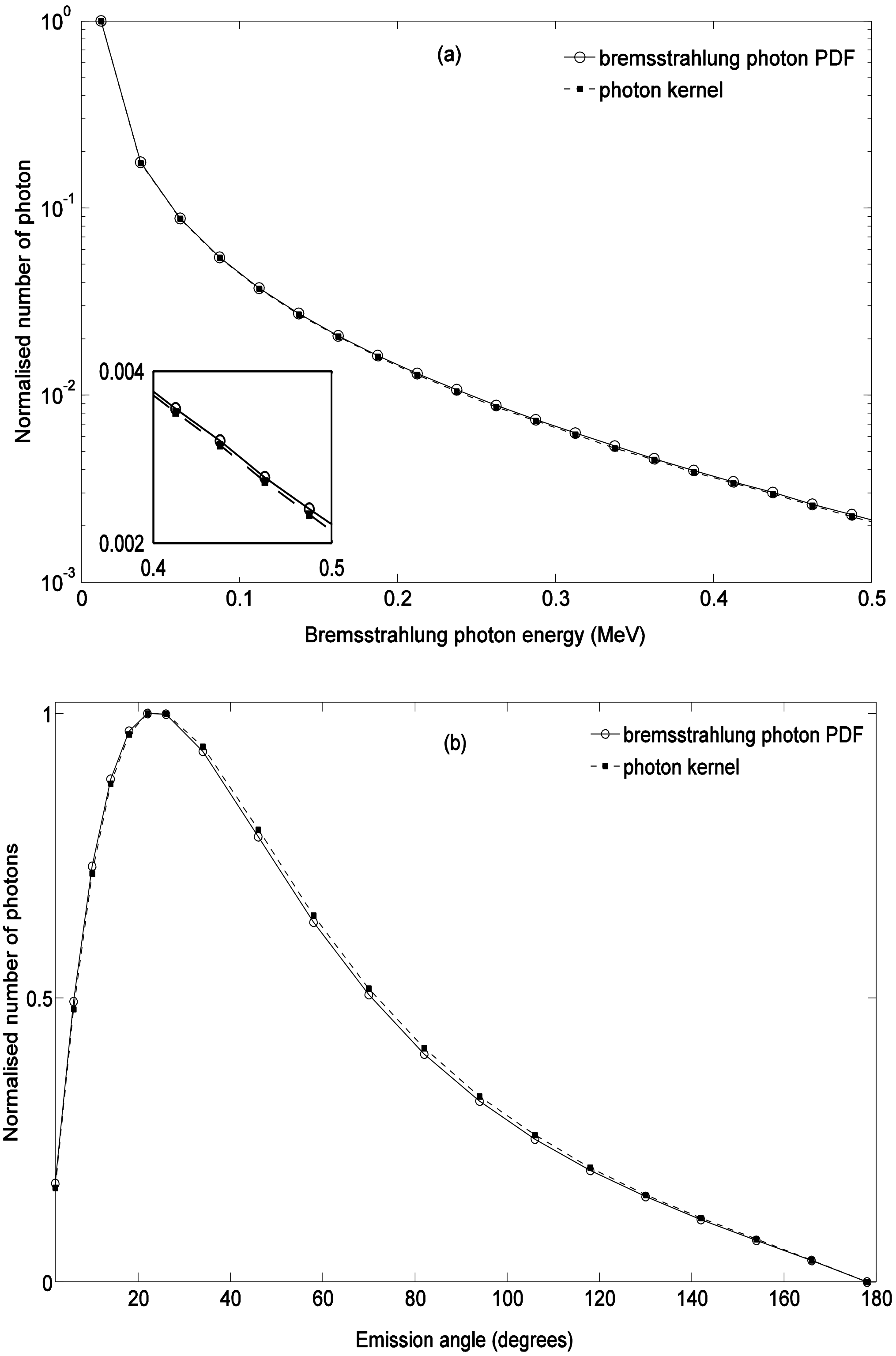


**Figure 5.5: Comparison between bremsstrahlung photon produced from beta simulation and kernel-based photon source for the (a) energy spectrum and (b) angular distribution.**

## 5.4 Discussion

Monte Carlo simulation of bremsstrahlung photons by $^{90}Y$ beta decay is slow due to low bremsstrahlung production and slow simulation of the electron transport processes. To reduce the simulation time, this study proposes that bremsstrahlung photons produced from beta decays of a point source are replaced with a kernel-based photon source. The kernel-based photon source is an array of concentric spherical shells of photon sources that corresponds to bremsstrahlung photon emissions. This approach reduces the problem associated with simulation time in bremsstrahlung imaging studies.

The kernel-based photon source was developed as a series of spherical shells with different radii that model the radial position of where bremsstrahlung photons were generated inside the water phantom. For each radial shell, the energy spectrum and the angular distribution of the kernel-based photon source were defined using the probability distribution obtained from the $^{90}Y$ beta decay simulation data. The accuracy and simulation time of the kernel-based photon source simulation was then compared to bremsstrahlung photons produced from $^{90}Y$ beta decay simulation. The results demonstrated that the kernel-based photon source can be used to replace $^{90}Y$ point source simulation. The use of kernel-based photon source increased the simulation speed and would be used in the subsequent simulation work to investigate bremsstrahlung imaging for radionuclide therapy using gamma cameras.

Although the kernel-based photon source was developed as a function of spheres with different radii, it was based on the energy spectrum, emission angle and radial distance of the bremsstrahlung photons obtained from full Monte Carlo simulation of $^{90}$Y. This means that it takes into account all the important parameters related to bremsstrahlung generation including the beta and bremsstrahlung energy as simulated by Geant4. This approach is used in our simulation because of the dependence of energy and angular distribution on the radial position as demonstrated by bremsstrahlung distributions from beta decay. Although different shell thicknesses are used to construct the kernel, it still can represent the bremsstrahlung photons generated from beta decay adequately. Relatively fewer photons are produced at greater distances from the source. Therefore increasing the shell spacing is reasonable so that the number of photons emitted from each shell does not decrease significantly.

The use of photons as a substitute for the beta source has been studied previously by Heard et al.(2004b) and Rault et al.(2010). However, their work did not consider the emission angle of the bremsstrahlung photons and modelled the photon emission as isotropic. The bremsstrahlung photon distribution is complex. It has a continuous energy spectrum, and the bremsstrahlung photons are produced at varying distances from the point where the electrons are emitted. The emission angle distribution is also not isotropic. The kernel-based photon source defined in this work accounts for the position, energy and anisotropic angular distribution of the bremsstrahlung photons.

$^{90}$Y also decays to an excited state of $^{90}$Zr and achieves its ground state by emitting a 1.76 MeV photon along with positrons with maximum energy of 800 keV (Johnson, et al., 1955). This in turn may create two 511 keV photons from annihilation of the emitted positron with electron. Rault et al.(2010) included the reported emission of the gamma photons and positron in their simulation.

Nonetheless, this is not considered in our simulation as their contribution is low where the relative intensity is $2.2\times10^{-4}$ for the gamma emission and $5\times10^{-5}$ for internal pair production from the total beta decay (Ryde, et al., 1961).

While an analysis of a $^{90}Y$ point source was presented, in a practical situation distributed continuous sources will need to be modelled. For these situations the source can be modelled as an array of closely-spaced point sources. The point source to point source separation will need to be of the same magnitude as the smaller inter-shell separation if it is desirable to include the effects studied in this work.

Although this study focused on the bremsstrahlung production by $^{90}Y$ decay inside water, this method can also be applied for other beta-emitting radionuclides and body tissues like bone which are relevant to bremsstrahlung imaging studies. Studies show that the distribution of bremsstrahlung photons production depends on the radionuclide and the material of the absorber. Therefore changes in the photon production, the energy spectra and emission angle are expected. However, these changes are not characterised in this thesis. Of further interest is how the kernel will change when a point source is positioned close to the boundary between two tissues of considerable density differences. Possibly it may be found that it may be straightforward matter to distort the kernel appropriately to account for this situation. If not, then full electron transport simulation may be necessary.

## 5.5 Summary

The kernel-based photon source is a surrogate for a beta point source for faster Monte Carlo simulation. The kernel-based photon source was defined using the characteristics of bremsstrahlung photons produced from $^{90}Y$ decay described in the previous chapter. The kernel-based photon source has been generated and compared to the initial bremsstrahlung production obtained from beta simulation. The results showed that the kernel-based photon source could be used to replace beta point source and greatly improve simulation time.

# CHAPTER 6

# ESTIMATION OF POINT SPREAD FUNCTION AND EVALUATION OF KERNEL-BASED PHOTON SOURCE

## 6.1 Introduction

It is valuable to assess how well the kernel-based photon source represents a point beta source when an image of it is "seen" by a gamma camera. Such assessments are described in this chapter. The simulation work is divided into three parts. First, it describes a method that assumes the point spread function to be adequately represented by a two-dimensional Gaussian function. Estimates of the standard deviation, $\sigma$, of the Gaussian function are obtained and used to calculate the FWHM of the point source's image. Then, the collimator model and the estimation method are validated by comparing the simulation data with experimental data. Finally, the accuracy and speed of the kernel-based photon source are evaluated.

## 6.2 Estimation of point spread function

When a point source is imaged, ideally the image will also appear as a point. However in practice the image is not a point but is better described as a blob spread around the position of the source. The spreading of the image of a point source is often described mathematically by a point spread function (PSF).

The performance of a gamma camera system can be evaluated by observing the point spread function.

A modelling of a point spread function can be achieved by fitting the detected photons distribution to a known function. Here it is assumed that the point spread function of the source image is a Gaussian function (Figure 6.1) that has been modulated by the effects of the collimator holes (although the modulation effect is not shown in Figure 6.1). The Gaussian part of the point spread function is of the form

$$f(x,y) = \frac{1}{2\pi\sigma^2} e^{-\frac{(x^2+y^2)}{2\sigma^2}} \qquad (6.1)$$

where $x$ and $y$ are the distances from the point source's position and $\sigma$ is the 'standard deviation'. In order to quantify the spatial resolution, the FWHM of the point spread function can be calculated by

$$FWHM = 2\sigma\sqrt{2\ln 2} \qquad (6.2)$$

The width of the Gaussian curve depends on $\sigma$, which measures the spreading of the function. A low $\sigma$ indicates that there is little spreading and therefore that the FWHM is small and the resolution is high.

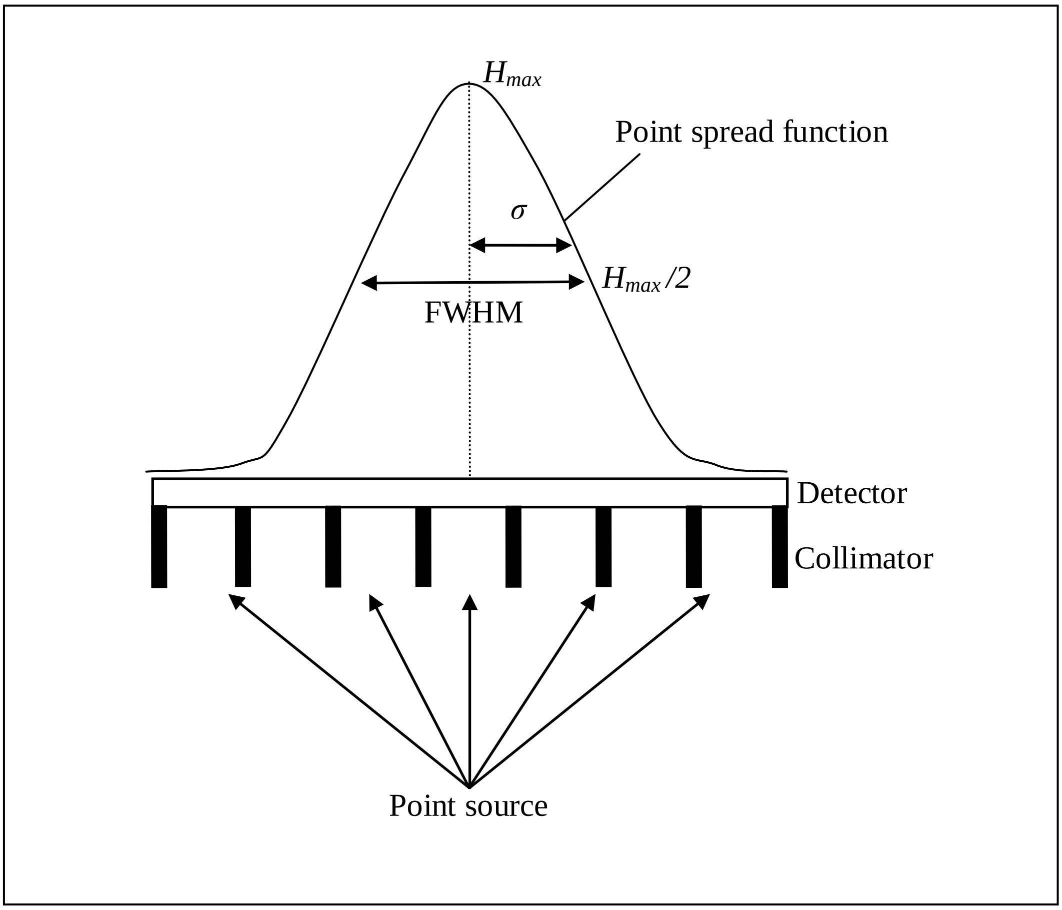


**Figure 6.1: Point spread function.**

The Gaussian function in the form that is given in (6.1) is a two-dimensional function that has been normalised so that the volume under a curve represented by that function is unity.

A simplified gamma camera model, which consists of a collimator and NaI(Tl) detector only, was simulated as shown in Figure 6.2 below. It would be expected to have a NaI(Tl) crystal behind the collimator. It was decided to model the top of the collimator holes as being filled with NaI(Tl) so that the photons entering a hole and being detected can be totally separated from those in an adjacent hole. This lends itself to the analysis that is described later.

Two types of collimator were simulated. The first is one with square holes. This is not a usual collimator that is used in nuclear medicine, but was used in the initial stages of developing the work described in this chapter as the geometry is very simple. The second type is the usual hexagonal-hole type. The top views of the collimators are shown in Figure 6.3 which illustrates the septal thickness, *s* and the hole diameter, *d* for square- and hexagonal-hole collimators.

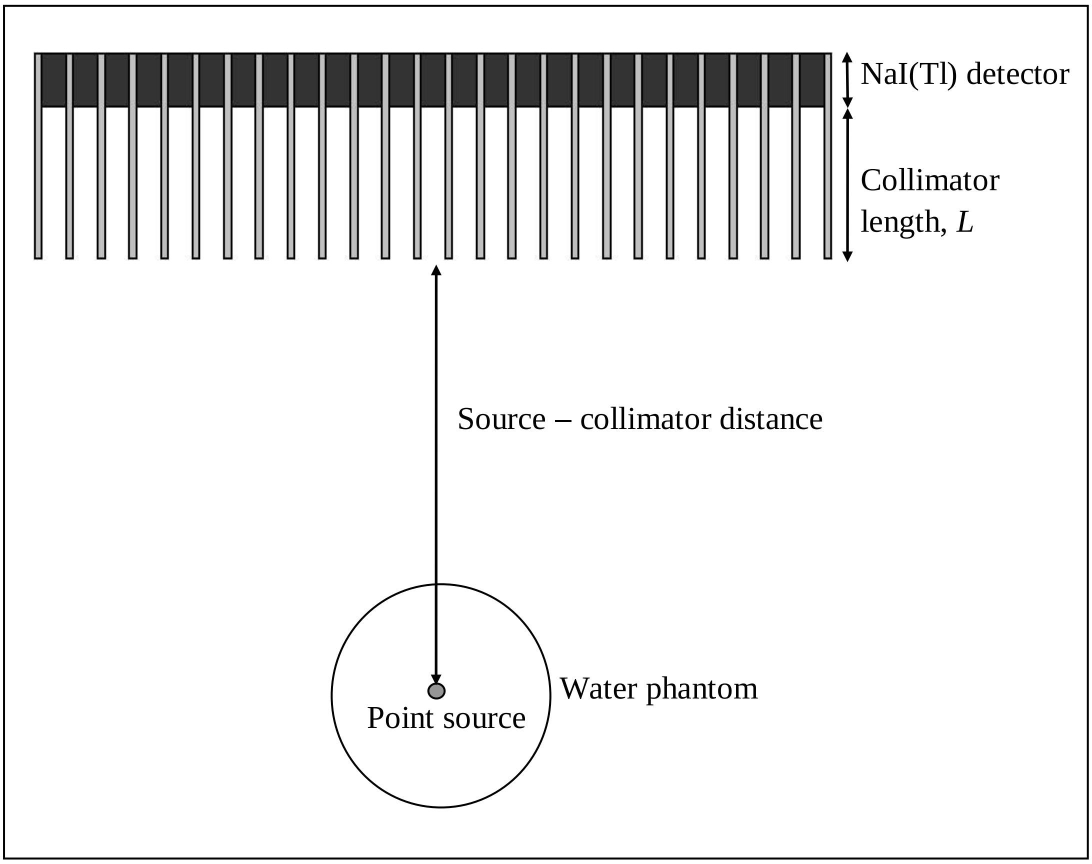


**Figure 6.2: Collimator simulation set-up.**

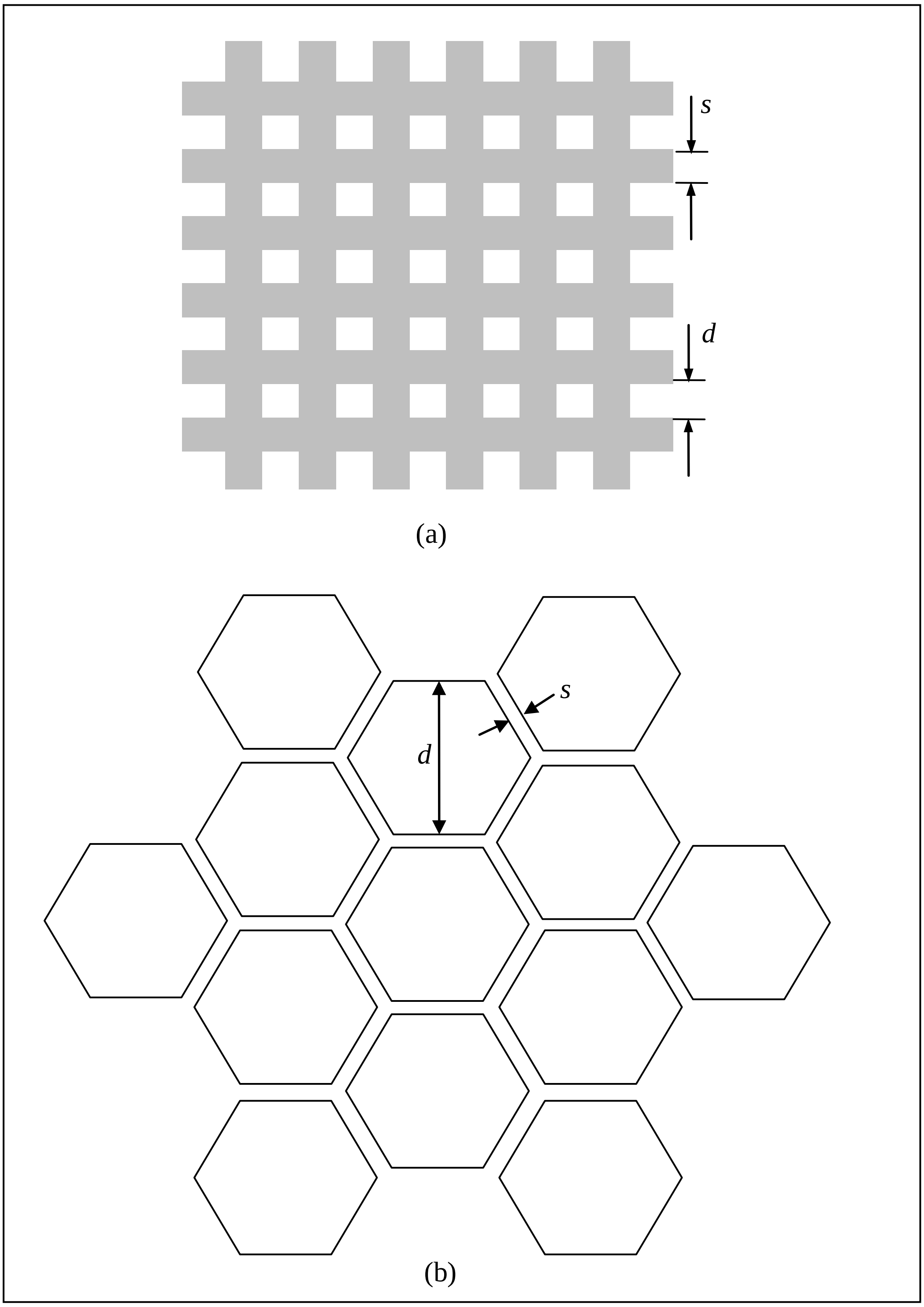


**Figure 6.3: Top view of (a) square-hole and (b) hexagonal-hole collimators.**

Determining the FWHM of the image of a point source formed by the collimator is not straightforward. If a NaI(Tl) detector is placed behind a collimator, it would detect the point source as a series of square or hexagonal projections through the collimator (based on the collimator hole shape) rather than as a continuous function. As the FWHM of the point spread function is of similar dimension to the collimator holes, the FWHM would be hard to estimate from such an image. Therefore the following method was used to calculate the FWHM.

It is assumed that all of the photons that approach the collimator are travelling perpendicular to the collimator. This is obviously not true for all the photons from a point source, but it will be a very close approximation to those that are emitted directly towards the collimator. These are the ones that are most likely to be detected. Those that approach the collimator at greater angles are less likely to be detected.

As a point source emits photons, some of these will travel through each hole and be detected. If the number of photons detected in each hole is recorded, then knowing these numbers, the positions of each hole and the mathematical function that describes the point spread function, it is simply a mathematical fitting process to estimate the parameters of the function. In the case of the function that is used here, the Gaussian function, we estimate the $\sigma$ and from that, the FWHM can be obtained.

In theory, it is possible to estimate the $\sigma$ by considering the number of detected photons that appear in just one hole compared to the total number detected. This is likely to give "noisy" estimate due to low statistics, especially when the hole is somewhat distant from the centre to the function. Therefore it is preferable to consider the number of photons detected in a number of holes to increase the statistics.

Ideally, it would be good to develop an expression that will describe the volume of square or hexagonal region under a two-dimensional Gaussian function that describes a point spread function. This would make the sort of analysis described above very straight forwards. At first sight this appears to be simple mathematical problem. However, the volume under a two-dimensional Gaussian function requires a double circular integral with rather awkward limits to be solved. Therefore a numerical approach was used instead.

The Gaussian function was evaluated on a square grid of points under a single quadrant of the Gaussian function at $0.01\sigma$ increments up to $5\sigma$ in the $x$ and $y$ dimensions (Figure 6.4). The $5\sigma$ limit was chosen as beyond that limit the Gaussian function is extremely small. The values of the function at the points were stored. It is, of course, not necessary to store the values for all quadrants as the Gaussian function is symmetrical.

The problem is then to compute the volume of a region under the function that is bound by an arbitrary shape in the $x$-$y$ plane. This is quite straight forwards as the surface can be considered to be a mesh with the surface approximated by many surface elements. The total volume is summed from the individual volumes below each surface element.

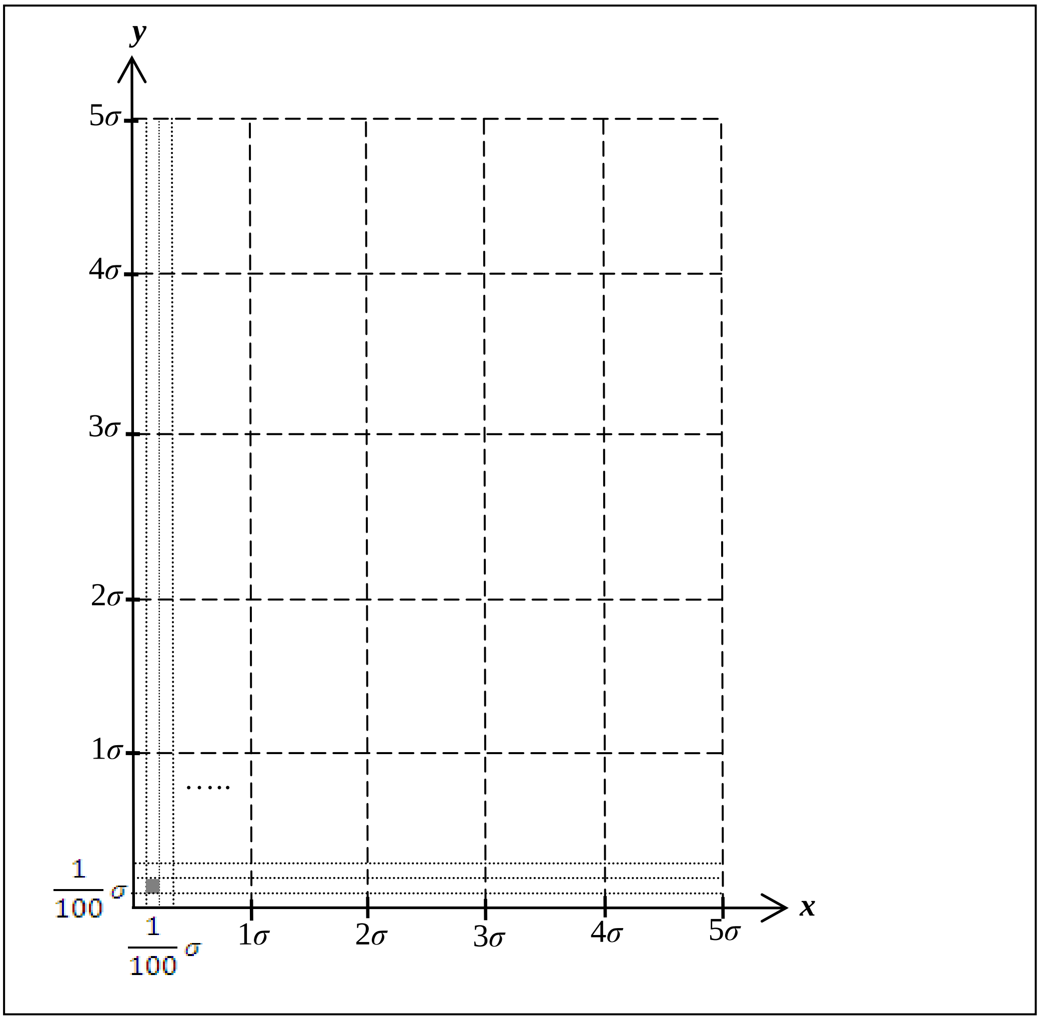


**Figure 6.4: Dividing the x-y plane into small squares. The values of the Gaussian function at each corner are stored.**

## 6.3 Initial studies with the square-hole collimator

### 6.3.1 Method

The estimation method was first implemented for the square-hole collimator arrangement as the geometry is very simple and the computations are very straight forward.

The square-hole collimator was initially simulated so that the source was directly in front of one of the holes. The number of photons entering the collimator hole directly above the source and the surrounding holes were recorded (Figure 6.5 (a)) and the value of $\sigma$ was estimated. The simulation was then performed with the source shifted so that the source was under a septum as in Figures 6.5(b) and (c) and the corresponding $\sigma$ values estimated to give further estimates. The estimates of $\sigma$, were then used to calculate the FWHM using equation in (6.2).

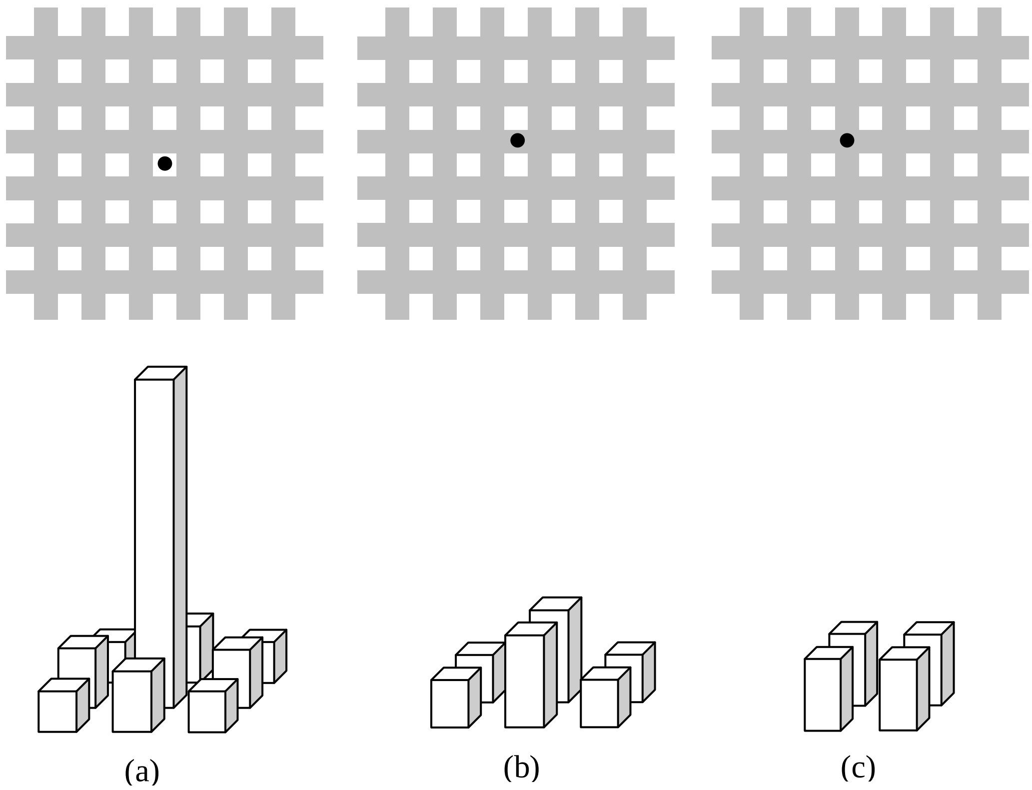


**Figure 6.5: Numbers of photons detected in the holes around point source for square-hole collimator.**

The same method was applied for hexagonal-hole collimator to estimate the $\sigma$. For this collimator, the source was modelled as being placed at the centre and directly in front of one of the holes. An estimate of $\sigma$ was made first just using the photon counts detected in the centre hole, then another for the next six out from the centre, then another for the next six out etc, to get series of (increasing noisy) estimates. Shifting of the source to other positions in front of the collimator was not done for hexagonal-hole collimators.

As the square-hole collimator does not represent an actual existing collimator, it was not expected that any simulations using it would be able to be compared with experimental results reported elsewhere. As stated earlier, it did provide a simple geometry for developing the $\sigma$ estimation technique.

In the simulation discussed in this section, the point source was simulated as being positioned 13 cm in front of the collimator and surrounded by 3 cm of water. The dimensions of the collimator were:

| | |
|---|---|
| septal thickness, $s$ | 1 mm, |
| hole size, $d$ | 1 mm |
| collimator length, $L$ | 60 mm. |

The top of each square-hole was modelled to be filled with 10 mm NaI(Tl) to act as a detector.

### 6.3.2 Results and discussion

The sensitivity and PSF were considered in the energy window of 50–300 keV for $^{90}$Y and 130–151 keV for $^{99m}$Tc. The sensitivity is defined as the number of detected photons divided by the number of particles emitted by the source. Figure 6.6 and 6.7 show estimates of $\sigma$ for full Monte Carlo $^{90}$Y and $^{99m}$Tc sources respectively for the source being shifted at different distances, $r$ from its initial positions. The estimation of $\sigma$ fluctuates as the number of photons detected at each hole varies with the hole distance with central axis. Photons were detected mostly in the central area and as the distance from the centre increases, fewer photons were detected. As the number of photons detected decreases, the reliability of the estimates of $\sigma$ decreases. This is demonstrated in the graphs where the estimates of $\sigma$ is generally more consistent at the centre region and get worse further from the centre.

The FWHM of the point spread function was calculated using equation 6.2, where $\sigma$ was taken as the mean value from the $\sigma$ estimation from different hole positions. The sensitivity and the FWHM values of the $^{90}$Y and $^{99m}$Tc sources for square-hole collimator are reported in Table 6.1. The FWHM values in Table 6.1 are quite small compared to what is usually encountered in gamma camera systems. However, as the collimator holes are quite narrow, this is consistent with what would be expected. Also, the FWHM for $^{90}$Y is larger than $^{99m}$Tc, which is again consistent with what would be expected. This is because bremsstrahlung photon production from $^{90}$Y decay in water is low. Even though a large energy window (50–300 keV) was used, most photons produced have energies below 50 keV. This means most of the bremsstrahlung photons that were produced cannot be detected thus contributed to low sensitivity for $^{90}$Y source. The results also show that the point spread of $^{90}$Y was greater than the $^{99m}$Tc. This is because bremsstrahlung photons are produced at few millimetres from the source and that higher-energy bremsstrahlung photons are able to penetrate the septa more easily, producing greater $\sigma$ estimation for $^{90}$Y source.

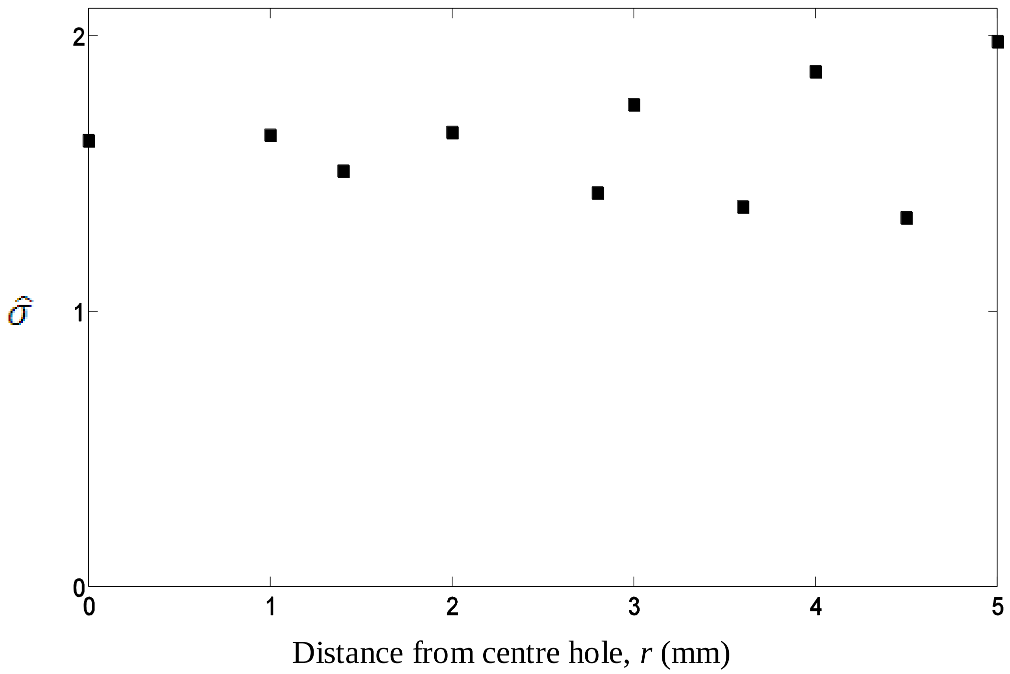


**Figure 6.6: Estimates of $\sigma$ for a full Monte Carlo $^{90}Y$ point source using a square-hole collimator.**

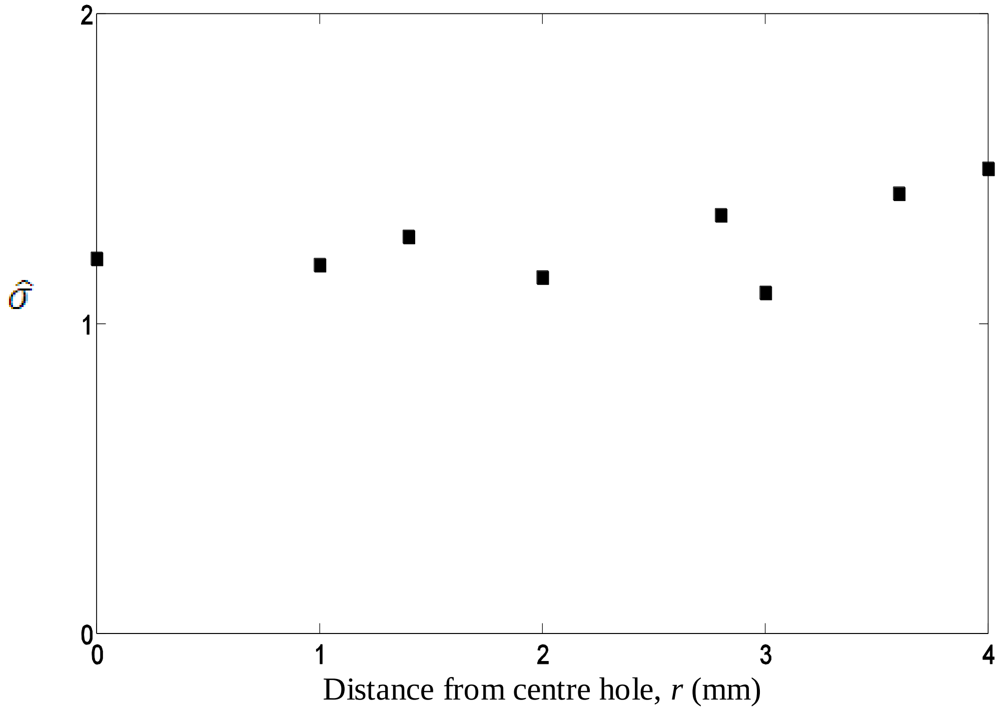


**Figure 6.7: Estimates of $\sigma$ for a $^{99m}Tc$ point source using a square-hole collimator.**

**Table 6.1: Sensitivity and the calculated FWHM of $^{90}$Y and $^{99m}$Tc point sources in water at 13 cm from the square-hole collimator**

| Source | Sensitivity ($\times 10^{-5}$) | FWHM (mm) |
|---|---|---|
| $^{90}$Y | 2.6 | 3.88 |
| $^{99m}$Tc | 3.5 | 2.98 |

## 6.4 Validation

### 6.4.1 Method

In this section, the accuracy of the collimator simulation model and the consistency of the $\sigma$ estimation method for the PSF were validated by comparing the Monte Carlo simulation results with the experimental data obtained from other research groups. The simulations and experimental data were compared in terms of the sensitivity and the collimator spatial resolution. In order to quantify the resolution, the FWHM were computed on the PSF using the $\sigma$ estimation method described in the previous section.

The geometry set-up of the gamma camera simulation was similar to the set-up illustrated in Figure 6.2. Two types of collimators, low-energy high-resolution (LEHR) and medium-energy general-purpose (MEGP), were simulated for different gamma-emitting radionuclides, namely $^{99m}$Tc and $^{123}$I for the respective collimator type. The hexagonal-shape holes for the LEHR and MEGP collimators were given dimensions according to the specification reported in the experimental studies conducted by Bahreyni et al (2010) and Rault (2011). The dimensions of the collimator holes are summarised in Table 6.2.

The simulation of a $^{99m}$Tc point source with LEHR collimator was compared with work by Bahreyni et al. (2010). The experimental work were performed with the $^{99m}$Tc point source (of 1.5 mm in diameter) placed at 10 cm from the collimator surface and the sensitivity and spatial resolution properties were acquired at the energy window of 130−151 keV.

The simulation of a $^{123}$I point source simulation with MEGP collimator was compared with work done by Rault et al. (2011). The sensitivity and PSF were acquired for $^{123}$I point source positioned in a cylinder water phantom (22.2 cm diameter, 18.6 cm height) at 15 cm from the collimator. The data were computed within the 143−175 keV energy window.

In the simulation work, $1\times10^8$ of photons from the gamma-emitting radionuclide sources were simulated.

**Table 6.2: Collimator design parameters**

| | Hole length, *L* (mm) | Hole diameter, *d* (mm) | Septal thickness, *s* (mm) |
|---|---|---|---|
| LEHR | 24.0 | 1.1 | 0.16 |
| MEGP | 58.0 | 3.0 | 1.05 |

### 6.4.2 Results and discussion

The validation of the full Monte Carlo simulation results against data obtained from experimental measurement was essential to assess the consistency and the reliability of the simulation method. $\sigma$ was estimated using the method explained in section 6.2, and the corresponding FWHM was computed. The sensitivity and the FWHM were considered in the energy window of 130−151 keV for $^{99m}$Tc and 143−175 keV for $^{123}$I. The $\sigma$ estimates for $^{99m}$Tc and $^{123}$I are shown in Figure 6.8 and 6.9 respectively. The sensitivity and FWHM values are listed in Table 6.3 and 6.4.

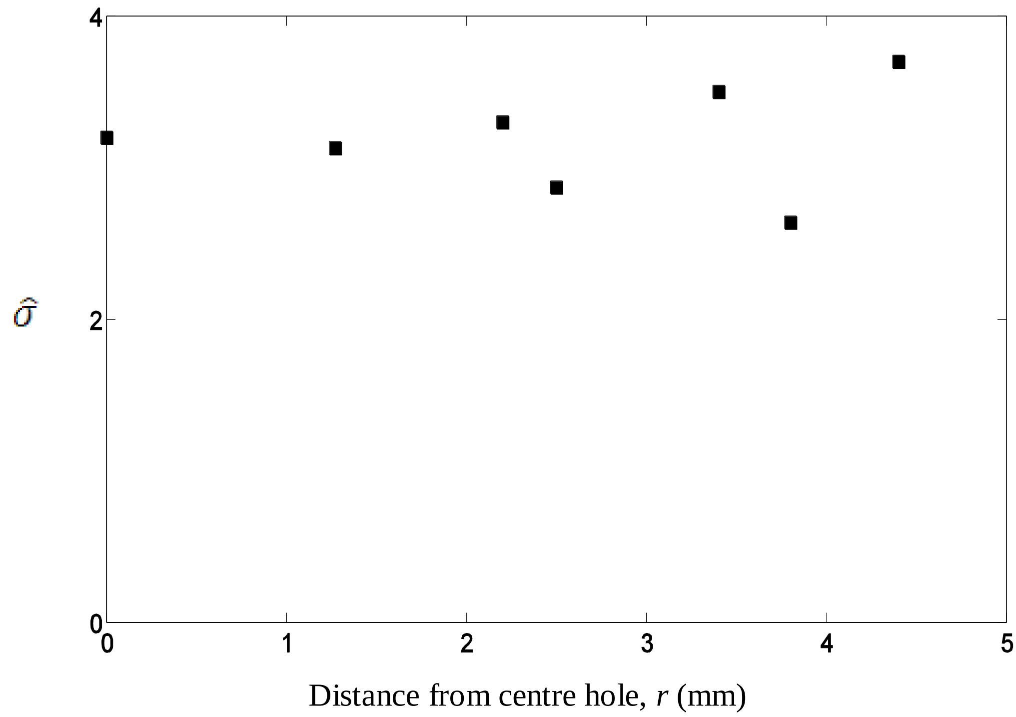


**Figure 6.8: Estimates of $\sigma$ for a $^{99m}$Tc point source in air at 10 cm from the collimator.**

**Table 6.3: Sensitivity and FWHM values obtained from simulation and experimental measurement of LEHR collimator for $^{99m}$Tc point source in air at 10 cm from the collimator. The percentage difference between the simulation and measured results are indicated**

| Collimator | Sensitivity (×10$^{-5}$) | | FWHM (mm) | |
|---|---|---|---|---|
| | Measured | Simulated | Measured | Simulated |
| LEHR | 8.5 | 9.7 (14.2%) | 8.4 | 7.5 (10.7%) |

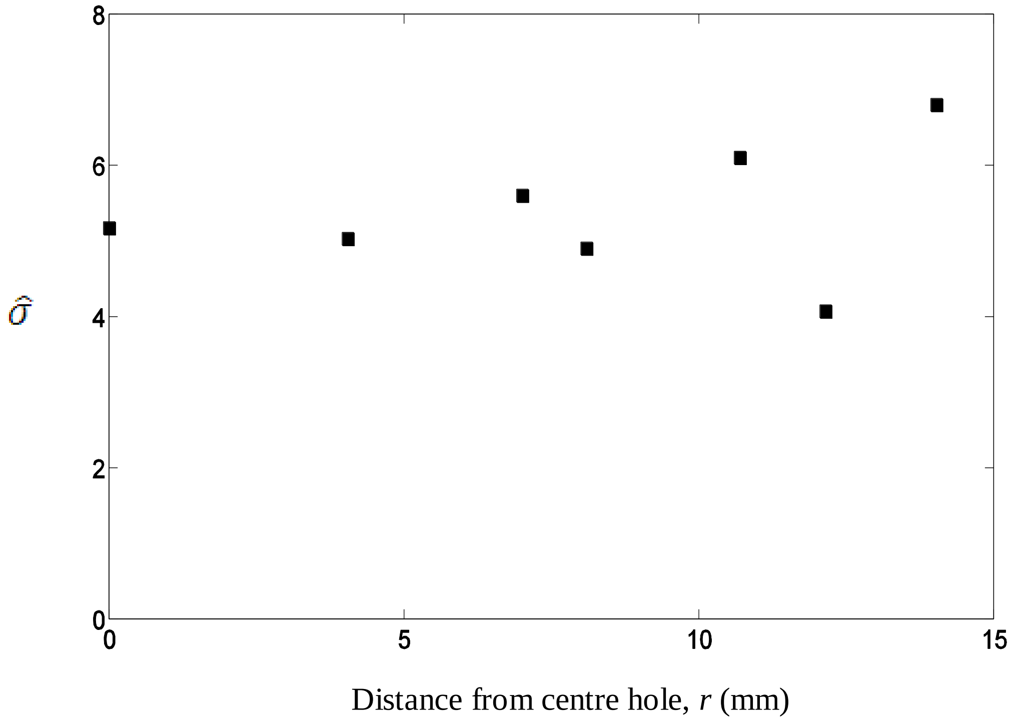


**Figure 6.9: Estimates of $\sigma$ for a $^{123}$I point source in water at 15 cm from the collimator.**

**Table 6.4: Sensitivity and FWHM values obtained from simulation and experimental measurement for MEGP collimator for $^{123}$I point sources in water at 15 cm from the collimator. The percentage difference between the simulation and measured results are indicated in brackets**

| Collimator | Sensitivity ($\times 10^{-5}$) | | FWHM (mm) | |
|---|---|---|---|---|
| | Measured | Simulated | Measured | Simulated |
| MEGP | 3.1 | 3.7 (19.4%) | 14.8 | 12.6 (14.9%) |

To assess the validity of our collimator model and estimation method, the simulation data were compared in terms of the sensitivity and spatial resolution with the experimental studies. The differences in the FWHMs between the simulated and experimental results occur mainly due to the fact that the simulation work did not take into account the intrinsic spatial resolution due to the gamma cameras photomultiplier tubes and the associated electronics, and the inability of the electronics to detect every photon precisely. As is expected, the sensitivity is greater and the FWHM is smaller in the estimates obtained from the simulations than those from the measured experimental results.

## 6.5 Evaluation of kernel-based photon source

### 6.5.1 Method

While the kernel-based Monte Carlo simulated point source appears to closely match that of a full Monte Carlo simulation of $^{90}$Y point source, as demonstrated in the previous chapter, it is important to test it in a simulation of a 'realistic' situation. It was decided to do this by estimating a point spread function parameter for a point source as ‘seen’ through a gamma camera collimator. Again it was decided not to simulate a whole gamma camera detection process, but to only consider the collimation and NaI detection rather than include the whole image formation chain which is not necessary and may introduce additional factors.

Again, the simulation set-up illustrated in Figure 6.2 was used, with the source being 13 cm from the collimator and the spherical water phantom having a 3 cm radius. The sensitivities of the detection system and the estimates of full-width at half-maximum (FWHM) of the ‘image’ of the point source formed by the collimator were made for four different models of $^{90}$Y source:

i) a full $^{90}$Y point source Monte Carlo situation

ii) a $^{90}$Y point source modelled as a kernel-based photon source

iii) a $^{90}$Y point source modelled as a kernel-based photon source but with the photons being emitted isotropically from the shells

iv) a $^{90}$Y point source modelled as a photon source with the $^{90}$Y bremsstrahlung spectrum

The different models of the bremsstrahlung photon source were used in the simulations to evaluate their accuracy and to compare their simulation time.

Previous studies have shown that the use of medium-energy collimator (Rault et al., 2009; Shen, et al., 1994b) is optimal for bremsstrahlung imaging. For the full $^{90}$Y point source Monte Carlo simulation, $1\times10^{10}$ disintegrations were simulated while for the photon source simulations the equivalent number of bremsstrahlung, which is $8.6\times10^{8}$ were simulated. Wide energy windows 50–300 keV are used to detect the photons as previously recommended for the bremsstrahlung imaging for better sensitivity (Clarke, et al., 1992; Rault, et al., 2010; Shen, et al., 1994b). Several estimates of $\sigma$, and thus of FWHM, were made using each of the four models.

### 6.5.2 Results and discussion

The sensitivities of the detection system given by the different simulation models, together with the time that each simulation took, are shown in Table 6.5.

**Table 6.5: Sensitivity values and simulation times for the different simulation methods**

| Source simulation method | Sensitivity ($\times 10^{-5}$) | Simulation time (min) |
|---|---|---|
| Full Monte Carlo $^{90}Y$ point source | 1.02 | 8700 |
| Photon kernel with anisotropic emission | 1.31 | 362 |
| Photon kernel with isotropic emission | 1.31 | 338 |
| Photon point source with $^{90}Y$ bremsstrahlung spectrum | 1.46 | 283 |

The sensitivity of the full Monte Carlo simulation of $^{90}Y$ point source and kernel-based photon sources was generally low. This results in the main limitation of Monte Carlo simulations for $^{90}Y$ bremsstrahlung imaging, which is poor statistical uncertainty, where only 1 out of 100 000 photons were being detected. The computation time for the full Monte Carlo simulation of $^{90}Y$ is considerably more than for the others. There are clearly considerable gains in computational speed to be had by using the kernel-based photon source models. Using the kernel-based photon source approach, source particles can be simulated and tracked with shorter computer time. Thus for a given amount of time, more particles can be simulated to improve the statistics. Therefore this approach is to be preferred providing that it is sufficiently accurate.

The sensitivity of the collimator depends on summing the number of photons detected in each hole. A point photon source positioned directly under a hole is slightly more likely to have its photons pass through the collimator than one positioned under a septum. This explains why the sensitivity for photon point source with bremsstrahlung spectrum was the highest. The sensitivities for other source models were slightly lower than bremsstrahlung point source because the photons were spread around the centre. Some of the photons would be created under septa and would be less likely pass through a hole, thus reducing the sensitivity. The reason why the full $^{90}$Y Monte Carlo simulation produces the lowest sensitivity is not clear.

Figures 6.10 – 6.13 show the $\sigma$ estimates for a full Monte Carlo simulation of a $^{90}$Y point source and for the different kernel-based photon source models. The estimates vary more and more as the distance increases as the number of photons detected decreases with lateral distance. In order to evaluate the kernel-based photon source, $\sigma$ estimation was obtained for the PSF and the resolution was calculated as $FWHM = 2\sigma\sqrt{2\ln 2}$. From these $\sigma$ estimates the FWHMs in the different situations are displayed in Table 6.6.

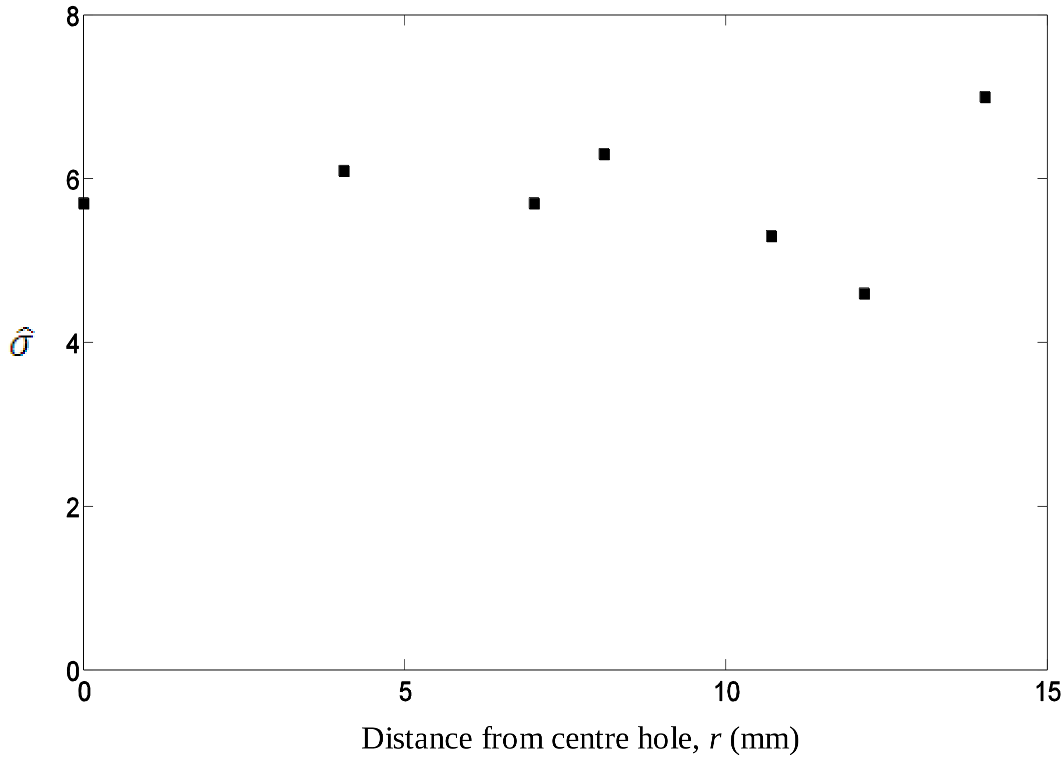


**Figure 6.10: Estimates of $\sigma$ using a fully simulated $^{90}Y$ point source.**

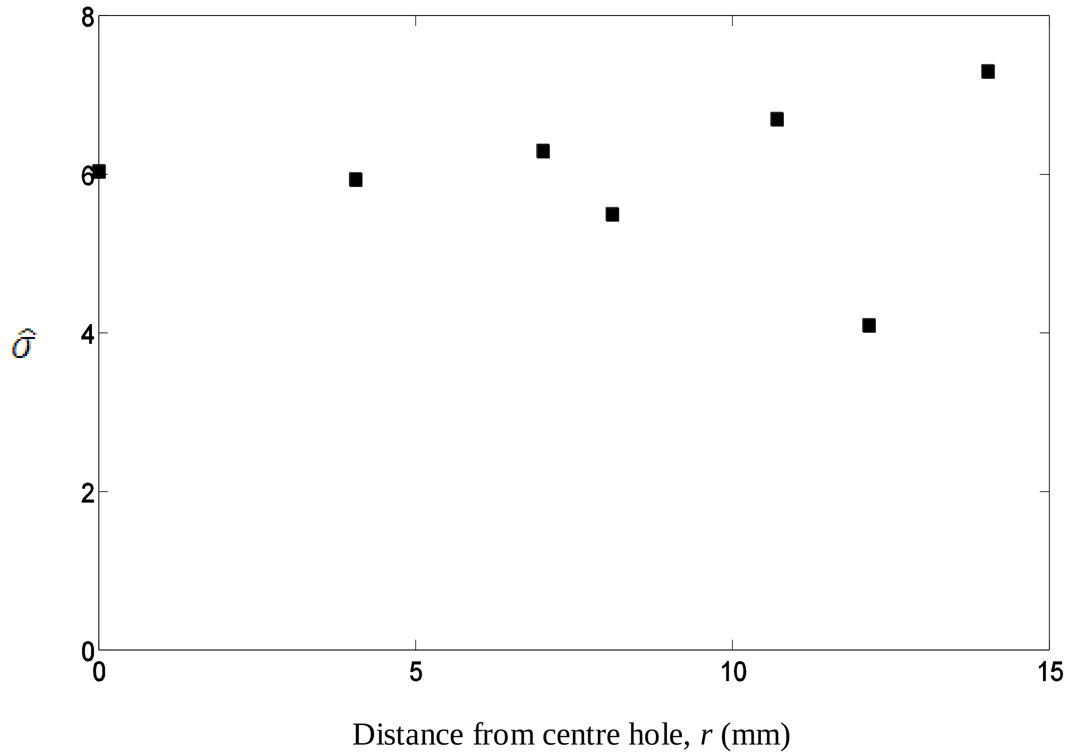


**Figure 6.11: Estimates of $\sigma$ using a kernel-based photon source with anisotropic emission.**

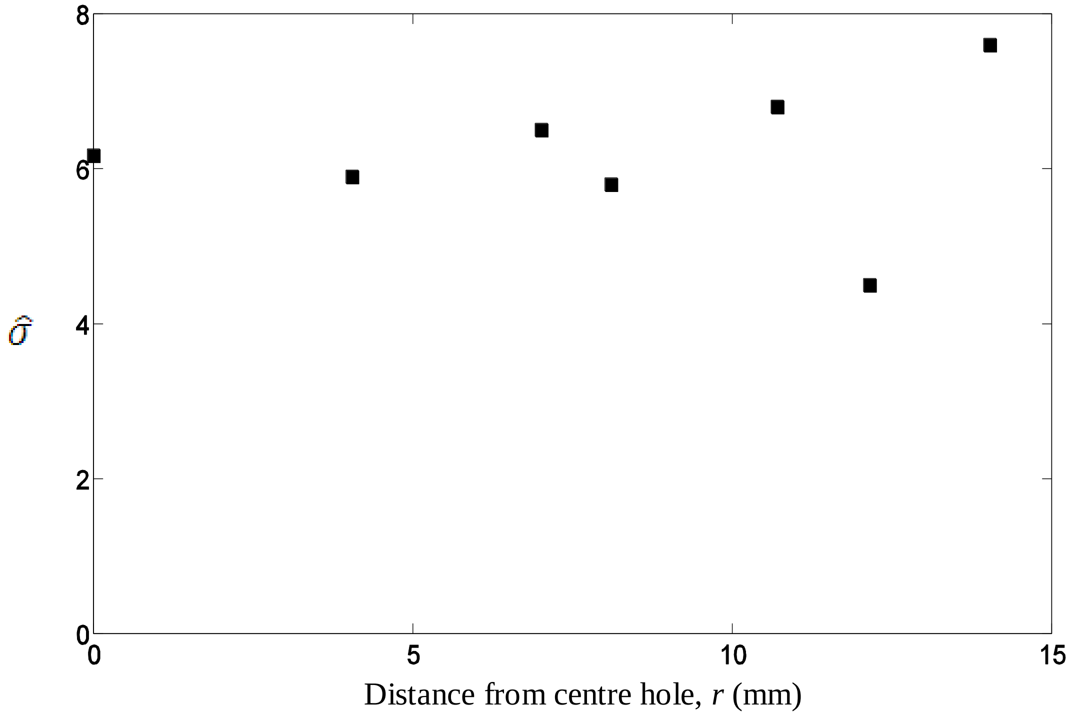


**Figure 6.12: Estimates of $\sigma$ using a kernel-based photon source with isotropic emission.**

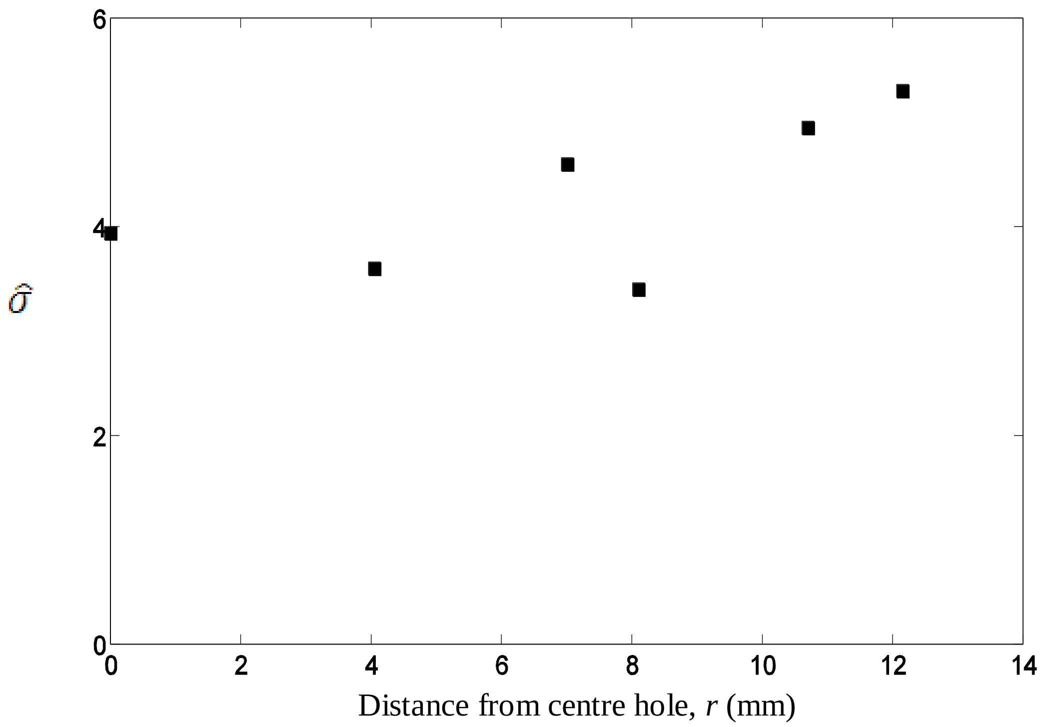


**Figure 6.13: Estimates of $\sigma$ using a photon point source with $^{90}Y$ bremsstrahlung spectrum.**

**Table 6.6: FWHM values for different source simulation methods**

| Source simulation method | FWHM (mm) |
|---|---|
| Full Monte Carlo $^{90}Y$ point source | 13.7 |
| Photon kernel with anisotropic emission | 14.1 |
| Photon kernel with isotropic emission | 14.5 |
| Photon point source with $^{90}Y$ bremsstrahlung spectrum | 10.1 |

FWHMs obtained by the full Monte Carlo $^{90}Y$ point source and kernel-based photon source models were larger than those obtained from the photon point source with the $^{90}Y$ bremsstrahlung spectrum. This is expected because the bremsstrahlung photons were created away from the position of the $^{90}Y$ point source thus forming a spread source which resulted in the increased FWHMs. For the photon point source, all the high-energy photons originated from a single position and so the corresponding FWHM is the lowest.

The results show that although the FWHM for the photon kernel with anisotropic emission is slightly lower than that of the photon kernel with isotropic emission, the difference is small. The photon kernel-based representation of the $^{90}Y$ point source with anisotropic photon emission only overestimates the FWHM as estimated by the full Monte Carlo simulation by 3%, whereas the photon kernel-based representation of the $^{90}Y$ point source with isotropic photon emission overestimates the FWHM by 6%. However, the FWHM determined for point photon source with a $^{90}Y$ photon spectrum was 26% less than that determined by a full Monte Carlo simulation of the true $^{90}Y$ point source. Thus the photon point source model should not be considered to be an adequate representation of the $^{90}Y$

source, while the kernel-based photon source models are adequate with a preference for the photon kernel with anisotropic emission model.

There is a little to be gained in term of its accuracy by choosing to use the more precise anisotropic photon emission kernel over the isotropic one. However the small extra computation time required for anisotropic photon source kernel is probably not an issue in almost all situations and should be used in preference.

The FWHM of the $^{90}Y$ and kernel-based photon source obtained in this work were smaller compared to those obtained from Rault et al. (2010). This is because, as mentioned earlier, we did not consider the limitation of intrinsic resolution. Furthermore, while our simulation used a point source, they defined the source as spherical source of 15.8 mm diameter, which is hardly a point source. The source–collimator distance was also larger in their simulation and this contributed to larger FWHM.

## 6.6 Summary

A method of estimating the FWHM of a point source as seen by a gamma camera collimator was described and used in this research. It is used as a way of comparing the distribution of detected photons for the different point sources and collimator types. The method and the collimator model were validated by comparing the results with experimental data. The method seems to be quite adequate in that the FWHM estimates that it provides are quite realistic and consistent. It is suitable for assessing the likely changes to the FWHMs when different source models and different collimator types are used.

The accuracy and speed of the kernel-based photon source were also evaluated in this chapter. Estimation of the $\sigma$ and thus the FWHM is used to compare the different kernel-based photon source models to represent a ‘real’ source generated by a full $^{90}Y$ Monte Carlo simulation. The results show that the FWHMs of the kernel-based photon source models were comparable to full Monte Carlo simulation of $^{90}Y$ point source. The FWHM determined for photon point source with a $^{90}Y$ photon spectrum underestimates the full Monte Carlo simulation of the true $^{90}Y$ point source. This demonstrates that accounting for the fact that the bremsstrahlung photons are emitted at a distance away from the source is vital and all of the photons cannot be assumed to come from a single point. It is more computationally efficient to use this source model than the photon kernel-based ones as shown by it having the shortest computation time, but it is quite inaccurate.

The results show that the kernel-based photon source can be used to replace a beta point source and greatly improve the simulation time by almost 30 times. Simplifying the kernel by disregarding the anisotropic nature of the photon emission reduces the accuracy of the model slightly, although the reduction in simulation time is sufficiently small that the more accurate anisotropic kernel should be preferred.

# CHAPTER 7

# CONCLUSIONS AND RECOMMENDATIONS

## 7.1 Conclusions

As emission of primary photons by $^{90}Y$ is relatively rare, imaging is better done acquiring the bremsstrahlung emissions events created from $^{90}Y$ decay. However, the main limitations of bremsstrahlung imaging are low photon counts and poor resolution. The Monte Carlo technique offers a reliable method to improve bremsstrahlung imaging, however, a large number of particle histories needs to be simulated in order to decrease the statistical uncertainty. Monte Carlo simulation of bremsstrahlung imaging is particularly time consuming because of the low production of bremsstrahlung photons and the slow Monte Carlo electron transport simulation.

This study proposes that for Monte Carlo simulation purposes, bremsstrahlung photons produced from a $^{90}Y$ beta point source are replaced with a kernel-based photon source. This is initially done by investigating the energy spectrum, the spatial and angular distributions of the bremsstrahlung photons to establish their relationship. A method to estimate the full-width half-maximum (FWHM) is also developed in order to evaluate the accuracy and speed of the kernel-based photon source by comparing it to the full Monte Carlo simulation of $^{90}Y$ point source.

A positive outcome has been achieved using the kernel-based photon source where the simulation time is greatly improved. This will allow more Monte Carlo studies to be carried out to optimise bremsstrahlung imaging techniques to obtain more accurate images. Faster Monte Carlo simulation will also instigate further development in the area of bremsstrahlung imaging research especially in the imaging technique, scatter correction and reconstruction algorithm. Sometimes dosimetry calculations for $^{90}Y$ therapy were computed based on the imaging of surrogate radionuclides like $^{111}In$ and $^{99m}Tc$. From the reviews, we are aware that imaging using surrogates does not predict $^{90}Y$ distributions precisely and may affect the dosimetry calculations and overall treatment planning. Therefore it is obvious that it is important to improve the bremsstrahlung imaging technique. Faster simulation of $^{90}Y$ bremsstrahlung using Monte Carlo techniques will allow this research to proceed at a faster rate.

Previous studies conducted to increase the $^{90}Y$ bremsstrahlung simulation speed only accounted for isotropic bremsstrahlung photon emission. This research attempts to demonstrate the importance of modelling the anisotropic emission of the bremsstrahlung, as well as taking into account its emission positions. This obviously leads to a better representation of bremsstrahlung emission of $^{90}Y$. We find that defining anisotropic emission for the kernel-based photon is not that vital, as argued by previous researchers, but it does offer some improvements. Its simulation time is only slightly more than the isotropic emission kernel-based photon source model. Therefore the correct modelling of the emission direction is preferable as it is more accurate but does not require a significantly increased computation time.

There are assumptions made in this study that may result in limitations in the method. The simulations assume medium with constant density and homogenous compositions. The substitute photon source of $^{90}Y$ point source was developed as a kernel and is different from approach taken from previous researchers. Although these assumptions are made, results that the kernel-based photon source accurately emulates a $^{90}Y$.

The kernel-based photon source was built only based on the distribution of bremsstrahlung photons produced from beta decay interactions. We did not take the gamma emission from $^{90}Zr$ decay into account, so its effects on the kernel-based source were not studied in this thesis.

## 7.2 Recommendations

Now that we have proved that it is possible to replace $^{90}Y$ point source with kernel-based photon source, a future aspiration would be to expand the use of the fast simulation method of $^{90}Y$ bremsstrahlung in the related area. It would be beneficial to study its implementation in the reconstruction or scatter correction methods which have not been made in this study.

The kernel-based photon source can also be developed by including the gamma-ray emission from the decay of the excited state of $^{90}Zr$. Its affect on the point spread function might offer new perspective on the $^{90}Y$ bremsstrahlung imaging studies.

The approach of using photon source as substitute for tracking electrons in Monte Carlo simulation can also be implemented to other beta-emitting radioisotopes like $^{89}Sr$ and $^{32}P$ which has lower bremsstrahlung events probability. The method can also be implemented to other materials in order to investigate its applicability on other tissues or organs.

# REFERENCES


Agostinelli, S., Allison, J., & Amako, K. (2003). GEANT4-a simulation toolkit. *Nucl. Instrum. Methods Phys. Res. A, 506*(3), 250-303.

Alvarez, R. D., Huh, W. K., Khazaeli, M. B., Meredith, R. F., Partridge, E. E., Kilgore, L. C., Grizzle, W. E., et al. (2002). A Phase I Study of Combined Modality 90Yttrium-CC49 Intraperitoneal Radioimmunotherapy for Ovarian Cancer. *Clin. Canc. Res., 8*(9), 2806-2811.

Amako, K., Guatelli, S., Ivanchenko, V. N., Maire, M., Mascialino, B., Murakami, K., Nieminen, P., et al. (2005). Comparison of Geant4 Electromagnetic Physics Models Against the NIST Reference Data. *IEEE Transactions on Nuclear Science, 52*(4), 910-918

Andreo, P. (1991). Monte Carlo techniques in medical radiation physics. *Phys. Med. Biol., 36*, 861-920.

Anger, H. O. (1958). Scintillation camera. *Rev. Sci. Instrum., 29*(1), 27-33.

Avila-Rodriguez, M. A., Selwyn, R. G., Hampel, J. A., Thomadsen, B. R., DeJesus, O. T., Converse, A. K., & Nickles, R. J. (2007). Positron-emitting resin microspheres as surrogates of 90Y SIR-Spheres: a radiolabeling and stability study. *Nucl. Med. Biol., 34*(5), 585-590.

Bahreyni, T. M., Islamian, J., Momennezhad, M., Ljungberg, M., & Naseri, S. (2010). SIMIND Monte Carlo simulation of a single photon emission CT. *Journal of Medical Physics, 35*(1), 42-47.

Bardiès, M., Flux, G., Lassmann, M., Monsieurs, M., Savolainen, S., & Strand, S.-E. (2006). Quantitative imaging for clinical dosimetry. *Nucl. Instrum. Methods Phys. Res. A, 569*(2), 467-471.

Barone, R., Borson-Chazot, F., Valkema, R., Walrand, S., Chauvin, F., Gogou, L., Kvols, L. K., et al. (2005). Patient-Specific Dosimetry in Predicting Renal Toxicity with 90Y-DOTATOC: Relevance of Kidney Volume and Dose Rate in Finding a Dose-Effect Relationship. *J. Nucl. Med., 46*(1_suppl), 99S-106.

Bayouth, J. E., & Macey, D. J. (1994). Quantitative imaging of holmium-166 with an Anger camera. *Phys. Med. Biol., 39*, 265-279.

Berger, M. J. (1971). Distribution of absorbed dose around point sources of electrons and beta particles in water and other media. *J. Nucl. Med., 12*(Suppl. 5 pamphlet No. 7 .), 6-23.

Brans, B., Bodei, L., Giammarile, F., Linden, O., Luster, M., Oyen, W., & Tennvall, J. (2007). Clinical radionuclide therapy dosimetry: the quest for the Holy Gray. *European Journal of Nuclear Medicine and Molecular Imaging, 34*, 772-786.

Breitz, H. B., Fisher, D. R., Weiden, P. L., Durham, J. S., Ratliff, B. A., Bjorn, M. J., Beaumier, P. L., et al. (1993). Dosimetry of Rhenium-186-Labeled Monoclonal Antibodies: Methods, Prediction from Technetium-99m-Labeled Antibodies and Results of Phase I Trials. *J. Nucl. Med., 34*(6), 908-917.

Buck, A. K., Nekolla, S., Ziegler, S., Beer, A., Krause, B. J., Herrmann, K., Scheidhauer, K., et al. (2008). SPECT/CT. *J. Nucl. Med., 49*(8), 1305-1319.

Carrasquillo, J. A., White, J. D., Paik, C. H., Raubitschek, A., Le, N., Rotman, M., Brechbiel, M. W., et al. (1999). Similarities and Differences in $^{111}$In- and $^{90}$Y-Labeled 1B4M-DTPA AntiTac Monoclonal Antibody Distribution. *J. Nucl. Med., 40*(2), 268-276.

Cherry, S. R., Sorenson, J. A., & Phelps, M. E. (2003). *Physics in Nuclear Medicine* (3rd ed.). Philadephia: Elsevier.

Chetty, I. J., Curran, B., Cygler, J. E., DeMarco, J. J., Ezzel, G., Faddegon, B. A., Kawrakow, I., et al. (2007). Report of the AAPM Task Group No. 105: Issues associated with clinical implementation of Monte Carlo-based photon and electron external beam treatment planning. *Med. Phys. , 34*(12), 4818-4853.

Chowdhury, F. U., & Scarsbrook, A. F. (2008). The role of hybrid SPECT-CT in oncology: current and emerging clinical applications. *Clin. Radiol., 63*(3), 241-251.

Cipriani, C., Atzei, G., Argirò, G., Boemi, S., Shukla, S., Rossi, G., & Sedda, A. F. (1997). Gamma camera imaging of osseous metastatic lesions by strontium-89 bremsstrahlung. *Eur. J. Nucl. Med. Mol. Imaging, 24*(11), 1356-1361.

Clarke, K. G., Odom-Maryon, T. L., Williams, L. E., Liu, A., Lopatin, G., Chou, J., Farino, G. M., et al. (1999). Intrapatient consistency of imaging biodistributions and their application to predicting therapeutic doses in a phase I clinical study of $^{90}$Y-based radioimmunotherapy. *Med. Phys., 26*(5), 799-809.

Clarke, L. P., Cullom, S. J., Shaw, R., Reece, C., Penney, B. C., King, M. l. A., & Silbiger, M. (1992). Bremsstrahlung Imaging Using the Gamma Camera: Factors Affecting Attenuation. *J. Nucl. Med., 33*(1), 161-166.

DeNardo, G. L., Juweid, M. E., White, C. A., Wiseman, G. A., & DeNardo, S. J. (2001). Role of radiation dosimetry in radioimmunotherapy planning and treatment dosing. *Crit. Rev. Oncol. Hematol., 39*(1-2), 203-218.

DeNardo, S. J., Kramer, E. L., O'Donnell, R. T., Richman, C. M., Salako, Q. A., Shen, S., Noz, M., et al. (1997). Radioimmunotherapy for Breast Cancer Using Indium-lll/Yttrium-90 BrE-3: Results of a Phase I Clinical Trial. *J. Nucl. Med., 38*(8), 1180-1185.

Druce, M. R., Lewington, V., & Grossman, A. B. (2009). Targeted Radionuclide Therapy for Neuroendocrine Tumours: Principles and Application. *Neuroendocrinology, 91*(1), 1-15.

Enger, S. A., Hartman, T., Carlsson, J., & Lundqvist, H. (2008). Cross-fire doses from beta-emitting radionuclides in targeted radiotherapy. A theoretical study based on experimentally measured tumor characteristics. *Phys. Med. Biol., 53*, 1909-1920.

Erdi, A. K., Erdi, Y. E., Yorke, E. D., & Wessels, B. W. (1996). Treatment planning for radio-immunotherapy. *Phys. Med. Biol.*(10), 2009.

Evans, R. D. (1955). *The Atomic Nucleus*. New York: McGraw-Hill.

Faddegon, B. A., Asai, M., Perl, J., Ross, C., Sempau, J., Tinslay, J., & Salvat, F. (2008). Benchmarking of Monte Carlo simulation of bremsstrahlung from thick targets at radiotherapy energies. *Med. Phys., 35*(10), 4308-4317.

Flux, G., Bardiès, M., Monsieurs, M., Savolainen, S., Strand, S.-E., & Lassmann, M. (2006). The impact of PET and SPECT on dosimetry for targeted radionuclide therapy. *Z. Med. Phys., 16*, 47-59.

Ford, K. W. (1955). Predicted 0+ Level in $_{40}Zr^{90}$. *Phys. Rev., 98*(5), 1516.

Friedberg, J. W. (2004). Radioimmunotherapy for Non-Hodgkin's Lymphoma. *Clin. Canc. Res.*, *10*(23), 7789-7791.

Gulec, S., Pennington, K., Hall, M., & Fong, Y. (2009). Preoperative Y-90 microsphere selective internal radiation treatment for tumor downsizing and future liver remnant recruitment: a novel approach to improving the safety of major hepatic resections. *World J. Surg. Oncol., 7*(1), 6.

Hamami, M. E., Poeppel, T. D., Muller, S., Heusner, T., Bockisch, A., Hilgard, P., & Antoch, G. (2009). SPECT/CT with 99mTc-MAA in Radioembolization with 90Y Microspheres in Patients with Hepatocellular Cancer. *J. Nucl. Med., 50*(5), 688-692.

Hamoudeh, M., Kamleh, M. A., Diab, R., & Fessi, H. (2008). Radionuclides delivery systems for nuclear imaging and radiotherapy of cancer. *Adv. Drug Deliv. Rev., 60*(12), 1329-1346.

Heard, S., Flux, G., Guy, M. J., & Ott, R. J. (2004a). Photon Source Kernels for Monte Carlo Simulation of Bremsstrahlung Imaging. *Eur. J. Nucl. Med., 31*(S2).

Heard, S., Glenn, D. F., Guy, M. J., & Ott, R. J. (2004b). Monte Carlo Simulation of $^{90}$Y Bremsstrahlung Imaging. *Nuclear Science Symposium Conference Record IEEE, 6*, 3579- 3583.

Helisch, A., Förster, G. J., Reber, H., Buchholz, H.-G., Arnold, R., Göke, B., Weber, M. M., et al. (2004). Pre-therapeutic dosimetry and biodistribution $^{86}$Y-DOTA-Phe$^{1}$-Tyr$^{3}$-octreotide versus $^{111}$In-pentetreotide in patients with advanced neuroendocrine tumours. *Eur. J. Nucl. Med. Mol. Imaging, 31*(10), 1386-1392.

Hendee, W. R., & Ritenour, E. R. (2002). *Medical Imaging Physics* (Fourth ed.). New York: Wiley-Liss.

Hendrix, C. (2004). Radiation safety with Yttrium 90 ibritumomab tiuxetan (Zevalin) radioimmunotherapy. *Seminars in Oncology Nursing, 20*(Supplement 1), 14-19.

Ito, S., Kurosawa, H., Kasahara, H., Teraoka, S., Ariga, E., Deji, S., Hirota, M., et al. (2009). 90Y bremsstrahlung emission computed tomography using gamma cameras. *Ann. Nucl. Med., 23*(3), 257-267.

Johnson, O. E., Johnson, R. G., & Langer, L. M. (1955). Evidence for a 0+ First Excited State in $Zr^{90}$. *Phys. Rev., 98*(5), 1517.

Johnson, T. K., Cole, W., Quaife, R. A., Lear, J. L., Ceriani, R. L., Jones, R. B., & Cagnoni, P. J. (2002). Biokinetics of Yttrium-90 –Labeled huBrE-3 Monoclonal Antibody. *CANCER, 94*(4), 1240-1248.

Jonsson, B.-A., Strand, S.-E., & Larsson, B. S. (1992). A Quantitative Autoradiographic Study of the Heterogeneous Activity Distribution of Different Indium-111-Labeled Radiopharmaceuticals in Rat Tissues. *J. Nucl. Med., 33*(10), 1825-1833.

Kassis, A. I., & Adelstein, S. J. (2005). Radiobiologic Principles in Radionuclide Therapy. *J. Nucl. Med., 46*(Suppl 1), 4S-12.

Kawrakow, I., & Bielajew, A. F. (1998). On the condensed history technique for electron transport. *Nucl. Instrum. Methods Phys. Res. B, 142*(3), 253-280.

Kimiaei, S., Larsson, S. A., & Jacobsson, H. (1996). Collimator design for improved spatial resolution in SPECT and planar scintigraphy. *J. Nucl. Med., 37*, 1417-1421.

King, J., Quinn, R., Glenn, D. M., Janssen, J., Tong, D., Liaw, W., & Morris, D. L. (2008). Radioembolization with selective internal radiation microspheres for neuroendocrine liver metastases. *Cancer, 113*(5), 921-929.

Knešaurek, K., Josef, M., Mmuzinic, M., DaCcosta, M., Zhang, Z., & Heiba, S. (2010). Quantitative comparison of yttrium-90 ($^{90}Y$)-microspheres and technetium-99m ($^{99m}Tc$)-macroaggregated albumin SPECT images for Planning $^{90}Y$ therapy of liver cancer. *Tech. Canc. Res. Treat., 9*(3), 253-261.

Kyle, V., Hazelman, B. L., & Wraight, E. P. (1983). Yttrium-90 therapy and 99mTc pertechnetate knee uptake measurements in the management of rheumatoid arthritis. *Ann. Rheum. Dis., 42*, 132-137.

Leichner, P. K., Akabani, G., Colcher, D., Harrison, K. A., Hawkins, W. G., Eckblade, M., Baranowska-Kortylewicz, J., et al. (1997). Patient-Specific Dosimetry of Indium-111- and Yttrium-90-Labeled Monoclonal Antibody CC49. *J. Nucl. Med., 38*(4), 512-516.

Lewington, V. (1993). Targeted radionuclide therapy for bone metastases. *Eur. J. Nucl. Med. Mol. Imaging, 20*(1), 66-74.

Lewington, V. (2003). Targeted radionuclide therapy for neuroendocrine tumours. *Endocr. Relat. Canc., 10*, 497–501.

Lhommel, R., van Elmbt, L., Goffette, P., Van den Eynde, M., Jamar, F., Pauwels, S., & Walrand, S. (2010). Feasibility of $^{90}$Y TOF PET-based dosimetry in liver metastasis therapy using SIR-Spheres. *Eur. J. Nucl. Med. Mol. Imaging, 37*(9), 1654-1662.

Linden, O., Kurkus, J., Garkavij, M., Cavallin-Stahl, E., Ljungberg, M., Nilsson, R., Ohlsson, T., et al. (2005). A Novel Platform for Radioimmunotherapy: Extracorporeal Depletion of Biotinylated and 90Y-Labeled Rituximab in Patients with Refractory B-Cell Lymphoma. *Canc. Biother. Rad., 20*(4), 457-466.

Ma, Y., Zhou, H., & Zhuo, Y. (2006). Condensed-history Monte Carlo simulation of the dosimetric distribution of electron microbeam. *Radiat. Environ. Biophys., 44*(4), 299-305.

Manjunatha, H. C., & Rudraswamy, B. (2010). Bremsstrahlung exposure of tissues from beta-therapeutic nuclides. *Nucl. Instrum. Methods Phys. Res. A, 621*(1-3), 581-589.

Mansberg, R., Sorensen, N., Mansberg, V., & Van der Wall, H. (2007). Yttrium 90 Bremsstrahlung SPECT/CT scan demonstrating areas of tracer/tumour uptake. *Eur. J. Nucl. Med. Mol. Imaging, 34*(11), 1887-1887.

Minarik, D., Gleisner, K. S., & Ljungberg, M. (2008). Evaluation of quantitative 90Y SPECT based on experimental phantom studies. *Phys. Med. Biol., 53*(20), 5689-5703.

Minarik, D., Ljungberg, M., Segars, P., & Sjogreen Gleisner, K. (2009). Evaluation of quantitative planar $^{90}$Y bremsstrahlung whole-body imaging. *Phys. Med. Biol., 54*, 5873–5883.

Moore, S. C., Kouris, K., & Cullum, I. (1992). Collimator design for single photon emission tomography. *Eur. J. Nucl. Med. Mol. Imaging, 19*(2), 138-150.

Murthy, R., Habbu, A., & Salem, R. (2006). Trans-arterial hepatic radioembolisation of yttrium-90 microspheres. *Biomed. Imaging Interv. J., 2*(3), e43.

Murthy, R., Nunez, R., Szklaruk, J., Erwin, W., Madoff, D. C., Gupta, S., Ahrar, K., et al. (2005). Yttrium-90 Microsphere Therapy for Hepatic Malignancy: Devices, Indications, Technical Considerations, and Potential Complications. *Radiographics, 25*(suppl 1), S41-S55.

Nickles, R. J., Roberts, A. D., Nye, J. A., Converse, A. K., Barnhart, T. E., Avila-Rodriguez, M. A., Sundaresan, R., et al. (2004). Assaying and PET imaging of yttrium-90: 1 >>34ppm>>0. *Nuclear Science Symposium Conference Record IEEE, 6*, 3412 - 3414.

Nordell, B., & Brahme, A. (1984). Angular distribution and yield from bremsstrahlung targets. *Phys. Med. Biol., 29*(7), 797-810.

Onthank, D. C., Liu, S., Silva, P. J., Barrett, J. A., Harris, T. D., Robinson, S. P., & Edwards, D. S. (2004). $^{90}$Y and $^{111}$In Complexes of a DOTA-Conjugated Integrin $a_v b_3$Receptor Antagonist:Different but Biologically Equivalent. *Bioconjugate Chem., 15*(2), 235-241.

Pandit-Taskar, N., Batraki, M., & Divgi, C. R. (2004). Radiopharmaceutical Therapy for Palliation of Bone Pain from Osseous Metastases. *J. Nucl. Med., 45*(8), 1358-1365.

Peremans, K., Cornelissen, B., Van Den Bossche, B., Audenaert, K., & Van de Wiele, C. (2005). A Review of Small animal maging planar and pinhole SPECT γ camera imaging. *Veterinary Radiology & Ultrasound, 46*(2), 162-170.

Perkins, A. C. (1999). *Nuclear Medicine in Pharmaceutical Research*. London, UK: CRC Press.

Perkins, A. C. (2008). In vivo molecular targeted radiotherapy. *Biomed. Imaging Interv. J., 1*(2), e9.

Rault, E., Staelens, S., Van Holen, R., De Beenhouwen, J., & Vandenberghe, S. (2010). Fast simulation of yttrium-90 bremsstrahlung photons with GATE. *Med. Phys., 37*(6), 2943-2950.

Rault, E., Staelens, S., Van Holen, R., De Beenhouwen, J., & Vandenberghe, S. (2011). Accurate Monte Carlo modelling of the back compartments of SPECT cameras. *Phys. Med. Biol., 56,* 87-104.

Rault, E., Vandenberghe, S., Staelens, S., De Beenhouwen, J., & Lemahieu, I. (2007). Investigation of yttrium-90 bremsstrahlung with GATE. *J. Nucl. Med., 48*(Supplement 2), 422P.

Rault, E., Vandenberghe, S., Staelens, S., & Lemahieu, I. (2009). Optimization of Yttrium-90 Bremsstrahlung Imaging with Monte Carlo Simulations. *4th European Conference of the International Federation for Medical and Biological Engineering, 22*, 500-504.

Rogers, D. W. O. (2006). Fifty years of Monte Carlo simulations for medical physics*. *Phys. Med. Biol., 51*(13), R287-R301.

Ryde, H., Thieberger, P., & Alvager, P. (1961). Two-Photon De-Excitation of the 0+ Level in Zr90. *Phys. Rev. Lett. , 6*(9), 475–478.

Saha, G. B. (1993). *Physics and radiobiology of nuclear medicine*. New York: Springer-Verlag.

Salem, R., & Thurston, K. G. (2006). Radioembolization with Yttrium-90 Microspheres: A State-of-the-Art Brachytherapy Treatment for Primary and Secondary Liver Malignancies: Part 3: Comprehensive Literature Review and Future Direction. *J. Vasc. and Interv. Radiol., 17*(10), 1571-1593.

Sarfaraz, M., Kennedy, A. S., Cao, Z. J., Sackett, G. D., Yu, C. X., Lodge, M. A., Murthy, R., et al. (2003). Physical aspects of yttrium-90 microsphere therapy for nonresectable hepatic tumors. *Med. Phys., 30*(2), 199-203.

Sarfaraz, M., Kennedy, A. S., Lodge, M. A., Li, X. A., Wu, X., & Yu, C. X. (2004). Radiation absorbed dose distribution in a patient treated with yttrium-90 microspheres for hepatocellular carcinoma. *Med. Phys., 31*(9), 2449-2453.

Sebastian, A., Szyszko, T., Al-Nahhas, A., Nijran, K., & Tait, N. (2008). Evaluation of Hepatic Angiography Procedures and Bremsstrahlung Imaging in Selective Internal Radiation Therapy: A Two-Year Single-Center Experience. *Cardiovasc. Intervent. Radiol., 31*(3), 643-649.

Selwyn, R. G., Nickles, R. J., Thomadsen, B. R., DeWerd, L. A., & Micka, J. A. (2007). A new internal pair production branching ratio of 90Y: The development of a non-destructive assay for 90Y and 90Sr. *Appl. Radiat. Isot., 65*(3), 318-327.

Sharkey, R. M., & Goldenberg, D. M. (2006). Targeted Therapy of Cancer: New Prospects for Antibodies and Immunoconjugates. *CA Cancer J. Clin., 56*(4), 226-243.

Shen, S., DeNardo, G. L., & DeNardo, S. J. (1994a). Quantitative bremsstrahlung imaging of yttrium-90 using a Wiener filter. *Med. Phys., 21*(9), 1409-1417.

Shen, S., DeNardo, G. L., Yuan, A., DeNardo, D. A., & DeNardo, S. J. (1994b). Planar Gamma Camera Imaging and Quantitation of Yttrium-90 Bremsstrahlung. *J. Nucl. Med., 35*, 1381-1389.

Shivaramu. (1986). Spectral shapes for atomic-field bremsstrahlung produced by beta particles of yttrium-90 in thick targets of Cu, Cd, Ta and Pb. *J. Phys. B: At. Mol. Phys., 19*, 1935-1944.

Siegel, J. A., & Khan, S. H. (1994). Body contour determination and validation for bremsstrahlung SPECT imaging. *J. Nucl. Med., 37*, 495-497.

Siegel, J. A., & Khan, S. H. (1996). Body contour determination and validation for bremsstrahlung SPECT imaging. *J. Nucl. Med., 37*, 495-497.

Simpkin, D. J., Cullom, S. J., & Mackie, T. R. (1992). The spatial and energy dependence of bremsstrahlung production about beta point sources in $H_2O$. *Med. Phys., 19*(1), 105-114.

Sureshbabu, W., & Mawlawi, O. (2005). PET/CT Imaging Artifacts. *J Nucl Med. Technol., 33*(3), 156-161.

Taylor, W. J., Corkill, M. M., & Rajapaske, C. N. (1997). A retrospective review of yttrium-90 synovectomy in the treatment of knee arthritis. *Rheumatology, 36*(10), 1100-1105.

Vilches, M., Garcia-Pareja, S., Guerrero, R., Anguiano, M., & Lallena, A. M. (2007). Monte Carlo simulation of the electron transport through thin slabs: A comparative study of PENELOPE, GEANT3, GEANT4, EGSnrc and MCNPX. *Nucl. Instrum. Methods Phys. Res. B, 254*, 219-230.

Volkert, W. A., Goeckeler, W. F., Ehrhardt, G. J., & Ketring, A. R. (1991). Therapeutic Radionuclides: Production and Decay Property Considerations. *J. Nucl. Med., 32*(1), 174-185.

Wagner, H. N., Jr., Wiseman, G. A., Marcus, C. S., Nabi, H. A., Nagle, C. E., Fink-Bennett, D. M., Lamonica, D. M., et al. (2002). Administration Guidelines for Radioimmunotherapy of Non-Hodgkin's Lymphoma with 90Y-Labeled Anti-CD20 Monoclonal Antibody. *J. Nucl. Med., 43*(2), 267-272.

Weiner, R. E., & Thakur, M. L. (2005). Radiolabeled peptides in oncology: role in diagnosis and treatment. *BioDrugs, 19*(3), 145-163.

Yu, J., Häfeli, U. O., Sands, M., & Dong, Y. (2003). $^{90}$Y-oxine-ethiodol, a potential radiopharmaceutical for the treatment of liver cancer. *Applied Radiation and Isotopes, 58*(5), 567-573.

Zaidi, H. (1999). Relevance of accurate Monte Carlo modeling in nuclear medical imaging. *Med. Phys., 26*(4), 574-608.

Zaidi, H. (2006). Recent developments and future trends in nuclear medicine instrumentation. *Med. Phys., 16*, 5-17.

Zanzonico, P. B., Binkert, B. L., & Goldsmith, S. J. (1999). Bremsstrahlung Radiation Exposure From Pure β-Ray Emitters. *J. Nucl. Med., 40*(6), 1024-1028.